Applications of analyticity to scalar meson phenomenology

Stuart Nicholas Cherry

Applications of Analyticity to Scalar Meson Phenomenology

Stuart Nicholas Cherry

A thesis presented for the degree
of Doctor of Philosophy

Department of Mathematical Sciences
University of Durham

August 2001

I would like to dedicate this thesis to my

mother and the memory of my father.

Abstract

Applications of Analyticity to Scalar Meson Phenomenology.

Stuart Nicholas Cherry.

A thesis presented for the degree of Doctor of Philosophy, August 2001.

The scalar mesons have caused much debate amongst hadronic physicists for many years. Even today the number of scalars is hotly contested, and there is almost no agreement on the composition of any of the experimentally observed states, except perhaps for the $K_0^*(1430)$. This thesis attempts to shed light on both of these problems via the application of analyticity to two different quantities.

Recently a number of authors have proposed the existence of a light, strange, scalar meson known as the κ. We perform a direct search of the best available πK scattering data to determine whether or not this resonance exists. This is done by constructing contour integrals from these data and determining the number of poles present inside the contour. We do not need to model either the internal dynamics of the state nor the form of the background scattering. The number of poles found tells us the number of resonances present and their positions allow us to estimate the resonance parameters. We find that there is only one resonance in scalar πK scattering below 1800 MeV and this is identified with the established $K_0^*(1430)$. We find no evidence for the κ.

Secondly, applying Cauchy's Theorem to the vacuum polarisation function leads to a relation between experimental and theoretical integrals known as a Finite Energy Sum Rule (FESR). FESRs are used to explore the scalar, isoscalar non-strange current and allow us to determine which of the experimentally observed scalar, isoscalar mesons is most likely to be the $u\bar{u} + d\bar{d}$ state. We find that the lightest scalar, isoscalar $u\bar{u} + d\bar{d}$ state is *not* the $f_0(980)$ as suggested by some authors, but is rather the light, broad object known as the $f_0(400-1200)$. We are also able to estimate the average light quark mass and find $m_q(1\ \mathrm{GeV}^2) = 4.7 \pm 0.9$ MeV which is consistent with the recent estimates of this quantity from unquenched lattice QCD.

Contents

List of Figures

List of Tables

Declaration

This thesis is the result of research carried out during the period October 1997 to July 2001 in the Department of Mathematical Sciences at the University of Durham and the Institut de Phyisque Nucléaire d'Orsay at the Université de Paris-Sud XI. No part of this thesis has been presented for a degree at these or any other universities.

Chapter 1 and parts of Chapters 2 and 4 contain some necessary background material and no claim of originality is made. The remaining work is believed to be original unless otherwise stated.

Chapters 2 and 3 are based on work done in collaboration with Mike Pennington and has been published in [129]. Chapters 4 and 5 are also based on work done in collaboration with Mike Pennington and will form part of a paper currently in preparation.

Acknowledgements

Firstly, I would like to thank my supervisor, Mike Pennington, for all his support, advice and encouragement over the course of this work. I would also like to thank all the people at the Institut de Physique Nucléaire d'Orsay for their hospitality during the last year.

I am most grateful for the financial support I have received both from the EPSRC during my time in Durham and the EU via the EuroDaphne Collaboration (TMR Contract Number ERBFMRXCT980169) during my time in Orsay.

Next I would like to say a big thank you to a number of friends: my office mates in Durham (Clare, Linda, Matt and Vinay) for putting up with me for three years, Kate for her spare room and all the help in dealing with the binding, Helen and in particular Ruth for her blend of support and abuse.

Lastly, but most definitely not leastly, I would like to thank my family for all their support, emotional, practical and financial, that they have always been so ready to provide.

Chapter 1

Introduction

1.1 The Strong Interaction

The nucleus of an atom is made up of positively charged protons and uncharged neutrons. Like charges repel, thus there must exist a force stronger than electromagnetism which binds protons and neutrons into nuclei, otherwise the many elements that make up the universe could not exist. In a famous paper of 1935 [1] Yukawa suggested that this force, known as the strong force, was carried by particles approximately two-hundred times more massive than the electron. These particles became known as *mesons* (meso meaning middle) as their predicted mass was between those of the light electron and the heavy nucleons.

Studies of cosmic rays led to the discovery in 1947 of two distinct particles with masses around two hundred and three hundred times the mass of the electron [2]. The lighter of these, which had in fact been detected previously, did not interact strongly with atomic nuclei and was later found to be a type of heavy electron: the muon. The heavier particle, which did interact strongly with nuclei, was identified with Yukawa's particle and was named the π-meson. The picture of the strong interaction seemed simple: atomic nuclei were collections of protons and neutrons bound together by the exchange of π-mesons (or *pions*).

However, this picture soon became more complicated with the unexpected discovery, once again in cosmic rays, of more strongly interacting particles. As

their existence was not expected and due to the peculiar difference between their production and decay rates, these particles were called *strange* particles. We now know them as the K-meson (or *kaon*) and the hyperons, Λ^0, $\Sigma^{\pm}$ and Ξ^-.

With the advent of high energy particle accelerators and colliders, the number of strongly interacting particles known grew rapidly. The term meson became redefined as any strongly interacting particle with integer spin, regardless of its mass. The hyperons, nucleons and other strongly interacting particles with half-integer spin were called *baryons*. By 1961 it was clear that the baryons with spin-1/2 and positive parity made a set of eight and could be arranged into a distinctive patten according to their quantum numbers, see Figure 1.1(a). Gell-Mann and Ne'eman [3] explained this phenomena by using Group Theory: this was the famous *Eightfold Way*. They predicted that the mesons with spin-0 and negative parity should also make up a group of eight, though only seven were then known: three pions and four kaons. This group of eight would then form the same pattern as the spin-1/2 baryons, see Figure 1.1(b), implying that the new meson was uncharged. The eighth member of the *octet*, the η, was found that same year.

In 1964 Gell-Mann and Zweig [4] noticed that the patterns arising from the Eightfold Way, as illustrated in Figure 1.1, could be simply explained by assuming that all strongly interacting particles were made of combinations of a triplet of fundamental, spin-1/2 objects and their antiparticles. Gell-Mann named these objects *quarks* and labelled the individual quarks u (up), d (down) and s (strange), see Figure 1.2. This label describes a property of the quarks that is now called *flavour*. In this model, baryons are made up of three quarks and mesons of a quark and an antiquark. With three different flavours, there are nine possible ways to combine a quark and an antiquark. This means that mesons should appear in *nonets*, which we now know that they do, such as the $J^P = 0^-$ (or pseudoscalar) nonet consisting of three pions (π^+, π^0, π^-), four kaons (K^+, K^0, $\overline{K^0}$, K^-) and two isospin zero particles, η and η', and the $J^P = 1^-$ (or vector) nonet,

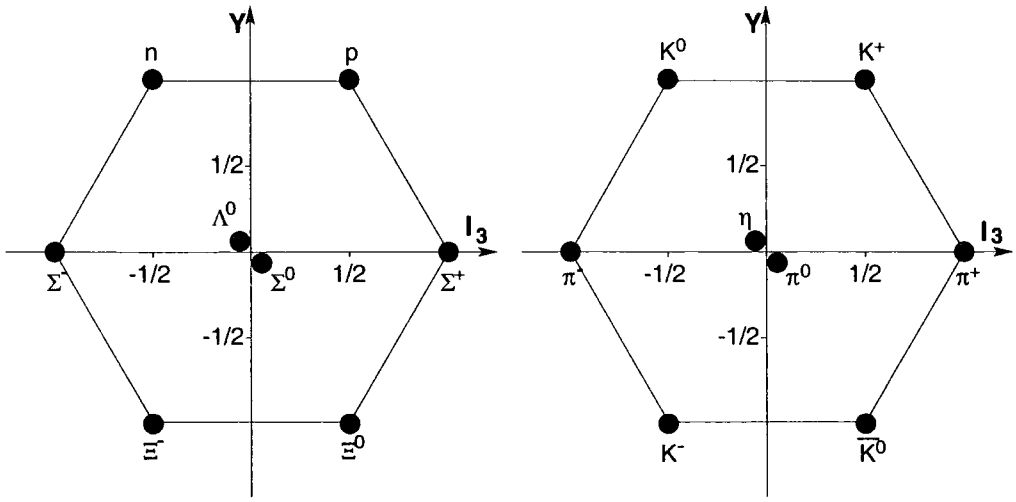

(a) The $\frac{1}{2}^+$ baryons

(b) The pseudoscalar mesons

Figure 1.1: The Eightfold Way for the spin-1/2 baryons and the pseudoscalar mesons. The quantities on the axes are hypercharge, Y, which is equal to strangeness plus the baryon number, and the third component of isospin, I_3, which is equal to the electric charge minus half the hypercharge. For mesons the baryon number is zero and for baryons it is one.

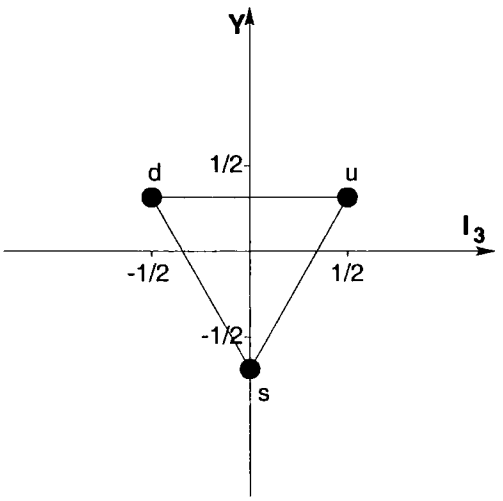

Figure 1.2: The three quarks required to explain patterns of the Eightfold Way. Quarks have a baryon number of 1/3, as three quarks make a baryon. Thus quarks have fractional electric charge.

(ρ, K^*, ω, ϕ). The vector nonet is illustrated in Figure 1.3 along with the quark combinations that gives rise to it.

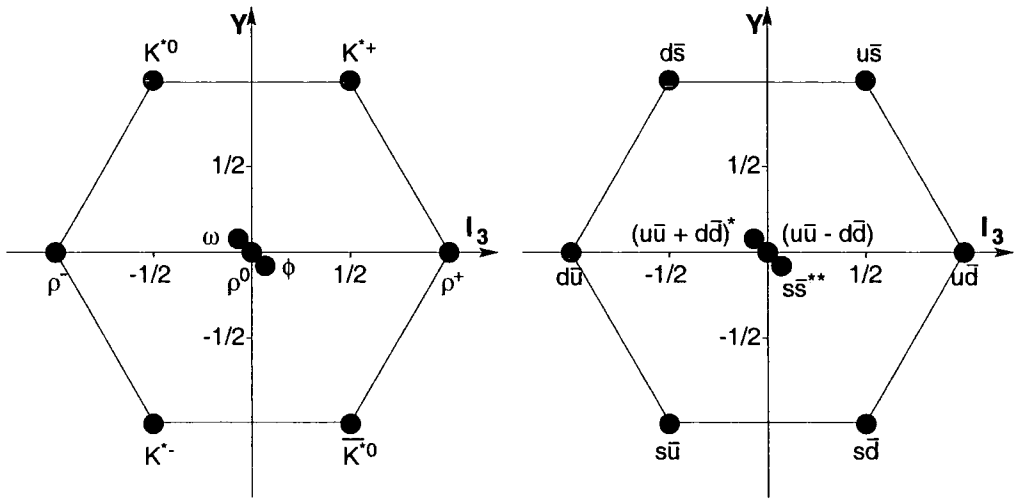

(a) The vector mesons

(b) The quark substructure

Figure 1.3: The vector meson nonet and its quark substructure. The states marked $*$ and $**$ are linear combinations of the states $u\bar{u}$, $d\bar{d}$ and $s\bar{s}$. For the pseudoscalar mesons we get the combinations $(u\bar{u}+d\bar{d}-2s\bar{s})$ and $(u\bar{u}+d\bar{d}+s\bar{s})$ respectively.

1.2 Coloured Quarks and QCD

There were, however, problems with the quark model. According to the Pauli Exclusion Principle (or more generally Fermi-Dirac statistics) two identical spin-1/2 particles, such as quarks, can not exist in the same state. But this is exactly what seems to happen in certain hadrons, for example the Ω^-. This is a baryon with strangeness -3, spin 3/2 and positive parity. Thus it must consist of three strange quarks, all spinning in the same direction. This seems to violate Fermi-Dirac statistics. Secondly, why were only certain combinations of quarks, qqq and $q\bar{q}$, seen experimentally? In particular, why don't we see individual quarks?

These problems were explained by assuming that quarks possessed another, hidden, degree of freedom [5], *i.e.* there were in fact three types of s-quark, each

differing by their value of this new degree of freedom. Thus Fermi-Dirac statistics wasn't violated in the Ω^- as the three quarks were not identical. Furthermore, if we assume that the only particles that can exist are those whose overall value of this new degree of freedom is zero, then this would explain why the combinations qqq and $q\bar{q}$ are seen but individual quarks aren't. As three different values of this new degree of freedom could combine to give zero, it became known as *colour* by analogy with red, green and blue light combining to give white. Colour is completely separate from flavour, in particular the hadron *multiplets* of the quark model are not modified by the existence of three colours of quarks.

The physics of electric charges is very accurately described by Quantum Electrodynamics or QED. This is a type of theory, known as a gauge theory, which combines special relativity and quantum mechanics. In the sixties, physicists tried to find an analogous theory to describe strongly interacting particles. The result was Quantum Chromodynamics [6], or QCD, which is the gauge theory of colour. In this theory, quarks are bound together by *gluons* to form colourless hadrons. The massless gluons act on the colour charge of the quarks in much the same way as a photon acts on electric charge. The big difference is that gluons also carry colour charge and so can interact with each other: photons are not charged therefore two photons cannot interact directly. It is this that leads to the finite range of the colour interaction. The force that binds protons and neutrons into nuclei is a complicated residual effect of this gluon mediated interaction.

Another difference between QED and QCD is that in QCD the strength of the interaction is greatest at low energies. In fact, at very high energies the quarks inside a proton behave as if they weren't bound together at all. This has made it possible to accurately calculate many physical quantities directly from QCD using the technique of Perturbation Theory, but only at high energies. At lower energies, such as those corresponding to the mass of the proton, QCD calculations cannot be carried out without some form of approximation being made. So, although the underlying theory of the strong interaction has been

known for thirty years, the study of hadrons still relies heavily on the use of models.

The existence of gluons and their ability to interact with each other opened up the possibility of new types of particles. Gluons carry colour charge and so cannot exist in isolation. However, it was realised very soon after the birth of QCD [7] that two or more gluons could combine to form uncoloured states. These states, known as *glueballs*, should then appear in the hadronic spectrum. Another possibility allowed by QCD are the so called *hybrid* hadrons [8] which consist of both quarks and gluons *e.g.* $q\bar{q}g$. Thus the spectrum of hadrons within QCD is far richer than in the naive quark model.

1.3 Hadronic Physics

Typically in quantum field theory the spectrum of states is determined by solving the equations of motion which arise from the Lagrangian of the theory. Although its Lagrangian has been known for thirty years now, we are still not able to do this for QCD at the energies of hadronic physics. However, via a number of less direct approaches we have been able to gain a great deal of understanding about the low energy structure of QCD. We will now outline a few of these approaches whose results have been important to the study of mesons..

1.3.1 Lattice Gauge Theory

This is the most direct approach to the study of the strong interaction at low energies. Space-time is represented by a four-dimensional lattice, with the separation between neighbouring lattices given by a. Wilson [9] discovered that when a gauge theory with sufficiently strong interactions is formulated on this lattice, it automatically displays *colour confinement.* To put this another way, the *ad hoc* assumption above that only uncoloured objects can exist arises as a natural consequence of doing QCD on the lattice. The limit of this discrete theory

as the the lattice spacing goes to zero will then give us QCD at low energies. Formulating QCD on the lattice lends itself to direct numerical calculation on a computer and in fact requires a great deal of computational power. Lattice QCD is extremely versatile and can be used to determine the properties of hadrons, see for example [10, 11], as well as the parameters of the QCD Lagrangian such as the quark masses; for a recent review of quark mass determinations on the lattice see [12].

Although in the long term it is believed that the lattice will give the most reliable results, it currently suffers from two problems which are slowly being overcome by increased computing power and improved algorithms. Firstly, QCD predicts that virtual $q\overline{q}$ pairs (sea quarks) are continually being emitted and absorbed within hadrons. To simulate this is extremely computationally expensive and until recently most works ignored this effect. This is equivalent to assuming infinitely heavy sea quarks and is known as the *quenched approximation.* In the last few years it has become possible to work with *unquenched* lattice QCD, firstly with 2 flavours of sea quarks, *e.g.* see [13], and most recently with three, *e.g.* [10]. Thus we are getting closer to full QCD on the lattice but the masses of the sea quarks are still unphysically large.

Lattice simulations are costly and time consuming, the more so as the lattice spacing is decreased. Consequently, most studies involve runs at only a few different values of a. Thus the extrapolation to $a = 0$, the continuum limit, is not totally under control.

1.3.2 The MIT Bag Model

Within this model, first proposed in [14], quarks and gluons are confined within a finite region of space, known as a *bag*, by the inclusion of a positive energy density within the bag. The assumption of this *bag pressure* ensures that only uncoloured objects can exist and leads to equations of motion that can be approximately solved to give the physical states.

In [15] the masses and other static quantities of the two lightest meson (pseudoscalar and vector) and baryon ($\frac{1}{2}^+$ and $\frac{3}{2}^+$) multiplets were calculated within the Bag Model and were found to give reasonable agreement with experiment.

1.3.3 Potential Models

In this class of models, also called constituent quark models, conventional mesons are treated as a $q\overline{q}$ system bound by some (static) potential. This potential is phenomenological in origin and in general includes a confining part, a Coulomb-type part and spin dependent pieces. Once this potential is formulated, the meson spectrum can be found by solving for the eigenvalues of the Schrödinger equation. The masses of the constituent quarks are then tuned to give the best agreement with experiment; these masses are not related to the quark masses that appear in the QCD Lagrangian. These models are non-relativistic and thus work best for heavy quark systems. The effects of relativity can to some extent be modelled by the inclusion of various parameters in the potential. For a fuller explanation of potential models see, for example, the discussion in [16].

1.3.4 Dressing and Unitarised Quark Models

In a world without interactions $q\overline{q}$ and gg systems would be absolutely stable, as the existence of lone quarks or gluons is forbidden by colour confinement, and would have fixed masses given by the quark model or quenched lattice QCD. If we turn on interactions, which is equivalent to unquenching on the lattice, we allow these *bare* states to couple to mesonic channels and thus permit them to decay. This *dressing* also shifts the physical masses away from the bare values [17, 18].

Unitarised Quark Models [19, 20] apply this idea of dressing by coupling (ideally mixed) $q\overline{q}$ states to two meson channels only. In the isoscalar sector of a particular channel, the $u\overline{u} + d\overline{d}$ and $s\overline{s}$ can then mix as both couple to the two kaon channels. gg seed states, which could affect the masses of the isoscalars, are not included and multiquark effects are assumed to be small. The scattering

amplitude for a given channel can be calculated, or fit to data, and the number and position of the resonances determined. These models have had reasonable success in reproducing meson spectra and scattering data in a number of sectors.

1.4 The Scalar Meson Problem

The quark model and QCD have enabled us to explain a large range of hadronic phenomena. However, the scalar ($J^{PC} = 0^{++}$) mesons still give rise to a great deal of debate. Whereas the placing of pseudoscalar and vector mesons into their familiar nonets, (π, K, η, η') and $(\rho, K^*, \omega, \phi)$, was fundamental to the creation of the quark-model, this has still not been done for the scalars nearly forty years later. A brief glance at the most recent edition of the Particle Data Guide [21] shows that there are currently more scalar mesons listed than are required for a quark model nonet. In the isospin-0 sector five mesons are listed below about 1700 MeV, the $f_0(400-1200)$, $f_0(980)$, $f_0(1370)$, $f_0(1500)$ and $f_0(1710)$. Some authors suggest even more (*e.g.* [22]) and some believe that not all the states listed are mesons (*e.g.* [23]). There are also two isospin-1 states, the $a_0(980)$ and $a_0(1450)$, but only one isospin-1/2 meson, the $K_0^*(1430)$. If we glance back through previous editions of the PDG [24] we see that the number and masses of mesons listed in this sector has changed many times. Why are so many states listed, and why is there so little agreement on their properties?

Obtaining information on the scalar mesons is complicated by the fact that these states do not tend to dominate experimental cross-sections, their contribution being much less than higher angular momentum states. Furthermore, scalar states tend to be wide for their masses, making it difficult to determine their parameters in any model independent way. For the isospin zero states, the picture is complicated further by the overlapping of states, making the standard description of resonances via a Breit-Wigner formula impossible.

Theoretically, the possible spectrum of states in the scalar channel is, perhaps, more complicated than in any other. As explained above, QCD predicts the

existence of glueballs. Calculations of the glueball spectrum consistently predict that the lightest glueball will be a scalar and that the scalar glueball will have a mass comparable to ordinary $q\bar{q}$ states [11, 25].

QCD also permits the existence of multi-quark states. In order to determine whether such states are energetically favourable it is necessary to work within models of QCD. Within one such model, the MIT-bag model, it was found [26] that scalar mesons made up of two quarks and two antiquarks were not only possible, but their binding energy was such that these states would, in fact, be lighter than conventional $q\bar{q}$ scalar mesons. This implies that there should be two complete nonets of scalar mesons, and that the lightest scalar mesons will have the internal structure $qq\overline{qq}$.

This conclusion has been contested by the authors of [27]. They showed, within the confines of a nonrelativistic potential model of QCD, that $4q$-states could only exist under certain very special conditions. Namely, $4q$ states probably only existed in the scalar channel, must include a $s\bar{s}$ pair and that, rather than the bag-model picture of four quarks all tightly bound together, $4q$-states were loosely bound $K\overline{K}$ 'molecules'. Thus only states with isospin 0 and 1 would exist and there would not be a second complete scalar nonet. In particular, there would be no light strange scalar meson.

That the quark model leads to nonets of mesons is "a truth universally acknowledged". However, this 'fact' has been called into doubt, at least in the scalar sector, by the unitarised quark models (UQMs). When applied to the scalar mesons [28, 29] these models found that the mass shifts due to dressing were far greater than for other channels and also the scalar mesons were unique in undergoing a phenomenon known as resonance doubling. In resonance doubling, a single input state can give rise to two separate physical hadrons. Both of these hadrons are at one level $q\bar{q}$-states, but may also include large components of the two meson states in their wavefunctions. There are, however, some very significant differences between the results of the two models. In the Nijmegen

Unitarised Meson Model [28], resonance doubling occurs for all the scalar input states. Thus, they predict two complete scalar '$q\overline{q}$' nonets (including a light strange meson) and leave no room for any exotic states, except perhaps to explain the $f_0(1710)$. However, the Helsinki Unitarised Quark Model [29] finds that resonance doubling occurs only for certain input states. In particular they do not predict a light strange scalar meson and cannot explain the $f_0(1500)$ or $f_0(1710)$.

The picture is more complicated yet. As all of these theoretical possibilities have the same quantum numbers and similar masses, quantum mechanics tells us that they can and will mix. Thus, it may make no sense to talk about glueballs, $q\overline{q}$ and $4q$ states as separate objects. Some authors today prefer to keep the term meson solely for $q\overline{q}$-states. In this work we use meson in its older context, *i.e.* to mean any hadron with integer spin, and do not imply anything about a state's internal structure by this name.

We can, then, express the so called Scalar Meson Problem in three questions? How many scalars are there below 2 GeV? Which states are $q\overline{q}$ in origin? What are the remaining states (if there are any)?

1.5 Synopsis

The mathematical concept that underlies and links the two strands of this work is Cauchy's Theorem, which is stated here for completeness.

$$\frac{1}{2\pi i}\oint_C f(z)\,\mathrm{d}z = \sum (\text{Enclosed residues}) \tag{1.1}$$

This theorem is so well known that we do not include a proof, which can be found in any undergraduate level text book on complex analysis.

We will apply Cauchy's Theorem in two different ways to address the first two questions posed at the end of the preceeding section. In Chapters 2 and 3 we will investigate the possibility that there are two complete scalar nonets below 2 GeV. More precisely we will try to determine whether or not there exists a strange scalar meson with a mass less than the established $K_0^*(1430)$. To this

end, we construct contour integrals from S-wave πK scattering data. From these integrals Cauchy's Theorem allows us to determine the position of any poles of the scattering amplitude within the contour. The number and positions of these poles give us the number of resonances present in the channel and their parameters.

In Chapters 4 and 5 we turn to the question of the composition of the scalar isoscalar mesons. In particular we will try to determine which is the lightest $q\bar{q}$ state in this channel. By applying Cauchy's Theorem to the $q\bar{q}$ vacuum polarisation function in the $I = J = 0$ channel, we are able to relate an integral of experimental data to the integral of a theoretical expression written in terms of quark fields. Thus we can relate $q\bar{q}$-states to physical hadrons.

Chapter 2

Hunting the κ: Background and Framework

2.1 Introduction

The light, strange scalar meson (usually known as the κ) has a long and somewhat chequered history. The first experimental claims for it came as far back as 1962 [30] and by 1966 theoreticians were predicting its existence [31] in order to satisfy sum rules of the Adler-Weisberger type. These sum rules relate axial-vector coupling constants to combinations of total cross-sections for (in this case) πK scattering. These cross-sections can be written in terms of low-energy resonances whose parameters can then be determined.

At about this time a number of experimental groups were reporting tentative 'observations' of the κ meson, suggesting a mass of around 725 MeV and a width $\lesssim 12 - 30$ MeV (for a review of these early experimental searches for the κ see [32]). By 1967, similar theoretical methods and the experimentally favoured mass were used to predict a width for the κ of $\sim 20 - 30$ MeV [33]. However, there was no consensus on the existence of the κ in either the theoretical or experimental communities. Another theoretical analysis based on Adler-Weisberger sum rules [34] pointed out that uncertainties in the calculation could remove the

need for the κ while the Particle Data Guide of 1967 [32] contained the following statement:

> "We are beginning to think that the κ should be classified along with flying saucers, the Loch Ness Monster and the Abominable Snowman."

It went on to explain that many experiments had searched for the κ but, at that point, none had found any direct evidence. The year after this statement appeared direct evidence for a light, strange, scalar state in the reaction $K^+p \to K^0\pi^0\Delta^{++}$ was reported [35]. This particle, with a mass of 1100 MeV and a width of 400 MeV, bore little resemblance to that predicted in the above works. The authors reported, however, that it it did satisfy the sum-rules upon which they were based.

During the 1970s a number of experiments reported seeing the κ with the consensus being for a much broader and heavier resonance than that favoured in the 60s (for a summary of these experiments see the mini-review listed under the $\kappa(1350)$ in [36]). The largest statistics at this time came from a study of the reactions $K^\pm p \to K^\pm\pi^+ n$ and $K^\pm p \to K^\pm\pi^-\Delta^{++}$ [37] which reported a resonance with a mass of 1425 MeV and a width around 250 MeV. These conclusions were supported by the LASS collaboration in 1988 [38]. Their study of the reaction $K^-p \to K^-\pi^+ n$ gave the highest statistics on $K\pi$ scattering currently available and found a strange scalar resonance of mass 1412 MeV and width 294 MeV. By this time the strange scalar resonance had also undergone a name change: the κ had become the K_0^*. Subsequent experiments [39, 40] have found no evidence to support a light κ, with the $K_0^*(1430)$ being sufficient to describe $IJ^P = \frac{1}{2}0^+$ πK scattering[1]. From now on we will keep the name κ to mean a strange scalar meson below the well established $K_0^*(1430)$.

Theoretically too, the lightest strange scalar meson was undergoing something

[1] At the time of writing rumours are beginning to appear that the E791 experiment at Fermilab can best describe its data on the decay $D^+ \to K^-\pi^+\pi^+$ by including a κ. As yet final results have not been published but see [41].

of a change of identity. In 1977, Jaffe [26] used the MIT-bag model to study multiquark hadrons. concluding that a broad κ with a mass of around 900 MeV should form part of a light $qq\overline{q}\overline{q}$ nonet. However, in 1982 Weinstein and Isgur [27] showed that, within a non-relativistic potential model of QCD, a $qq\overline{q}\overline{q}$ system with open-strangeness could not be bound into a meson. In that same year, Scadron [42] suggested that the spontaneous breakdown of SU(3) chiral symmetry leads to a low mass $\boldsymbol{q\bar{q}}$ scalar nonet including a κ which, with a mass of 800 MeV and width of 80 MeV, was consistent with the particle 'seen' in the experiments of the late 60s. A light κ was also predicted within the framework of the unitarised meson model [28]. Although work in a similar model [29] found only one strange, scalar resonance: the $K_0^*(1430)$.

In recent years a number of authors have revived the idea of a light (< 1 GeV) κ as the $SU(3)_f$ partner of the (now widely accepted) σ-meson, arguing that if the σ exists then why not the κ. Ishida *et al.* [43] reanalysed the LASS data, introducing a background with a negative phase-shift, and found that a light κ could be accommodated, with the background 'hiding' the expected effect of a resonance on the phase-shifts. In the work by Black *et al* [44], a model amplitude inspired by the large-N_c expansion of QCD is compared to the real part of the experimental amplitude. Within this model the κ is required to maintain the unitarity of the amplitude below 1 GeV. Oller and Oset [46] also find a κ as a meson-meson state arising from the unitarisation of the lowest order amplitude obtained from Chiral Perturbation Theory. Anisovich and Sarentsev [47] have performed a K-matrix analysis of the LASS data concluding that the κ is not present.

In this new incarnation the κ has been ascribed a large range of masses but is generally agreed to be a very wide object. In Table 2.1 we list the parameters obtained from some of the recent analyses.

The LASS experiment provides us with high statistics results on the π^+K^- S-wave amplitude from 825 MeV to 2.51 GeV [38]. The κ, if it exists, should

Source	Mass (MeV)	Width (MeV)	$\sqrt{s_{pole}}$ (MeV)
Van Beveren [28]	—	—	$727 - 263i$
Ishida [43]	905	545	$875 - 335i$
Black [44]	897	322	$911 - 158i$
Delbourgo [45]	810	—	—
Oller [46]	—	—	$779 - 330i$
Oller [48]	$\sim$850	very large	$770 - 250i$
Jamin [49]	—	—	$708 - 305i$

Table 2.1: The properties of the light κ resonance as found by various authors.

have an effect on the LASS data if its mass is within this energy range. In fact due to its large width we can expect that the effect of the κ will be apparent in the LASS data even if the mass is somewhat below 825 MeV. As mentioned above, a number of fits to these LASS (and other) data have been carried out, some finding evidence for the κ [43, 44] and some claiming to rule it out [29, 47]. However, the existence of a state is not defined by the ability (or otherwise) to fit a certain formula to data along the real axis in the $s-$plane. Indeed, a state is wholly specified by there being a pole of the $S-$matrix in the complex energy plane on the nearby unphysical sheet [50]. When carrying out a fit-to-data it is usually necessary to separate the scattering amplitude into resonance and background parts. It is the different modellings of the background, along with its large width, that leads to the large range of masses for the κ apparent in Table 2.1. Here, we will use an alternative approach that does not require such an artificial separation.

The aim of this project is to determine whether or not the best data currently available on the S-wave πK scattering amplitude (*i.e.* the LASS data) require or rule out the existence of a strange scalar resonance in the mass range $\sim$800–1000 MeV. We do this by attempting to directly count and locate the poles of the partial wave amplitude as constructed from the data with the minimum of theoretical modelling. We also consider the earlier data of Estabrooks *et al.* [37], which extends closer to threshold but with reduced precision. The method we will

use, which is due to Nogová *et al.* [51], combines some simple statistics with the analytic properties of the partial wave amplitude in a way that allows us to search for poles in the amplitude without recourse to a specific formula to parameterise these poles.

The method is explained in the remainder of this Chapter and the results obtained are presented in Chapter 3 along with a discussion of the inputs into the calculation.

2.2 Conformal Mapping

2.2.1 Analytic Structure of the πK Partial Wave Amplitude

Fig. 2.1 shows the analytic structure (except for resonance poles) of the S-wave partial wave amplitude for πK scattering as a function of the Mandelstam variable s, the square of the total centre of mass energy. The cuts shown in Fig. 2.1 arise in the following ways. Unitarity in the $s-$channel $\pi K \to \pi K$ scattering leads to the physical cut from $s = s_{th}$ to $s = \infty$. The left-hand cut, running from $s = -\infty$ to $s = (m_K - m_\pi)^2$, comes from the crossed ($u-$channel) $\pi K \to \pi K$ scattering. The circular cut is due to the unitarity of the $t-$channel process, $\pi\pi \to KK$. The origin of these cuts is discussed in more detail for the case of πN scattering by Hamilton [52]. It should be noted that in πK scattering there is no short cut $(m_K - \frac{m_\pi^2}{m_K})^2 \leq s \leq m_K^2 + 2m_\pi^2$ because, unlike πN scattering, there is no Born term.

Our final goal is to determine the complex positions of the poles of the partial wave amplitude from scattering data, which is obviously collected along the real axis. To do this we need to carry out some form of analytic continuation. This continuation will only be valid within a region characterised by the distance to the nearest singularity. To maximise this region, we begin by conformally mapping the unphysical sheet of the partial wave amplitude into the unit disc which we call

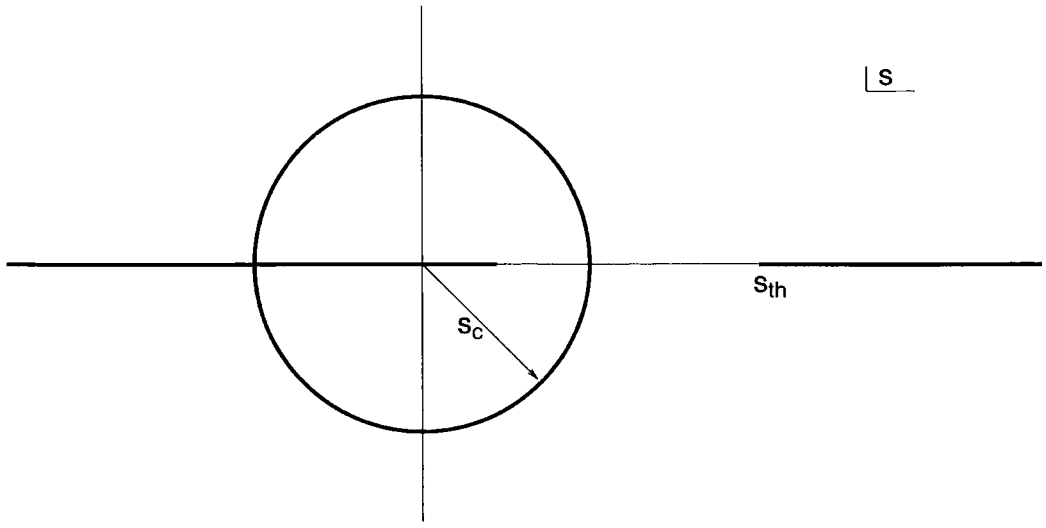

Figure 2.1: The cut structure of the πK partial wave amplitude, where $s_{th} = (m_K + m_\pi)^2$ and the radius of the circular cut is $s_c = m_K^2 - m_\pi^2$.

the $z-$plane. In fact, for the scattering of unequal mass particles the cuts of the partial wave amplitude split the $s-$plane into two separate regions (see Fig. 2.1). The poles associated with resonances will lie in the region outside the circular cut and so it is this that we map into the $z-$plane. The mapping is designed so that the cuts of the partial wave amplitude in the $s-$plane are mapped onto the circumference of the circle. So, except for the resonance poles that we wish to locate, the partial wave amplitude will be analytic within the disc and we can continue the amplitude throughout the complex $z-$plane and thus, via the inverse mapping, the entire $s-$plane.

2.2.2 The Mapping

The mapping is accomplished in two steps. Firstly,

$$y(s) = \left(\frac{s - s_c}{s + s_c}\right)^2 \quad . \tag{2.1}$$

Under this mapping the cuts along the real axis of the $s-$plane are mapped to the positive real axis in the $y-$plane with $y(s_{th}) = m_\pi/m_K \approx 0.28$. The positive and negative real axis cuts in the $s-$plane are joined together in the $y-$plane at

the point $y(\infty) = y(-\infty) = 1$. The circular cut in the $s-$plane is mapped onto the negative real axis in the $y-$plane with the point $s = s_c$ mapped to the point $y = 0$. The point $s = -s_c$ appears on both the circular cut and the left-hand cut in the $s-$plane and so has two images in the $y-$plane at $y = \pm\infty$. The result of this mapping is shown pictorially in Fig. 2.2.

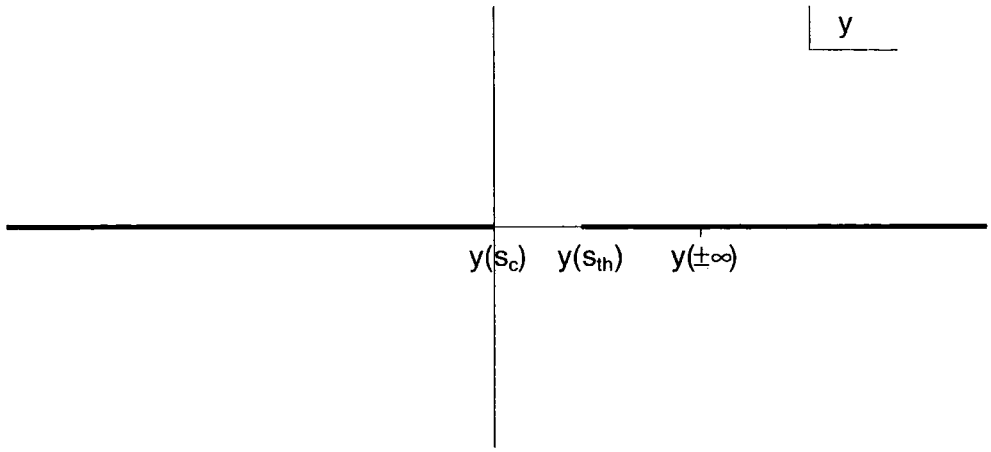

Figure 2.2: The cut structure in the $y-$plane with the mapping of certain key values of s shown. $y(s_c) = 0$, $y(s_{th}) \approx 0.28$ and $y(\pm\infty) = 1$.

Now, to map the twice cut $y-$plane into the unit disc, we define

$$z(s) = \frac{i\beta\sqrt{y(s)} - \sqrt{y(s) - y(s_{th})}}{i\beta\sqrt{y(s)} + \sqrt{y(s) - y(s_{th})}} \quad , \tag{2.2}$$

where β is a real parameter which is chosen so that the region of interest in the $s-$plane is mapped close to the imaginary axis in the $z-$plane. This minimises the distance the continuation must cover and increases the rate of convergence. If we believe that the pole is near the (complex) point s_p then we calculate β using

$$\beta = \left| \sqrt{\frac{y(s_p) - y(s_{th})}{y(s_p)}} \right| \quad . \tag{2.3}$$

The points $s = s_{th}$ and $s = s_c$, *i.e.* the branch points in the $y-$plane, are fixed for any value of β, being mapped to $z = 1$ and $z = -1$ respectively. For all other points, the position in the $z-$plane is dependent on the value of β. Fig. 2.3 shows the upper half of the $z-$plane with the images of certain values of s for a particular value of β. Notice that the cuts in the upper half of the $s-$plane

(such as the region where physical data lie) are mapped to the upper semi-circle in Fig. 2.3.

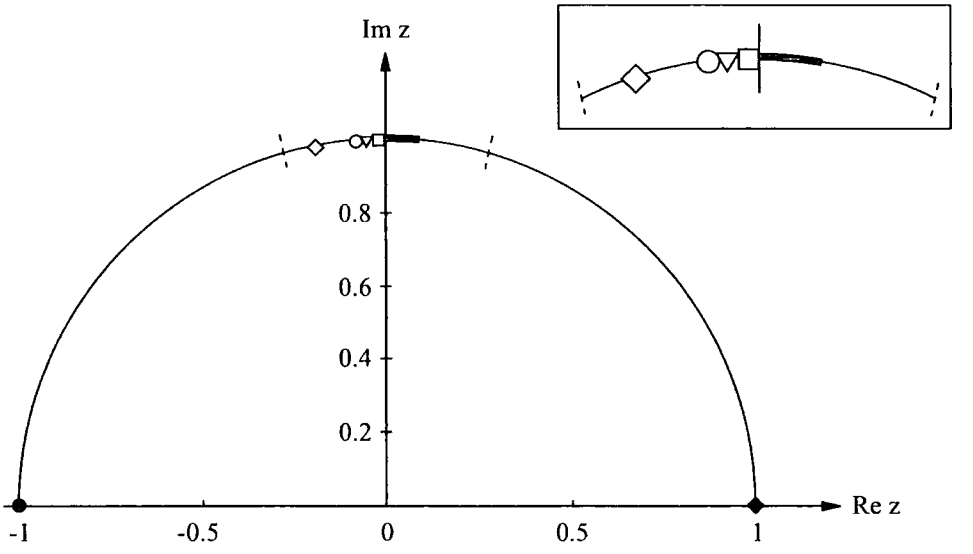

Figure 2.3: The $z-$plane showing how points in $s-$plane map. The mapping parameter β is chosen so that $s = (1.4 + 0.15i)^2$ GeV^2 is mapped to the imaginary axis. The thicker line shows the arc covered by the LASS data. The inset shows an enlargement of the key region close to $z = i$, from where we analytically continue. The symbols mark particular values of s as follows: $\blacklozenge$ $s = s_{th}$, $\square$ $s = \infty$, ∇ $s = -s_c$, $\circ$ $s = is_c$, $\Diamond$ $s = \frac{1}{\sqrt{2}}(s_c + is_c)$, $\bullet$ $s = s_c$.

Once the pole positions in the $z-$plane have been found, they will need to be mapped back to the $s-$plane to understand their physical significance. The inverse of the mapping defined in (2.1)-(2.2) is given by

$$u(z) = \sqrt{\frac{y(s_{th})(1+z)^2}{(1+z)^2 + \beta^2(1-z)^2}} \quad , \tag{2.4}$$

$$s(z) = s_c \left(\frac{1+u(z)}{1-u(z)} \right) \quad . \tag{2.5}$$

2.2.3 Some Comments about the Mapping

We require the mapping defined in (2.1) and (2.2) to preserve the real analyticity of the partial wave amplitudes. It is easy to check that this is the case for (2.1).

To see that it is also true for (2.2) we note that the effect of the branch cut in the $y-$plane is only felt by the square-root that has the same branch-point.

To illustrate this we consider first the point y_0, see Fig. 2.4, given by

$$y_0 = p^2 e^{2i\gamma} = y_{th} + q^2 e^{2i\delta} \tag{2.6}$$

$$\Rightarrow \quad y_0 - y_{th} = q^2 e^{2i\delta}. \tag{2.7}$$

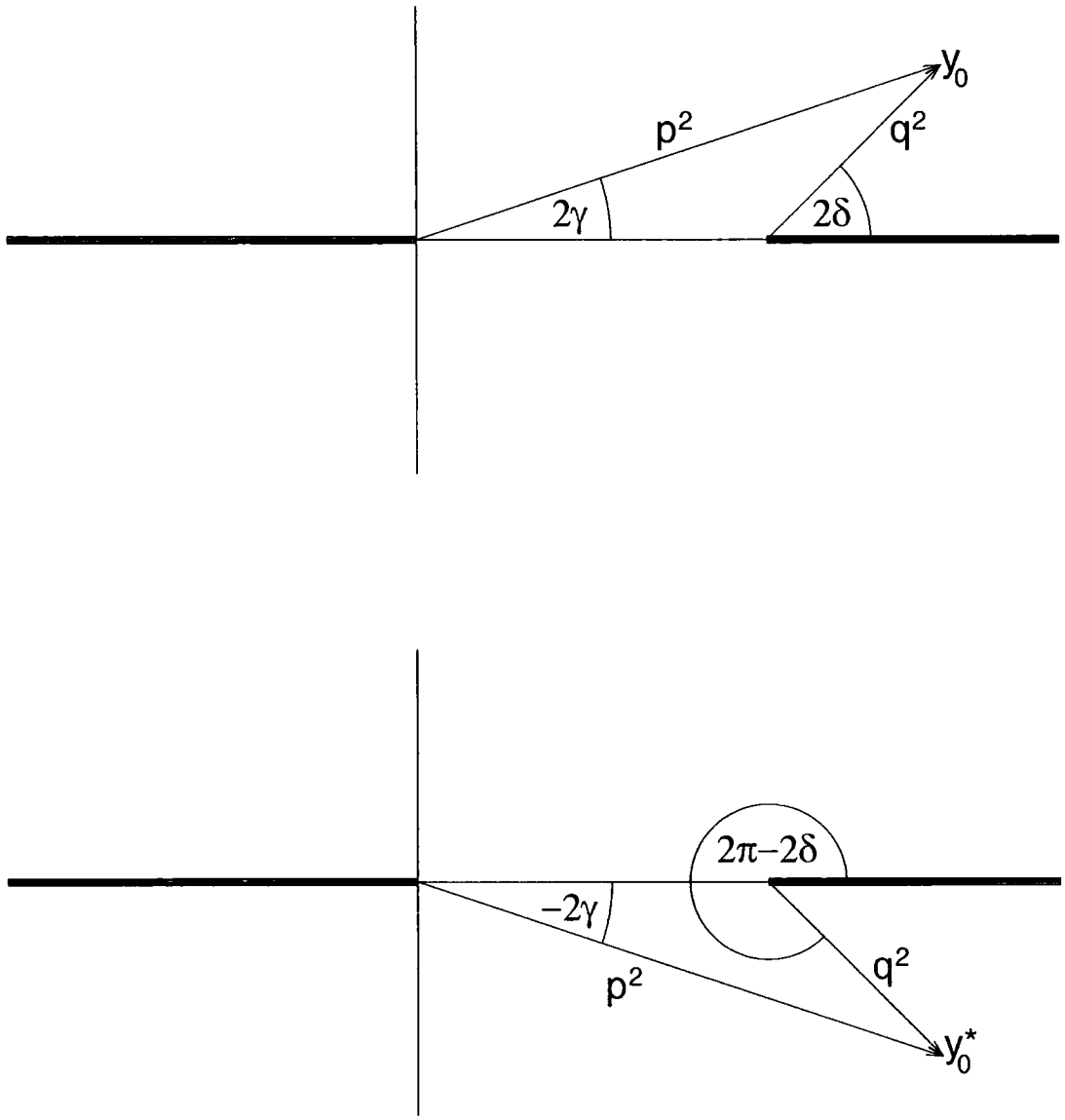

Figure 2.4: The $y-$plane as defined by (2.1) showing how the square roots in (2.2) are affected by the branch points of the partial wave amplitudes when going from a point y_0 to its complex conjugate y_0^*. $y_{th} = y(s_{th})$.

Therefore

$$z(y_0) = \frac{ipe^{i\gamma} - qe^{i\delta}}{ipe^{i\gamma} + qe^{i\delta}} \tag{2.8}$$

Now we consider the point y_0^*. As $\sqrt{y}$ has no branch point at y_{th}, we can go from $\sqrt{y_0} \to \sqrt{y_0^*}$ simply by changing 2γ to -2γ. However, $\sqrt{y - y_{th}}$ has a branch point at y_{th} so, in order to stay on the same sheet, when going from y_0 to y_0^* we must go around the branch point *i.e.* $2\delta \to 2\pi - 2\delta$. Thus,

$$y_0^* = p^2 e^{-2i\gamma} = y_{th} + q^2 e^{2i(\pi-\delta)} \tag{2.9}$$

$$\Rightarrow y_0^* - y_{th} = q^2 e^{2i(\pi-\delta)} \tag{2.10}$$

and

$$\begin{aligned} z(y_0^*) &= \frac{ipe^{-i\gamma} - qe^{i(\pi-\delta)}}{ipe^{-i\gamma} + qe^{i(\pi-\delta)}} \\ &= \frac{-ipe^{-i\gamma} - qe^{-i\delta}}{-ipe^{-i\gamma} + qe^{-i\delta}} \\ &= [z(y_0)]^*. \end{aligned} \tag{2.11}$$

If $\Re(y_0)$ had been less than zero, *i.e.* the position of the other branch-point, then when going from y_0 to y_0^* the vector would have crossed the branch cut corresponding to $\sqrt{y}$. A similar argument to above would hold with $2\delta \to -2\delta$ and $2\gamma \to 2\pi - 2\gamma$.

From Fig. 2.3 we can see that the mapping is highly non-linear in the following sense. As we increase the energy from threshold to infinity, the proportion of the circle covered by each increment falls very sharply. It is clear that the region between threshold (at 633 MeV) and the start of the data (at 825 MeV) covers a much longer arc than the region in which we have data (825 MeV to 2.51 GeV) and the region between the end of the data and infinite energy is much smaller still. This compression of the high energy region would suggest that the method is less sensitive to higher mass resonances. This apparent weakness actually has some benefit. As we explain in the next section, we test the scattering amplitude against the hypothesis that it contains a given number of poles. The computational burden increases rapidly as we increase the number of poles, so if

we had to account for all the radial excitations in a given channel the calculation would soon become computationally prohibitive. Consequently, the procedure is only practicable for the lowest few states.

It is obvious from this mapping that the physical region in the $s-$plane only covers a fraction of the circle. Even if we had data over an infinite range of energies, we could never complete the circle, see Fig. 2.3. Nevertheless, we only need analytically continue very close to the region of data (*i.e.* the solid arc in Fig. 2.3). We shall return to this point later.

2.3 Analytic Continuation

2.3.1 The Subtraction Method

For now we assume that we have a scattering amplitude, y_i, with errors, Δ_i,[2] , defined at discrete points all the way around our circle $|z| = 1$. We define $|\delta z_i|$ as the average distance between the ith data point and its two nearest neighbours in the complex $z-$plane shown in Fig. 2.3. In regions where these discrete points are densely packed, our scattering amplitude is most tightly controlled and so we weight the error on each point by the density of the data points in that region, defining $\epsilon_i(z) = \Delta_i\sqrt{|\delta z_i|/2\pi}$. We make a smooth interpolation to the amplitude, $Y(z)$, and the weighted errors, $\epsilon(z)$, so that we have continuous functions defined on the entire circle. This weighting procedure ensures that the small region of the unit circle in Fig. 2.3, where we have experimental data, controls the analytic continuation into the nearby region where resonance poles are expected to sit.

If $F(z)$ is a square integrable function on the circle, C, then we can test how well this function describes the data through a χ^2, defined by

$$\chi^2 = \frac{1}{2\pi}\oint_C \left|\frac{F(z) - Y(z)}{\epsilon(z)}\right|^2 |\mathrm{d}z| \quad . \tag{2.12}$$

[2]This method requires the errors on the real and imaginary parts of the amplitude to be equal. This is arranged by taking the value of the error to be the larger of the error on the real part and the error on the imaginary part at any given energy.

We now introduce a non-zero weight function $g(z)$, which is defined to be real analytic and constrained by $|g(z)| = \epsilon(z)$ around the circle. This weight function will take the role of the errors in our χ^2, but has the analytic properties that we require. We expand the data and the trial function as Laurent series about the origin, so that

$$y(z) = \frac{Y(z)}{g(z)} = \sum_{k=-\infty}^{\infty} y_k z^k \quad , \quad f(z) = \frac{F(z)}{g(z)} = \sum_{k=-\infty}^{\infty} a_k z^k \quad . \tag{2.13}$$

Since partial wave amplitudes are real analytic, the coefficients a_k and y_k are real. Although we are expanding about the origin, the expansion is carried out round the circle, since this is where we have data. The singular Laurent coefficients will pick up any poles within the disc. Substituting (2.13) into (2.12) gives

$$\chi^2 = \sum_{k=1}^{\infty} (a_{-k} - y_{-k})^2 + \sum_{k=0}^{\infty} (a_k - y_k)^2 \quad . \tag{2.14}$$

The pole structure of our partial wave amplitude, $Y(z)$, can then be determined by finding the test function $F(z)$ which minimises the first summation in (2.14).

If we want to test against the assumption that there are no poles in the data we must use a test function that is analytic, *i.e.* $a_{-k} \equiv 0$ for $k > 0$. Then, if the amplitude has no poles, the quantity $\chi_0^2 = \sum_{k=1}^{N} y_{-k}^2$ will be zero[3]. If we think that the scattering data has one pair of complex conjugate poles in the $z-$plane (as is the case where there is one resonance present) then we can write our test function as

$$\begin{aligned} f(z) &= \frac{\alpha}{z - z_0} + \frac{\alpha^*}{z - z_0^*} + h(z) \\ &= \sum_{k=1}^{\infty} \frac{2\,\Re[\alpha z_0^{k-1}]}{z^k} + h(z) \quad , \end{aligned} \tag{2.15}$$

where $h(z)$ is some analytic function. By comparing (2.15) with (2.13) we see that, in this case, the analytic continuation is carried out by setting $a_{-k} = 2\,\Re[\alpha z_0^{k-1}]$ and then it is the quantity $\chi_1^2 = \sum_{k=1}^{N} (y_{-k} - 2\,\Re[\alpha z_0^{k-1}])^2$ that has a χ^2 distribution with N degrees of freedom.

[3]Actually, due to inevitable experimental noise, χ_0^2 will not be exactly zero, but should fit a χ^2 distribution with N degrees of freedom.

2.3.2 A Better Continuation: The Blaschke Factor Method

There is, however, a problem with the continuation described in Section 2.3.1. In effect in (2.15) we are expanding a quantity like $(1 - z_0)^{-1}$ and in the actual computation this expansion will have to be truncated at some order. This is fine as long as $|z_0| \ll 1$, but in practice $|z_0|$ is close to one and the above procedure becomes unreliable. As an illustration, if $|z_0| = 0.99$ (a not unreasonable value for a resonance pole), then the quantity $(1 - z_0)^{-1} = 100$ whereas the expansion truncated to 40 terms gives 33.8. Even if we include the first 200 terms then the expansion still only gives 86.7.

Consequently, we adopt an alternative approach which is to cancel any pole in the data explicitly by the introduction of the so-called Blaschke pole killing factor, $B(z)$. This factor is real analytic when we are considering a function that is real analytic and is defined so that $|B(z)| = 1$ for $|z| = 1$, so there is no arbitrary rescaling of our χ^2. We define the function

$$\tilde{y}(z) = \frac{Y(z)B(z)}{g(z)} \tag{2.16}$$

and expand this as a Laurent series about the origin, *i.e.*

$$\tilde{y}(z) = \sum_{k=-\infty}^{\infty} \tilde{y}_k \, z^k \quad . \tag{2.17}$$

We test this function, $\tilde{y}(z)$, against the hypothesis of analyticity, *i.e.* we investigate the quantity $\sum_{k=1}^{N} (\tilde{y}_{-k})^2$ which will indeed obey a χ^2 distribution with N degrees of freedom, if we have the correct Blaschke factor.

To test for different numbers of poles we use different Blaschke factors. If we believe the amplitude to be analytic, we use $B(z) \equiv 1$. For a pair of complex conjugate poles the Blaschke factor looks like

$$B(z) = \frac{(z - z_0)(z - z_0^*)}{(1 - zz_0)(1 - zz_0^*)} \tag{2.18}$$

where z_0 is the position of our test pole. From (2.18) we can see that the Blaschke factor contains poles at $z = 1/z_0$ and $z = 1/z_0^*$, which at first sight would seem to complicate our calculation. However, we are searching for poles inside the unit

circle *i.e.* $|z_0| < 1$ so these extra poles are outside the circle which we use as our contour of integration when calculating the coefficients and so do not contribute to them. Blaschke factors for larger numbers of poles are constructed analogously to (2.18).

By cancelling out any poles before we expand our amplitude we avoid the need to make the expansion explicit in (2.15) and so significantly improve the convergence and stability of the method.

It is worth making a few comments about the method at this point. Firstly, we are not making a traditional 'fit-to-data'. In particular, in the Blaschke factor method we create a function from the experimental data and the Blaschke factor and fit the singular coefficients of this function to zero.

Secondly we are not assuming any particular form for the scattering amplitude, merely that it is a complex function, analytic except for those cuts shown in Fig 2.1 (which define our mapping) and those poles corresponding to the resonances we wish to determine. This is why the form of the background, as long as it can be assumed to be smooth, should not affect our results.

Chapter 3

Hunting the κ: Phenomenology and Results

3.1 Experimental Input

Our experimental information on the $S-$wave πK partial wave amplitude comes in the form of the magnitudes, $a(s)$, and phases, $\phi(s)$, measured, for instance, by the LASS experiment. We normalise the amplitude on the first sheet such that

$$f^I(s) = \frac{a(s)\, e^{i\phi(s)}}{\rho(s)} \quad , \tag{3.1}$$

where the phase space $\rho(s) = 2q/\sqrt{s}$ and q, the c.m. 3-momentum, is given by

$$q = \frac{1}{2}\sqrt{\frac{[s-(m_K+m_\pi)^2][s-(m_K-m_\pi)^2]}{s}} \quad . \tag{3.2}$$

In general, πK scattering has two possible isospin channels, $I = 1/2$ and $I = 3/2$. The resonances we are interested in are isodoublets. The $I = 1/2$ results must be extracted from the total $S-$wave data by subtracting an assumed form for the $I = 3/2$ amplitude[1] which introduces an extra layer of uncertainty. Furthermore, this separation of the data into definite isospin components is only reliable over a restricted energy range. However, there are no known resonances

[1]Whilst it is possible to obtain purely isospin-3/2 results, by studying the reactions $\pi^+K^+ \to \pi^+K^+$ or $\pi^-K^- \to \pi^-K^-$, it is not possible to study isospin-1/2 πK scattering in isolation.

in the the $I = 3/2$ channel: so we can assume that it acts as an additional, smooth background to the $I = 1/2$ resonances that we are looking for and, as explained in Chapter 2, should not affect the pole positions found. This means that there is no need to separate the isospin components and we, therefore, carry out our analysis on the total $S-$wave data. Nevertheless, the $I = 1/2$ component does provide a valuable check, both of our results using the total $S-$wave amplitude and of the assertion that there are no exotic $I = 3/2$ resonances.

As is well-known, resonance poles do not appear on the physical sheet in the energy plane. Consequently, to determine the number of resonances in a given channel we must consider the scattering amplitude on the relevant unphysical sheet. For purely elastic scattering this would be sheet II[2]. As inelastic channels open, the sheet structure of the amplitude becomes more complicated and we must ensure that we are considering the correct sheet. The first inelastic channel for πK scattering is ηK at around 1.05 GeV. However, $SU(3)$ flavour symmetry predicts that this channel will not couple strongly to πK and this is confirmed by the experimental results [38]. So any inelasticity can be safely neglected, until one reaches the $\eta' K$ threshold at around 1.46 GeV. This channel opens in the region of a possible $K_0^*(1430)$ and we must take this threshold into account when we change sheets. Any resonance would then be on sheet III.

So we require a means of selecting the nearby unphysical sheet that can be used in a two channel system where the amplitude may consist of the sum of two isospin components. To illustrate how we go about doing this we consider the $K-$matrix formalism for such an amplitude. On the physical sheet we can write the partial wave amplitude as

$$F^I = \frac{\lambda_a(K^a_{11} - i\,\rho_2 \det K^a)}{1 - i\,\rho_1\,K^a_{11} - i\,\rho_2\,K^a_{22} - \rho_1\,\rho_2 \det K^a} + \frac{\lambda_b(K^b_{11} - i\,\rho_2 \det K^b)}{1 - i\,\rho_1\,K^b_{11} - i\,\rho_2\,K^a_{22} - \rho_1\,\rho_2 \det K^b} \quad , \tag{3.3}$$

where the Roman numeral denotes the Riemann sheet, the letter denotes the

[2]The Riemann sheets are labelled by (r_1, r_2), where the r_j are the signs of the imaginary parts of the complex phase spaces ρ_j in particular channels. $j = 1$ for πK, $j = 2$ for $\eta' K$. Sheet I is $(+,+)$, sheet II is $(-,+)$ and sheet III is $(-,-)$.

isospin and the Arabic numeral denotes the channel. To go to the second sheet we must make the change $\rho_1 \to -\rho_1$ and so the amplitude looks like

$$F^{II} = \frac{\lambda_a(K^a_{11} - i\,\rho_2\,\det K^a)}{1 + i\,\rho_1\,K^a_{11} - i\,\rho_2\,K^a_{22} + \rho_1\,\rho_2\,\det K^a} + \frac{\lambda_b(K^b_{11} - i\,\rho_2\,\det K^b)}{1 + i\,\rho_1\,K^b_{11} - i\,\rho_2\,K^a_{22} + \rho_1\,\rho_2\,\det K^b} \quad . \tag{3.4}$$

While to move from the first to the third sheet we must make the changes $\rho_1 \to -\rho_1$ and $\rho_2 \to -\rho_2$ giving us

$$F^{III} = \frac{\lambda_a(K^a_{11} + i\,\rho_2\,\det K^a)}{1 + i\,\rho_1\,K^a_{11} + i\,\rho_2\,K^a_{22} - \rho_1\,\rho_2\,\det K^a} + \frac{\lambda_b(K^b_{11} + i\,\rho_2\,\det K^b)}{1 + i\,\rho_1\,K^b_{11} + i\,\rho_2\,K^a_{22} - \rho_1\,\rho_2\,\det K^b} \quad . \tag{3.5}$$

Comparing (3.3) and (3.5), we find that, above the second threshold, $F^{III} = F^{I*}$.

However, below the second threshold we should use the the analytic continuation of the phase-space for this channel *i.e.* $\rho_2 = i\,|\rho_2|$. Then the amplitude on the physical sheet becomes

$$F^{I} = \frac{\lambda_a(K^a_{11} + |\rho_2|\,\det K^a)}{1 - i\,\rho_1\,K^a_{11} + |\rho_2|\,K^a_{22} - i\,\rho_1\,|\rho_2|\,\det K^a} + \frac{\lambda_b(K^b_{11} + |\rho_2|\,\det K^b)}{1 - i\,\rho_1\,K^b_{11} + |\rho_2|\,K^a_{22} - i\,\rho_1\,|\rho_2|\,\det K^b} \quad , \tag{3.6}$$

and the amplitude on the second sheet is

$$F^{II} = \frac{\lambda_a(K^a_{11} + |\rho_2|\,\det K^a)}{1 + i\,\rho_1\,K^a_{11} + |\rho_2|\,K^a_{22} + i\,\rho_1\,|\rho_2|\,\det K^a} + \frac{\lambda_b(K^b_{11} + |\rho_2|\,\det K^b)}{1 + i\,\rho_1\,K^b_{11} + |\rho_2|\,K^a_{22} + i\,\rho_1\,|\rho_2|\,\det K^b} \quad . \tag{3.7}$$

From (3.6) and (3.7) we see that below the second threshold $F^{II} = F^{I*}$. So for any energy, the amplitude on the *nearby* unphysical sheet is just the complex conjugate of the amplitude on the physical sheet and the simplest way to pick the correct sheet is to change the sign of the phase in (3.1), *i.e.*

$$f(s) = \frac{a(s)\,e^{-i\phi(s)}}{\rho(s)} \quad . \tag{3.8}$$

Note that, although it was stated that any inelasticity due to the ηK channel could be neglected, this method of selecting the sheet actually takes into account

the thresholds due to *all* open channels at a given energy. However, we can only specify which sheet we are on by knowledge of the thresholds we have passed. In other words, although we know we are on the correct sheet to locate a resonance pole we may not know exactly which sheet we are on.

We then map the data, including errors, as described above. As noted previously it is not possible to cover the circle completely with physical region data. The exact proportion of the circle covered by data depends on the choice of the mapping parameter β. From Fig. 2.3 we see that there are two distinct arcs of the upper semi-circle that are not covered by the experimental data. Firstly there is the arc corresponding to the energy region between threshold and the start of the data. Our treatment of this region is slightly different for our tests using the model data in Section 3.2 than when we are considering the real data in Section 3.3 and, hence, will be detailed in the appropriate sections. Secondly there is the arc corresponding to the left-hand and circular cuts in Fig. 2.1. As we do not have information about what happens on these unphysical cuts, we simply make a guess. So that the guess does not unduly affect the results, we de-weight these guessed points by giving them very large errors and by ensuring that they are widely spaced (see Fig. 3.1). With the top semi-circle now spanned by "data" points, we make an interpolation to give us a continuous function. We complete the circle by reflecting the interpolated data in the upper semi-circle onto the lower half so as to obey the Schwarz Reflection Principle, thus ensuring the real analyticity of the amplitude.

A suitable form for the weight function $g(z)$, which fulfils all the conditions described above is

$$g(z) = \exp\left(\sum_{n=0}^{N} c_n z^n\right) \tag{3.9}$$

where the c_n are found from a Fourier cosine fit to $\ln\epsilon(z)$, *i.e.*

$$\begin{aligned} c_0 &= \frac{1}{\pi}\int_0^{2\pi} \ln\epsilon(z = e^{i\theta})\, \mathrm{d}\theta \\ c_{n\geq 1} &= \frac{2}{\pi}\int_0^{2\pi} \cos n\theta \ln\epsilon(z = e^{i\theta})\, \mathrm{d}\theta \end{aligned} \tag{3.10}$$

In practice we take $N = 100$.

We are now in a position to calculate the singular coefficients of the Laurent expansion of the data about the origin in the usual way *i.e.*

$$y_{-k} = \frac{1}{2\pi} \oint_c \frac{Y(z)}{g(z)} z^k \, |\mathrm{d}z| \quad , \tag{3.11}$$

for the subtraction method of Section 2.3.1 and

$$\tilde{y}_{-k} = \frac{1}{2\pi} \oint_c \frac{Y(z)\, B(z)}{g(z)} z^k \, |\mathrm{d}z| \quad , \tag{3.12}$$

for the Blaschke factor method of Section 2.3.2.

3.2 Tests on Model Data

3.2.1 The Model Data

Before attempting to analyse real experimental data, we would like to have an idea of the capabilities and limitations of the method outlined in Chapter 2. To this end a model data-set was created describing an amplitude containing a light, broad resonance, κ_1, and a heavier, narrower resonance, κ_2[3]. The amplitude was constructed using Jost functions, so the positions of the poles of the amplitude can be found analytically, and the lighter resonance is treated as the background at the second, *i.e.*

$$f^I(s) = f_1^I(s) + e^{2i\delta_1(s)} f_2^I(s) \tag{3.13}$$

on the first sheet, where

$$f_j^I(s) = \frac{-2k(s)d_j}{\rho(s)\,(k(s)+c_j+id_j)(k(s)-c_j+id_j)} \quad , \tag{3.14}$$

$$\delta_1(s) = \arctan\left(\frac{2k(s)d_1}{c_1^2+d_1^2-k^2}\right) \quad , \tag{3.15}$$

$$k(s) = \frac{1}{2}\sqrt{s-(m_K+m_\pi)^2} \quad . \tag{3.16}$$

The four parameters $\{c_j, d_j\}$ are chosen, so that the amplitude has poles at $s_1 = (0.9 \pm 0.25i)^2$ (GeV)^2 and $s_2 = (1.4 \pm 0.15i)^2$ (GeV)^2. Data are created for

[3]This generalises a model analysis discussed by Nogová *et al.* to two resonances.

energies equivalent to the full LASS data-set [38], with the error on both the magnitude and phase fixed at 5%. Below the energy of the LASS data, we create a few equally spaced points between threshold and 825 MeV. The magnitudes, a, and phases, ϕ for these "physical region data" are shown in Fig. 3.1 as a function of energy. The amplitude in the unphysical region is set to a real constant (incidentally equal to the amplitude at threshold) with very large errors (± 5). Fig. 3.2 shows the real and imaginary parts of the mapped test amplitude on the second sheet, including both the physical and unphysical regions, as a function of the angle around the circle, θ.

3.2.2 Results using the Model Data

The model data described in Section 3.2.1 were used to test both of the methods described in Section 2.3. The results obtained by fitting over the first 40 singular coefficients are shown in Tables 3.1, for the subtraction method, and 3.2 for the Blaschke factor method. Also tabulated for comparison are the results obtained when the errors on the points in the unphysical region are halved. It was expected that the Blaschke factor method would be the more accurate and Tables 3.1 and 3.2 show that this is indeed the case. They also show that the subtraction method is more sensitive to the input along the unphysical cuts, thus reducing its reliability. The Blaschke factor method was also found to be far more stable to variations of non-physical parameters (such as the number of terms in our definitions of the χ^2 and the weight function). All subsequent results have been obtained using the Blaschke factor method.

It is normal when working with χ^2 to quote its value per degree of freedom. As our quantity is not a statistically rigorous χ^2 we refrain from doing this and prefer to interpret our results in terms of the change of the absolute value. For information, however, we note that all tabulated results were obtained by fitting the first forty singular coefficients, as defined in (3.12), to zero. When testing for no resonances we have no free parameters, so there are 40 degrees of freedom.

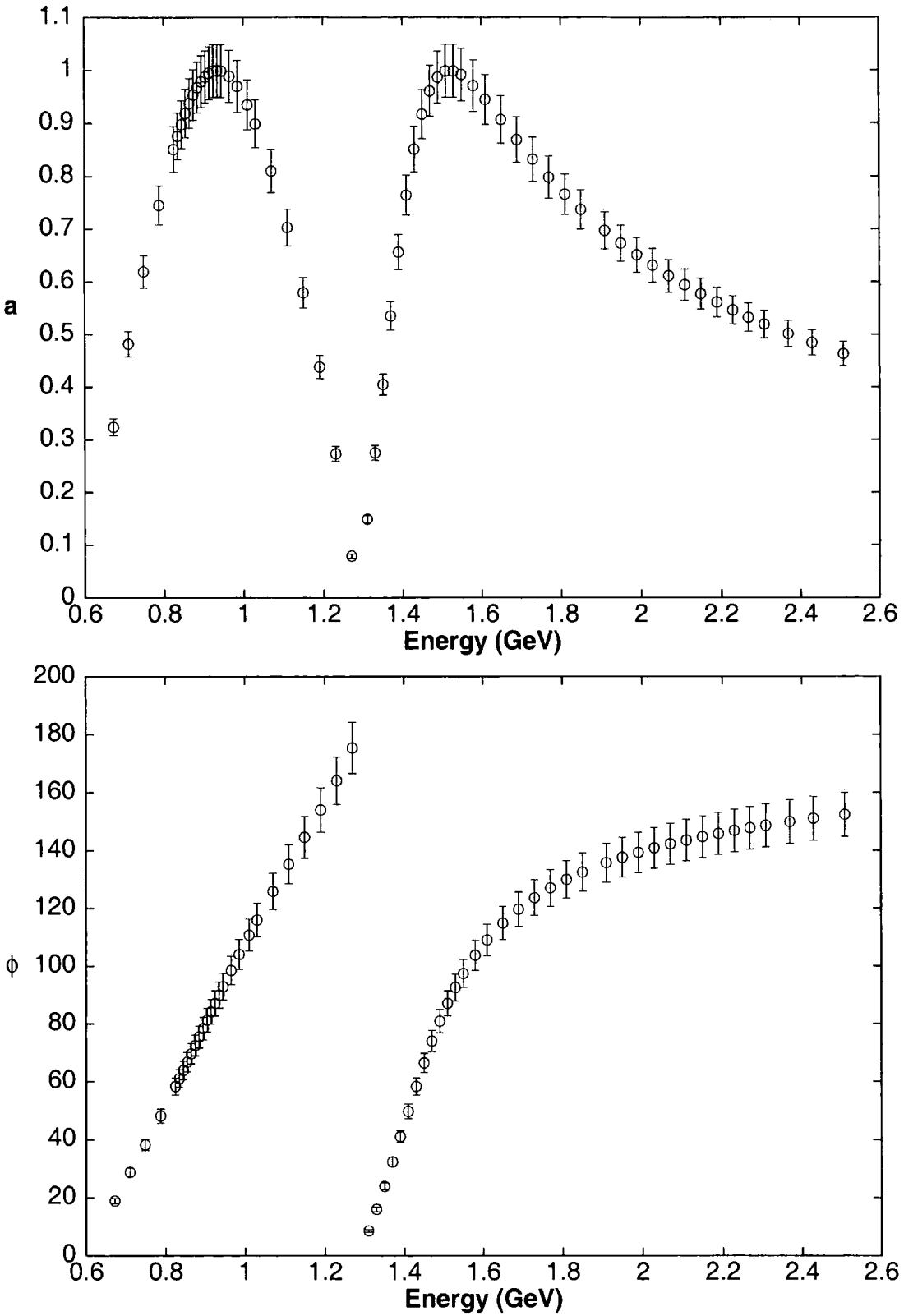

Figure 3.1: Magnitudes, a and phases, ϕ, of the test data as functions of the centre-of-mass energy. As calculated from (3.13-3.16).

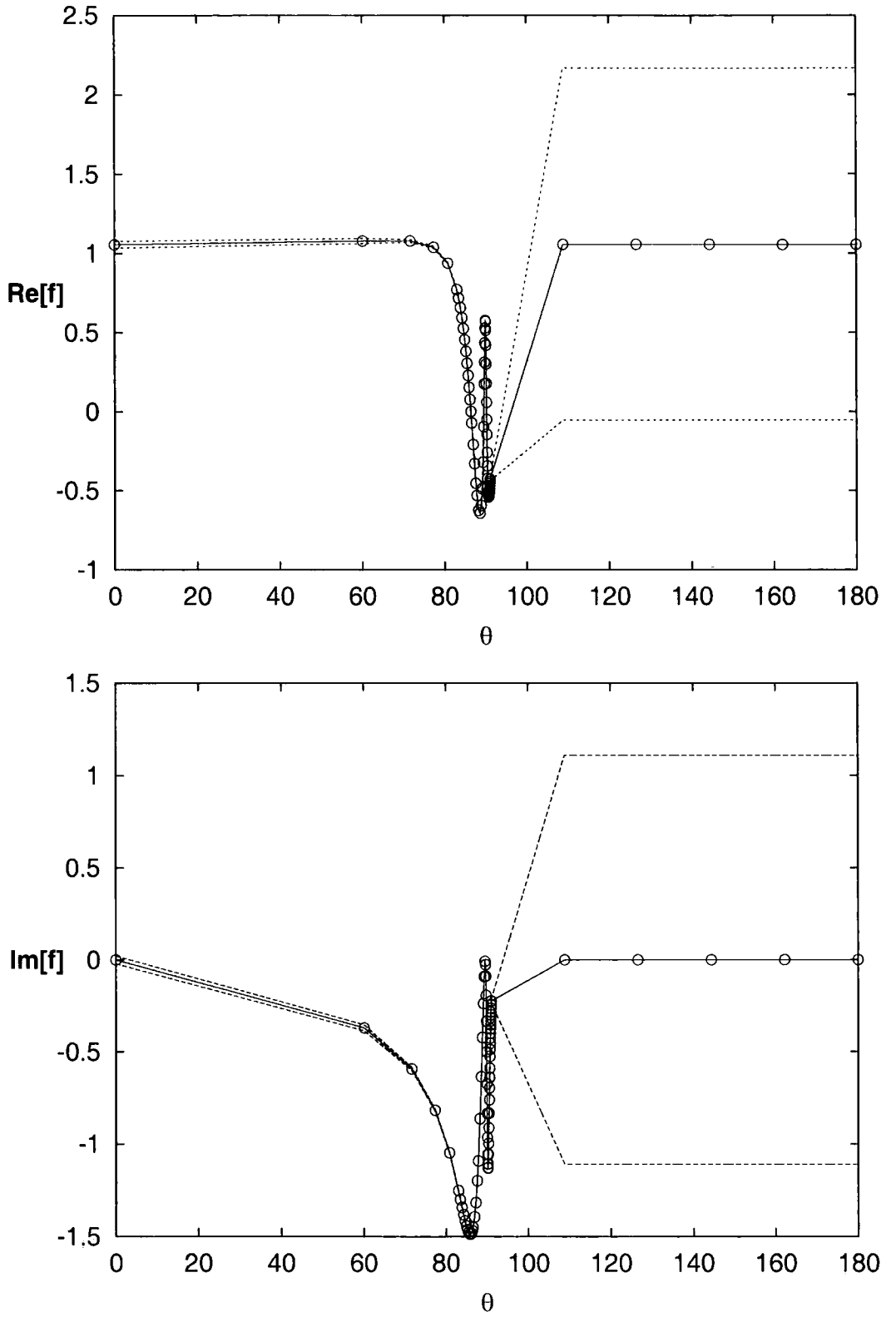

Figure 3.2: Real and imaginary parts of f^{II} as a function of θ, the angular position around the circle in degrees, for the model data-set. The circles represent data points, the solid line shows the interpolation to the data and the dashed line shows the interpolated weighted errors.

Option	No. of resonances	z_{pole} (r,θ)	$\sqrt{s_{pole}}$ (MeV)	χ^2
1	0	—	—	4081
	1	(0.986,88.16°)	$1079 \pm 78i$	33.8
	2	(0.961,89.85°)	$1013 \pm 343i$	0.5
		(0.972,90.16°)	$1127 \pm 394i$	
2	0	—	—	3759
	1	(0.988,87.73°)	$1015 \pm 57i$	57.0
	2	(0.976,89.67°)	$1151 \pm 279i$	0.6
		(0.951,90.13°)	$933 \pm 366i$	

Table 3.1: Pole positions and χ^2's for model data using the subtraction method outlined in Sect. 2.3.1. Option 1 has the unphysical errors set to 5. Option 2 has the unphysical errors set to 2.5.

Option	No. of resonances	z_{pole} (r,θ)	$\sqrt{s_{pole}}$ (MeV)	χ^2
1	0	—	—	4081
	1	(0.988,89.31°)	$1201 \pm 131i$	281
	2	(0.993,89.98°)	$1396 \pm 142i$	0.5
		(0.943,88.64°)	$903 \pm 234i$	
2	0	—	—	3759
	1	(0.989,89.13°)	$1173 \pm 111i$	417
	2	(0.993,89.97°)	$1392 \pm 140i$	1.0
		(0.942,88.61°)	$900 \pm 233i$	

Table 3.2: Pole positions and χ^2's for model data using the Blaschke factor method outlined in Sect. 2.3.2. Option 1 has the unphysical errors set to 5. Option 2 has the unphysical errors set to 2.5.

For one resonance there are two parameters (the real and imaginary parts of the pole position), hence 38 degrees of freedom and for two resonances we have four parameters and so 36 degrees of freedom.

From Table 3.2, it is clear that the method is readily capable of identifying the number and position of poles even when the associated resonances are broad and overlapping. The decrease in χ^2 when going from no resonance to one resonance is large, but far less significant than the fall when we ask is there one or two resonances. From this Table, one would have no doubt that there are two resonances in the model data and their positions are well determined.

3.2.3 Higher Mass Resonances

Of course the physical amplitude may contain many resonances with masses greater than those of our κ_1 and κ_2. As was stated earlier, this method is expected to be less sensitive to these poles. To see to what extent this is true further tests were carried out using a different form of trial data. For these tests an amplitude containing an effective range background plus two resonances, a κ_2 and a heavier κ_3, was simulated. We use modified Breit-Wigner formulae to describe the resonant parts of the amplitude, so for the κ_j resonance we have

$$f_j = \frac{m_j \Gamma_j}{m_j^2 - s - i m_j \rho \Gamma_j} \quad , \tag{3.17}$$

where m_j and Γ_j are the mass and width of the resonance and ρ is the phase space defined earlier. The total amplitude is given by

$$f = \frac{1}{\rho(\cot \delta_{BG})} + e^{2i\delta_{BG}} f_2 + e^{2i(\delta_{BG}+\delta_2)} f_3 \quad , \tag{3.18}$$

with δ_2 being the argument of f_2 (the phase-shift of the κ_2) and

$$q \cot \delta_{BG} = \frac{1}{a} + \frac{b q^2}{2} \quad . \tag{3.19}$$

Using these formulae, data were created up to various energies. Points were created at the same energies as the LASS data and above that at 40 MeV intervals. The error on both the magnitude and phase were set to 5%. These trial data are illustrated, over the same energy range as the data from the LASS experiment, in Fig. 3.3. The trial amplitude was analysed assuming zero, one and two resonances and the χ^2's and pole positions found are shown in Table 3.3 as functions of the maximum energy of the data-set.

From these results we can clearly see that, as the maximum energy of the data falls, the κ_3 becomes less necessary to describe the data in the $z-$plane. With data up to 22.5 GeV, there is a strong case for claiming that there are both the κ_2 and the κ_3, but their parameters are not accurately found. When the data only extends to 2.5 GeV, the ratio of χ_1^2 to χ_2^2 is small enough that one would not be confident in claiming that the data exhibited more than one resonance. While

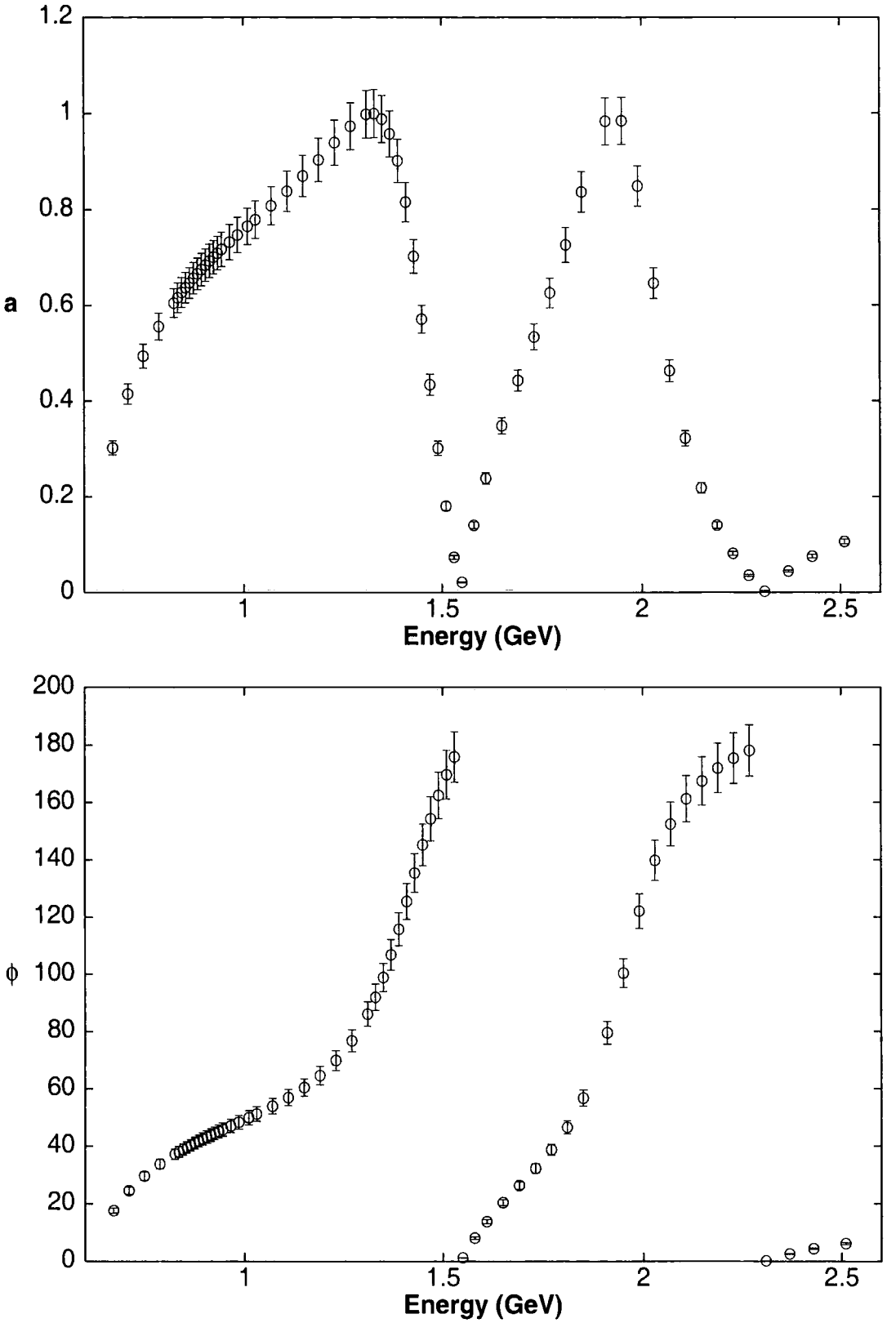

Figure 3.3: Magnitudes, a, and phases, ϕ of the trial data described by (3.17)-(3.19).

Max. Energy	χ_0^2	χ_1^2	χ_2^2	λ	λ_1	λ_2
				MeV		
22.51	2320	43.3	2.02	$1395 \pm 53i$	$1938 \pm 234i$	$1453 \pm 137i$
12.51	2361	37.0	1.98	$1394 \pm 56i$	$1951 \pm 253i$	$1456 \pm 133i$
8.51	2389	35.0	1.96	$1394 \pm 58i$	$1959 \pm 264i$	$1457 \pm 130i$
6.51	2380	18.9	1.84	$1395 \pm 69i$	$2024 \pm 331i$	$1458 \pm 114i$
3.51	2207	11.4	1.77	$1396 \pm 78i$	$2099 \pm 441i$	$1454 \pm 102i$
2.91	1959	7.33	1.70	$1398 \pm 84i$	$2178 \pm 788i$	$1445 \pm 91i$
2.51	1529	4.58	1.57	$1399 \pm 92i$	$899 \pm 1457i$	$1422 \pm 82i$

Table 3.3: χ^2's and pole positions for trial data described in the text. Maximum energies are in GeV. λ is the pole position found when searching for one resonance. λ_1 and λ_2 are the pole positions found when searching for two resonances. χ_0^2, χ_1^2, and χ_2^2 are the χ^2's assuming no, one and two resonances respectively. The actual pole positions are $1421 \pm 119i$ MeV for the κ_2 and $1957 \pm 106i$ MeV for the κ_3.

the position of the κ_2 is more stable, the parameters found for the κ_3 bear no resemblance to the correct values. Meanwhile, the pole parameters found when testing for just one pole are always recognisable as the κ_2. If we introduce realistic experimental errors and inelasticity, then the κ_3 becomes even more hidden.

Similar results were found using a trial amplitude where the κ_2 in (3.18) was replaced by a κ_1. However, if the trial amplitude contained no resonance below it then the κ_3 was found and its parameters were well determined. From the results of these tests it appears that, when an amplitude contains more than one resonance, the higher mass resonances cannot be found using this method if their mass is above some value. For πK scattering this value is somewhere above 1600 MeV.

3.2.4 Estimating the Errors

Evaluating the errors on the pole positions that we obtain using this method is nevertheless not straightforward. The experimental errors are folded into the actual calculation and so their propagation cannot easily be followed. Moreover, as pointed out by Nogová *et al.* [51], the χ^2's obtained are not strictly statistical, so the standard confidence level techniques are not appropriate.

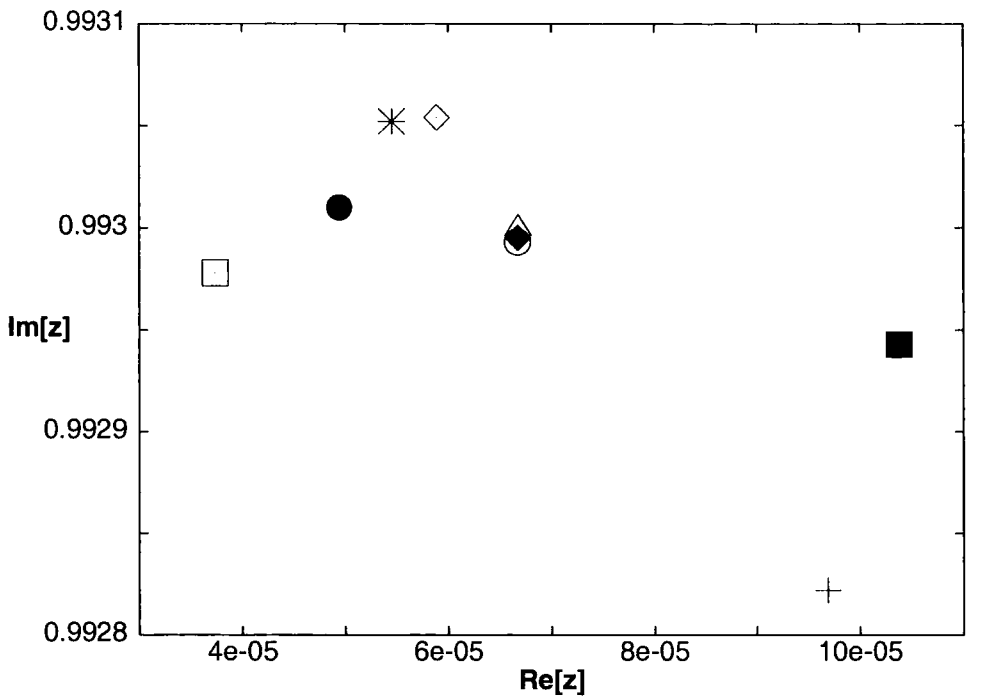

Figure 3.4: Expanded view of the z-plane showing the spread of pole positions found by varying the input parameters. ♦: standard values. ◇: double the number of terms in $g(z)$. +: halve the number of terms in $g(z)$. ∗: Double the number of terms in χ^2. □: Halve the number of terms in χ^2. ○: Double the value of $f(z)$ in the unphysical region. △: Halve the value of $f(z)$ in the unphysical region. ■: Halve the errors in the unphysical region. •: Double the number of points in the unphysical region.

Thus we resort to an order of magnitude estimate of the errors obtained by varying the inputs that introduce uncertainty into the calculation. These inputs include the number of terms in the Fourier expansion defining the weight function, the number of terms in the summation used to evaluate χ^2 and the treatment of the unphysical region. The uncertainty in the pole position found in the z-plane due to these changes in parameters is shown in Fig. 3.4, from which we see that the typical uncertainty in the z-plane is of the order of $(4 + 20i) \times 10^{-5}$.

Due to the non-linearity of the mapping a fixed absolute uncertainty in the z-plane will give different uncertainties in the E-plane depending on the actual position. The minimum uncertainty in the position of the κ_2 is of the order of 3 MeV on the real part and 5 MeV on the imaginary. For the κ_3 the minimum

uncertainty would be 5 MeV on the real part and 15 MeV on the imaginary part. In contrast, for the κ_1 the minimum uncertainty is of the order 1 MeV on both parts. The pole positions listed in Table 3.2 would suggest that these minimum uncertainties underestimate the true uncertainty and we can expect to do no better than an accuracy of 10 MeV on the real part and 20 MeV on the imaginary part of the pole position.

3.3 Investigation of Experimental Data

3.3.1 Description of the LASS Data

From LASS [38], we have the magnitude and phase of the π^+K^- S-wave amplitude from 825 MeV up to 2.51 GeV as shown in Fig. 3.5. The mapped amplitude on the second sheet, as normalised in (3.8), is shown in Fig. 3.6.

Due to a Barrelet ambiguity [53], the LASS group find two partial wave amplitude solutions which only differ above 1.84 GeV. For our calculation we use their Solution A, but this choice of solution does not affect our conclusions regarding the $\kappa(900)$ and the $K_0^*(1430)$. The total $S-$wave amplitude for $\pi^+K^- \to \pi^+K^-$ is related to the amplitudes with definite isospin by

$$f_S(s) = f^{(1/2)} + \frac{1}{2} f^{(3/2)} \quad . \tag{3.20}$$

Since resonances are only expected in the $I = 1/2$ channel, it is natural to consider the effect of separating out this component. Such a separation requires a modelling of the $I = 3/2$ contribution. Below 1.58 GeV, the LASS group group provide a model of this contribution based on the parametrisation of Estabrooks [54]. This allows us to apply the method used in Section 3.2 to the $I = 1/2$ amplitude alone, but only below 1.58 GeV. As a control on this procedure, we also consider the full $S-$wave data over this reduced energy range, which we refer to as the "Short $S-$wave data-set".

The effective range type formula provided by LASS gives one possible extrapolation of their data to threshold. This serves as *a guide* (and only a guide) to

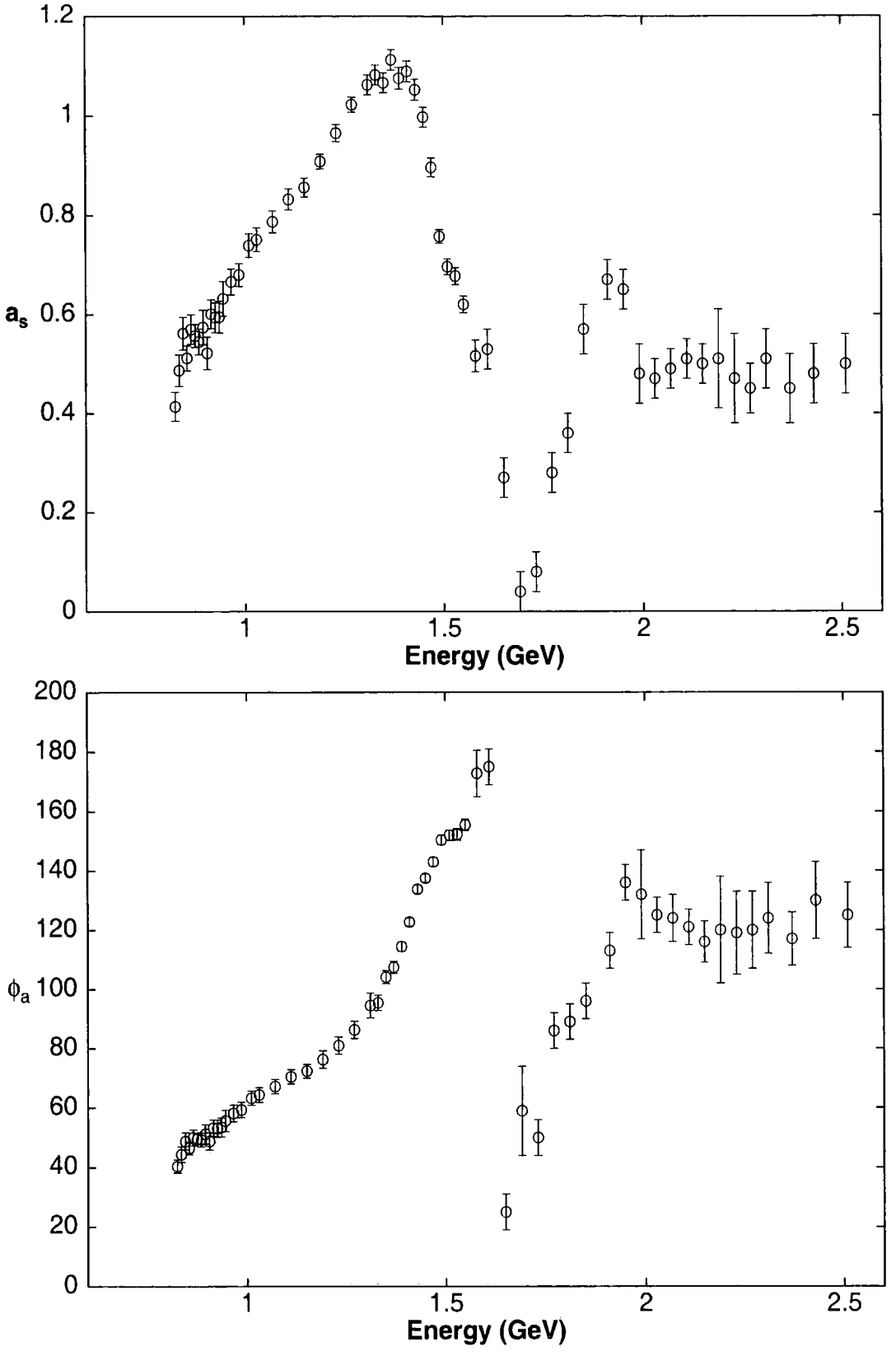

Figure 3.5: Magnitudes, a, and phases, ϕ of the total $S-$wave πK partial wave amplitude as measured by the LASS experiment [38].

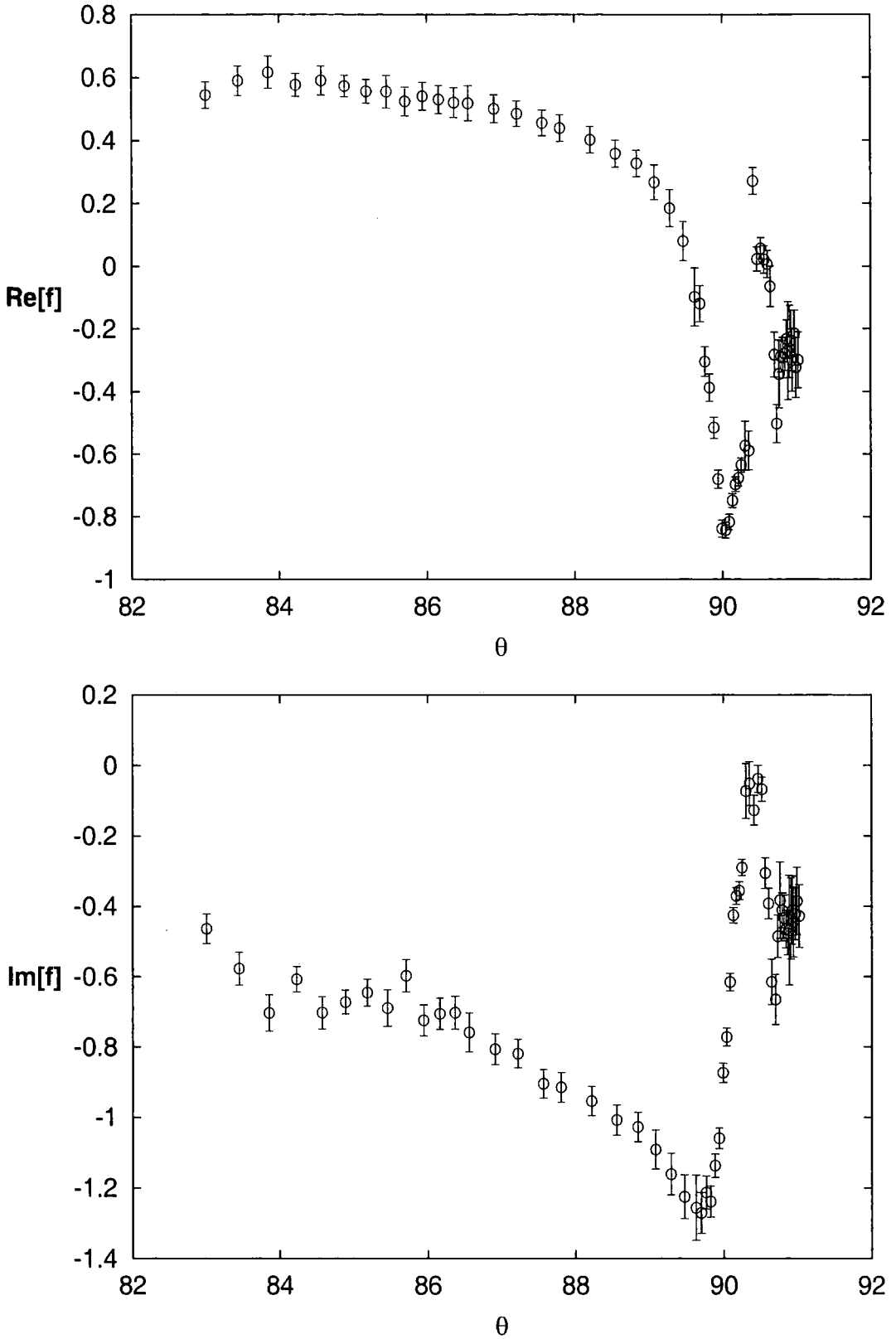

Figure 3.6: Real and imaginary parts of f^{II} as a function of θ for the LASS $S-$wave data-set. Only the actual data points are shown, with unweighted errors.

possible data points between threshold and the start of the data. Note that the superscript (I) is an isospin label. All equations for amplitudes in this section refer to the physical sheet. Their formula is

$$f^{(I)} = \frac{1}{\rho\,(\cot\delta_{BG}^{(I)} - i)} + \frac{e^{2i\delta_{BG}^{(I)}}}{\rho\,(\cot\delta_{BW} - i)} \quad , \tag{3.21}$$

where δ_{BG} for each isospin channel is given by (3.19) and the resonance term, which only appears in the $I = 1/2$ case, is given by

$$\cot\delta_{BW} = \frac{(m_r^2 - s)\,E\,q_r}{m_r^2\,\Gamma_r\,q} \quad , \tag{3.22}$$

with q given by (3.2), and q_r being its value at $s = m_r^2$. The LASS fit gave the threshold parameters $a^{(1/2)} = 2.19$ GeV^{-1} and $b^{(1/2)} = 3.74$ GeV^{-1} in the $I = 1/2$ channel and $a^{(3/2)} = -1.03$ GeV^{-1} and $b^{(3/2)} = -0.94$ GeV^{-1} in the $I = 3/2$ channel. For the $I = 1/2$ resonance the parameters $m_r = 1.412$ GeV and $\Gamma_r = 0.294$ GeV were found[4]. It is important to recognise that though the LASS effective range fit assumes the tail of a Breit-Wigner-like pole, this does not prejudge that such a pole exists in our analysis. We call this treatment of the low energy region Case A.

While the above Case A is largely experimentally motivated, a more theoretically well-founded guide to low energy meson-meson scattering is provided by Chiral Perturbation Theory (χPT). This makes predictions for near threshold πK scattering that we can input into our analysis. However, the effect of the higher order corrections becomes larger and less predictable as one goes much above threshold. Consequently, we only generate data points based on χPT within 100 MeV of threshold, with a precision encompassing the range of present calculations [55, 56, 49]. We call this Case B. We let the method determine the interpolation between the low energy χPT results and where LASS data begin. This avoids the need for us to enter into any debate about whether higher order corrections in χPT are summed better by the Inverse Amplitude method or by

[4]These six parameters were provided by W. Dunwoodie and are not the values quoted in the original paper.

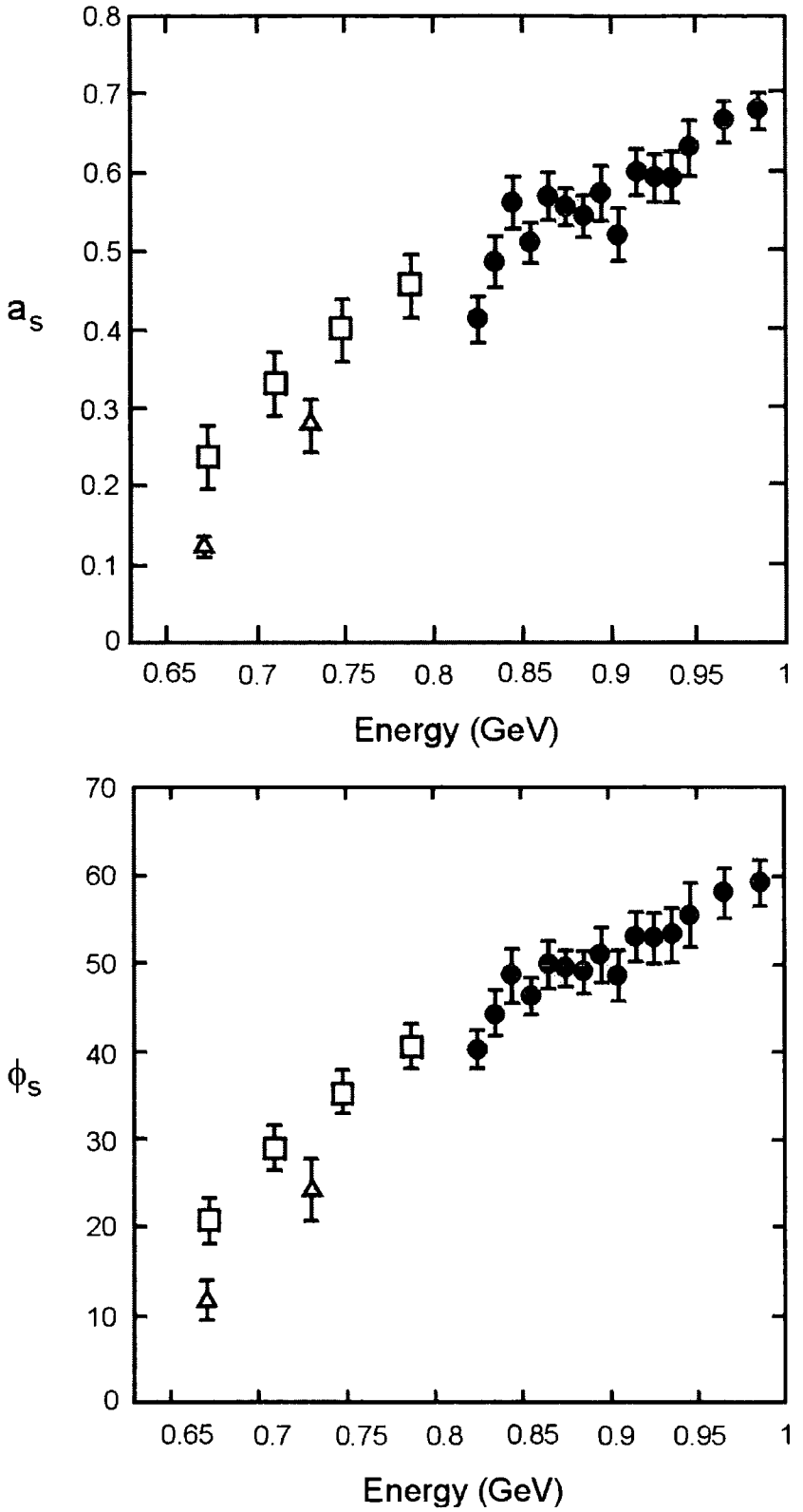

Figure 3.7: The magnitude and phase of the total $S-$wave scattering amplitude showing Case A (□), Case B (△) and the LASS data below 1 GeV (•).

explicitly including resonances. Such differences are large at 825 MeV. It is in this sense that we describe our method as "model independent".

In implementing either Case A or Case B, we only create a few low energy "data" points so as not overly to prejudice the results. These two alternative sets of "data" are shown in Fig. 3.7 together with the LASS experimental results below 1 GeV. In both Cases the unphysical cuts are treated as for the model data-set of Section 3.2.

3.3.2 Results from the LASS Data

In Table 3.4, we present the results of our analysis for the data shown in Fig. 3.5. The Table shows the pole positions found for the full $S-$wave data, with full and halved errors on the unphysical points.

Case	Option	No. of resonances	z_{pole} (r, θ)	$\sqrt{s_{pole}}$ (MeV)	χ^2
A	1	0	—	—	1373
		1	$(0.994, 90.07°)$	$1433 \pm 149i$	4.7
		2	$(0.995, 90.15°)$	$1432 \pm 148i$	1.8
			$(0.987, 82.02°)$	$805 \pm 13i$	
	2	0	—	—	1629
		1	$(0.993, 90.06°)$	$1423 \pm 157i$	9.0
		2	$(0.993, 90.06°)$	$1423 \pm 154i$	8.8
			$(0.998, 86.98°)$	$969 \pm 6i$	
B	1	0	—	—	1340
		1	$(0.994, 90.10°)$	$1444 \pm 151i$	16.9
		2	$(0.994, 90.07°)$	$1436 \pm 133i$	1.0
			$(0.854, 95.14°)$	$609 \pm 238i$	
	2	0	—	—	1694
		1	$(0.993, 90.08°)$	$1428 \pm 168i$	33.2
		2	$(0.994, 90.05°)$	$1429 \pm 132i$	1.0
			$(0.870, 93.35°)$	$645 \pm 260i$	

Table 3.4: Pole positions and χ^2's for LASS $S-$wave data [38] from 0.825 GeV to 2.51 GeV. Cases A and B are explained in the text and shown in Fig. 3.7.
Option 1: The amplitude in the unphysical region equals the amplitude at threshold, with an error of 5.
Option 2: The amplitude in the unphysical region equals the amplitude at threshold, with an error of 2.5.

Option	No. of resonances	z_{pole} (r,θ)	$\sqrt{s_{pole}}$ (MeV)	χ^2
1	0	—	—	210
	1	(0.992,90.22°)	$1467 \pm 224i$	2.1
	2	(0.992,90.22°)	$1464 \pm 221i$	1.1
		(0.993,82.14°)	$808 \pm 7i$	
2	0	—	—	367
	1	(0.991,90.23°)	$1455 \pm 245i$	5.3
	2	(0.991,90.19°)	$1439 \pm 237i$	2.4
		(0.911,100.1°)	$503 \pm 238i$	

Table 3.5: Pole positions and χ^2's for LASS $I = 1/2$ data [38]. Option 1 has unphysical errors set to 5. Option 2 has unphysical errors set to 2.5.

Option	No. of resonances	z_{pole} (r,θ)	$\sqrt{s_{pole}}$ (MeV)	χ^2
1	0	—	—	170
	1	(0.991,90.03°)	$1471 \pm 242i$	2.2
	2	(0.985,90.07°)	$1422 \pm 553i$	1.9
		(0.997,90.08°)	$1457 \pm 80i$	
2	0	—	—	283
	1	(0.991,90.26°)	$1459 \pm 264i$	5.6
	2	(0.990,90.23°)	$1440 \pm 263i$	2.4
		(0.886,101.8°)	$513 \pm 208i$	

Table 3.6: Pole positions and χ^2's for the short LASS $S-$wave data [38]. Option 1 has unphysical errors set to 5. Option 2 has unphysical errors set to 2.5.

The results for the $I = 1/2$ and the shorter $S-$wave data-sets are shown in Tables 3.5 and 3.6. These Tables show a remarkable consistency, as one would hope for effects that are real. It is worth pointing out that our method will 'find' exactly as many poles as it is asked to. So if we search for two resonances then positions for two resonances will be given no matter how many resonances are present in the data. Resonances that really are present in the data will be stable to changes in unphysical parameters and result in sizeable falls in the χ^2. Conversely, if the χ^2 does not fall significantly between one and two resonances then we can conclude that the second resonance 'found' is not really present and the pole position given is meaningless. Likewise, any resonance found whose pole

position changes wildly with variations in unphysical parameters will also be an artifact.

3.3.3 The Estabrooks *et al.* Data

As a further check of our results, the same technique was applied to the total $S-$wave data from an earlier SLAC experiment [37]. These data extend closer to threshold, so it is only necessary to create a point at threshold. Fig. 3.8 shows the magnitudes and phases for this data-set in the region below 1 GeV and should be compared with the treatment of the low energy region for the LASS data-set shown in Fig. 3.7. Again, we use both an experimentally motivated *Case A* and a theoretically motivated *Case B*. In *Case A* we use an effective range formula, see (3.19), with $a^{(1/2)} = 2.39$ GeV^{-1} and $a^{(3/2)} = -1.00$ GeV^{-1} (as only a point at threshold is calculated only the scattering lengths need be known). No resonance was assumed in this fit, so any lingering doubts that assuming the tail of the $K_0^*(1430)$ in the low energy extrapolation introduces a prejudice is clearly not there in this case. In *Case B* the scattering lengths calculated from χPT are used. The results for the Estabrooks *et al.* data-set [37] are shown in Table 3.7.

3.4 Discussion

For the real πK experimental results, Tables 3.4–3.7 display a consistency in identifying a single resonance which looks very like the $K_0^*(1430)$. The fall in χ^2 in going from no resonance to one resonance is always sizeable, ranging from a factor of 32 to a factor of 290. In contrast when going from one to two resonances, the χ^2 does not generally fall by a significant amount. Importantly, recall that the present analysis technique is always most sensitive to the lightest resonance and this is clearly the $K_0^*(1430)$. So whilst the $K_0^*(1430)$ is overwhelmingly apparent, a lighter, broad resonance is not. When studying *Case B* for the LASS data there is also a sizeable fall in the χ^2 when going from one to two resonances, but the

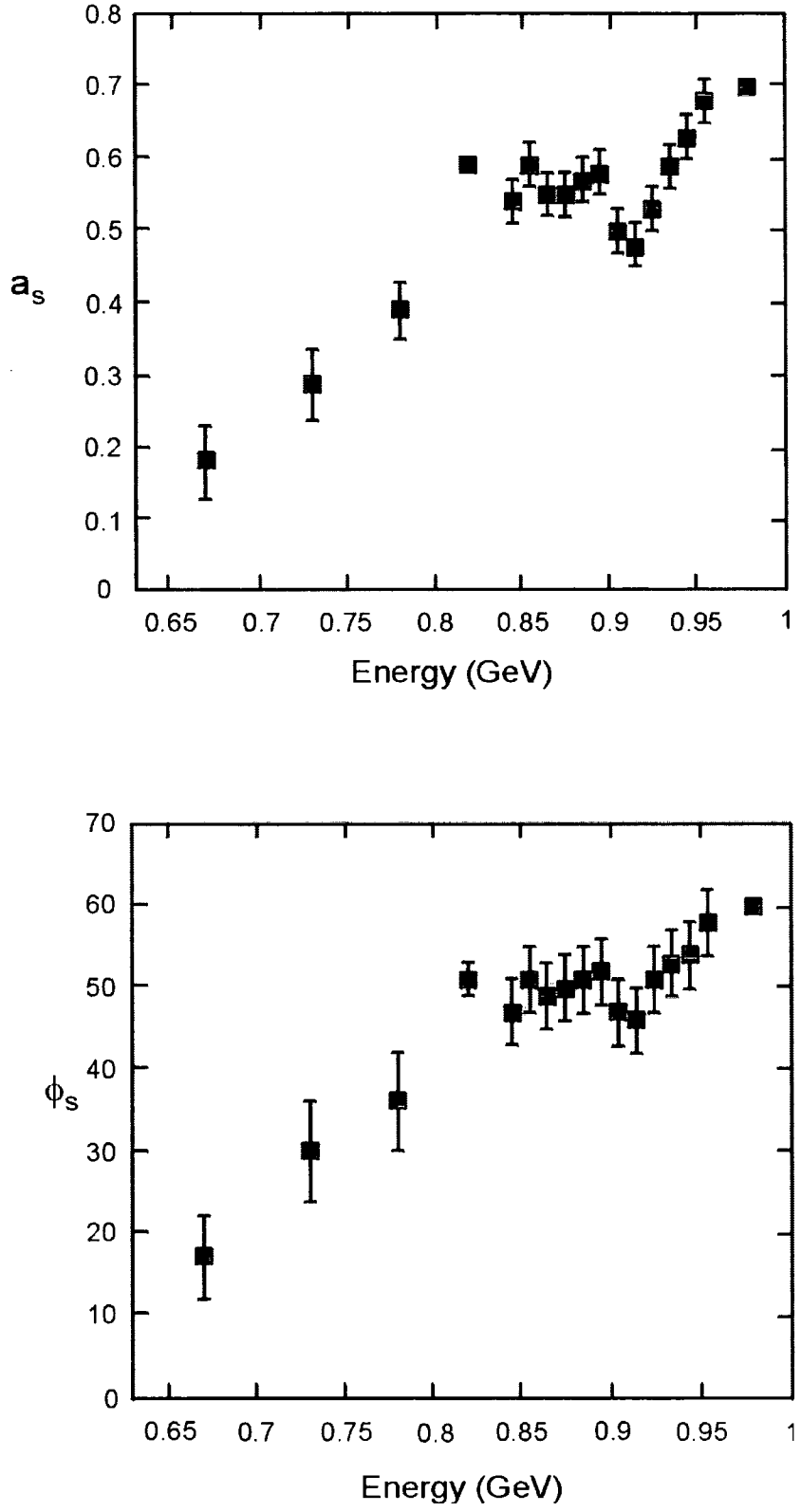

Figure 3.8: Magnitudes, a_s, and phases, ϕ_s (in degrees), for the $S-$wave πK scattering amplitude below 1 GeV from Estabrooks *et al.* [37], to be compared with Fig. 3.7.

Case	Option	No. of resonances	z_{pole} (r,θ)	$\sqrt{s_{pole}}$ (MeV)	χ^2
A	1	0	—	—	553
		1	(0.991,90.20^o)	$1446 \pm 232i$	16
		2	(0.986,89.83^o)	$1277 \pm 231i$	12
			(1.017,90.46^o)	$1344 \pm 444i$	
	2	0	—	—	812
		1	(0.990,90.16^o)	$1411 \pm 250i$	14
		2	(0.988,89.92^o)	$1323 \pm 221i$	14
			(1.01,90.47^o)	$1564 \pm 316i$	
B	1	0	—	—	551
		1	(0.991, 90.20°)	$1447 \pm 231i$	17
		2	(0.986, 89.84°)	$1286 \pm 227i$	14
			(1.015, 90.44°)	$1382 \pm 423i$	
	2	0	—	—	816
		1	(0.990, 90.16°)	$1411 \pm 253i$	16
		2	(0.991, 89.81°)	$1324 \pm 159i$	16
			(1.001, 89.89°)	$1395 \pm 18i$	

Table 3.7: Pole positions and χ^2's for Estabrooks *et al.* [37] $S-$wave data. The Cases A and B are described in the text.
Option 1 has unphysical errors set to 5. Option 2 has unphysical errors set to 2.5.

second resonance is below the experimental range (in fact for one of the options it is below threshold). This suggests that it is a result of something encoded in that particular extrapolation to threshold and not an effect in the data. Interestingly, such a state is not apparent when considering the data of Estabrooks *et al.* which extends closer to threshold, albeit with larger errors.

Halving the assumed errors in the unphysical region should not affect the pole positions obtained, and from Table 3.2 we can see that this is indeed the case. From Tables 3.4–3.7 we see that for the assumption that there is only one resonance present, then halving the unphysical errors, has a small effect. However, when we force the amplitude to have two resonances the effect is much more noticeable. Generally, the resonance which looks like $K_0^*(1430)$ tends to stay in a similar position, but the second one moves around wildly. This is what one would expect if this second resonance is merely an artifact of forcing the method to find two pairs of poles when only one is really present in the data.

It was mentioned earlier that we would expect the method to be less sensitive to high mass resonances. This is borne out by these results. The LASS group provide strong evidence for a state at 1.95 GeV. With data to 2.51 GeV we would expect to see this state showing up, but the compression of the high energy portion of the amplitude has diluted the effect of the $K_0^*(1950)$ so much that it is not needed to describe the data in the complex $z-$plane. This is to be expected from our study using model data, described in Sect. 3.2.3. The non-linearity of the mapping procedure (and the presence of the $K_0^*(1430)$) severely limits our ability to find states above 1800 MeV in πK scattering. However, below that, and particularly down towards the lower end of the experimental range, the method is totally reliable and quite unambiguous. The results we obtain when using the higher statistics of the LASS experiment (Tables 3.4-3.6) indicate that there is just one strange, scalar resonance. This is readily identified as the $K_0^*(1430)$. In particular, the best available πK scattering data does not contain a light κ with a mass above 825 MeV. The supporting evidence shown in Table 3.7, would suggest that there is no κ.

Chapter 4

Sum Rules in the Scalar-Isoscalar Channel

4.1 Introduction

As explained in Chapter 1, there are more scalar mesons than can be accommodated in a single quark-model nonet. It is tempting to say that these 'spare' experimental states are the unconventional mesons permitted by QCD, but which *are* the spare states? In the work that follows we hope to shed some light on this question by attempting to determine which of the 5 scalar-isoscalar mesons currently listed in the PDG is the lightest $u\overline{u} + d\overline{d}$ meson in this channel. To address this question we will use the QCD sum rule technique.

QCD sum rules are integral expressions that relate the hadronic and partonic regimes, *i.e.* the low energy world of resonances with the high energy world of (tractable) QCD. Since their conception over twenty years ago [57], QCD sum rules have become an established technique both for calculating hadronic properties in channels where the QCD expressions are under control and, conversely, estimating QCD parameters (such as the masses of the quarks) in channels where there is good experimental information.

These days, QCD sum rules are used in two complementary forms which are

based on different aspects of the analyticity of the hadronic vacuum polarisation, $\Pi(s)$. In the first form, a dispersion relation (with the necessary number of subtractions) is written for $\Pi(s)$ and then the inverse Laplace (or Borel) transform operator is applied. This gives the Laplace (or Borel) QCD sum rule, which in the case where no subtractions are required can be written as

$$\mathcal{L}\left[\Pi(q^2)\right] = \frac{1}{\pi}\int_0^\infty e^{-s/M^2}\,\mathrm{Im}\Pi(s)\,\mathrm{d}s\ , \tag{4.1}$$

where $q^2 = s$, M is known as the Borel mass and

$$\mathcal{L}\left[f(q^2)\right] = \lim_{\substack{-q^2,n\to\infty \\ -q^2/n=M^2}} \frac{(-q^2)^{n+1}}{n!}\left(\frac{\mathrm{d}}{\mathrm{d}q^2}\right)^n f(q^2). \tag{4.2}$$

The left hand side of (4.1) can be calculated within QCD whilst on the right hand side it is usual to use the 'resonance + continuum' ansatz. In this representation, the imaginary part of the correlator up to some cut-off, s_0, is assumed to be dominated by one or more resonances which are either modelled by data or a phenomenological parameterisation. Above this cut-off, the imaginary part of the correlator is assumed to be equal to the continuum, calculable within QCD. For a fuller discussion of QCD Laplace sum rules see for instance [58, 59]. In this work we make use of the so-called QCD Finite Energy Sum Rules, which will be discussed in Section 4.2.

QCD sum rules were first applied to the scalar mesons in [60]. Here Laplace sum rules were used, with resonances being represented as δ-functions and the continuum being calculated entirely within perturbative QCD. As only the Operator Product Expansion (see Section 4.4) was taken into account on the theory side, *exact* mass degeneracy between the lightest isoscalar and isovector was found, with $m_{f_0} = m_{a_0} = 1.00 \pm 0.03$ GeV. The $s\bar{s}$ state was predicted with a mass of around 1.35 GeV. These, findings were supported by [61] who used QCD sum rules to calculate the couplings of the $f_0(980)$ and $a_0(980)$ to two photons. Again modelling the resonances with δ-functions the authors concluded that a $q\bar{q}$ interpretation of these two mesons could not be ruled out with the data then available.

The effects of going beyond the OPE were studied in [62], where instantons (see Section 4.6) were included on the theoretical side, but not in the QCD continuum on the phenomenological side. Once again the resonances were treated as δ-functions and only the isospin-1 channel was considered. It was concluded that the lightest $q\bar{q}$ state in this channel had a mass $\lesssim 1$ GeV.

For the light scalar mesons, the zero-width approximation is not a good one and the first attempt to go beyond it in a sum rule investigation was by Elias *et al* [63]. Here resonances were represented by Breit-Wigner formulae, which, whilst better than a δ-function, still does not adequately describe the complex structure in the scalar sector. A further abstraction was introduced by replacing these Breit-Wigner shapes with a Riemann sum of rectangular pulses. Laplace sum rules were used, but in an integral form which requires the calculation of perturbative expressions at rather low energy scales. Again instantons were included, but not in the continuum. In the isovector channel, the $a_0(980)$ was found to decouple from the sum rule and the mass of the lightest quarkonium isovector was consistent with the $a_0(1450)$. In the isoscalar channel the conclusions were not so clear cut, it was predicted that the lightest quarkonium here should have a width less than half of its mass, and although the $f_0(980)$ could not be ruled out a lighter state was preferred. Similar conclusions were reached in [64]. This study used both Laplace and Finite Energy sum rules, again requiring perturbative expressions to be evaluated at low energies. The authors noted, that for a consistent treatment of the Borel sum rules, the instanton effects should also be included in the QCD continuum contribution. The sum rules were dominated by an isoscalar with mass around 1 GeV and an isovector with mass around 1.5 GeV, thus suggesting the $f_0(980)$ and $a_0(1450)$ as the lightest $q\bar{q}$ states in their respective channels. However, in the same work, a comparison to a more realistic resonance shape predicted resonance parameters for the lightest quarkonium of $m \sim 860$ MeV and $\Gamma \sim 340$ MeV. These parameters are not consistent with the $f_0(980)$ but could describe a Breit-Wigner fit to the $f_0(400-1200)$.

In [65] pinched weight Finite Energy sum rules were used to calculate the decay constants of the $a_0(980)$ and $a_0(1450)$, which were then compared with the decay constant of the, presumably $q\bar{q}$, $K_0^*(1430)$. Instantons were included and all QCD integrals were carried out in the complex plane, which improves the convergence of perturbative expressions. The isovector decay constants were found to be of comparable size, suggesting a similar structure for both. The author concluded that this favoured a UQM-like scenario, where two physical hadrons can arise from one 'seed' state.

In this work we will apply QCD Finite Energy sum rules to the scalar-isoscalar channels. On the phenomenological side we will incorporate data directly, whilst on the theory side we will make use of the OPE and instantons.

4.2 Finite Energy Sum Rules

Finite Energy Sum Rules (FESRs) are a direct consequence of Cauchy's Theorem and, in fact, pre-date QCD [66]. QCD FESRs were first studied in [67] and require also the concept of global duality between hadronic and partonic physics at moderate energies. The link between quarks and hadrons is made via the vacuum polarisation, $\Pi(s)$. This is defined by the correlation function of two currents, *i.e.*

$$\Pi(s) = i \int \mathrm{d}^4x \; e^{iqx} \langle 0|T\{J(x)J(0)\}|0\rangle \; , \tag{4.3}$$

where $s = q^2 = -Q^2$ and the currents are chosen so as to select the desired channel.

This quantity is analytic everywhere in the complex s-plane except along the positive real (time-like) axis. Thus, for any weight function, $w(s)$, that is analytic within the contour shown in Fig. 4.1, Cauchy's Theorem (1.1) becomes

$$\frac{1}{2\pi i}\left[\int_0^{s_0} w(s+i\epsilon)\,\Pi(s+i\epsilon) - w(s+i\epsilon)\,\Pi(s+i\epsilon)\mathrm{d}s + \oint_{|s|=s_0} w(s)\,\Pi(s)\mathrm{d}s\right] = 0 \; . \tag{4.4}$$

The fact that $\Pi(s)$ is real for real $s < 0$, and assuming $w(s)$ is real for all real s,

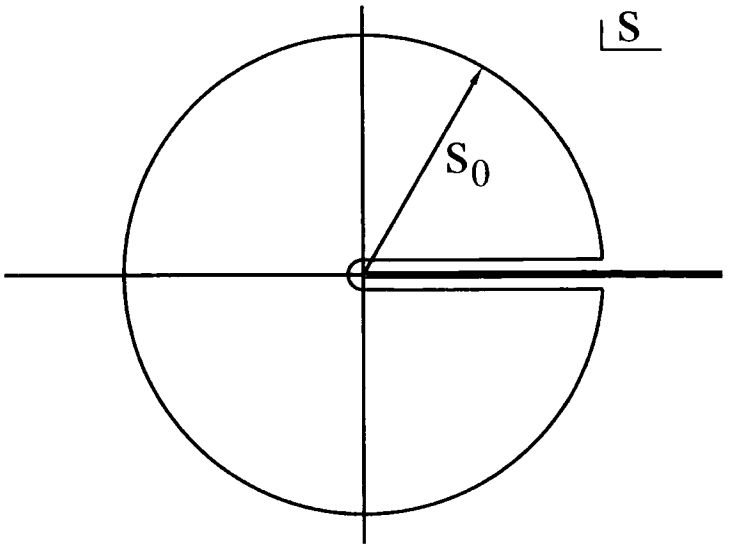

Figure 4.1: The complex s-plane showing the so called 'Pacman' contour which is used to derive the FESRs.

allows the Schwarz Reflection Principle to be exploited, giving

$$\frac{1}{\pi}\int_0^{s_0} w(s)\,\mathrm{Im}\Pi(s)\,\mathrm{d}s = -\frac{1}{2\pi i}\oint_{|s|=s_0} w(s)\,\Pi(s)\,\mathrm{d}s\ . \tag{4.5}$$

Global quark-hadron duality implies that the integral of an hadronic expression is equal to the integral of an expression written in terms of partonic degrees of freedom. On the left-hand side of (4.5) we have an integral in the physical region, and here we choose to describe the integrand using hadronic physics (either with experimental data or a phenomenological parameterisation). On the right-hand side we have an integral in the non-physical region (complex s), and here we use field theory (*i.e.* QCD) to calculate the integrand. The assumption that (4.5) still holds for some values of s_0 is a statement of global quark-hadron duality.

As Cauchy's Theorem applies within QCD, we could choose to deform the contour of integration on the right-hand side of (4.5) to run around the real axis. This would then lead to sum rules of the type exploited in [63, 64]. However, this would then require that perturbative expressions be evaluated at rather low energies, where they are not expected to converge. Hence we choose not to follow this path, but to calculate the theoretical side via a complex integral.

Early sum rule work used positive integer powers of s as weight functions. In this work we wish to investigate the lightest meson in the $I = J = 0$ channel, and so we choose a decaying exponential, $w(s) = \exp(-s/M^2)$. On the phenomenological side, this weight function will suppress the region of the integral $s > M^2$, and so by varying M^2 we can control which regions of the integrand contribute most significantly to the sum rule. If we also include integer powers of s in the weight function then we can build up a family of sum rules. We will refer to these sum rules which have weight functions $w(s) = s^k e^{-s/M^2}$ as R-type sum rules and denote them by the symbol R_k.

Almost by definition, at energies where resonances dominate the spectral density, QCD does not give a good description, at least as we are currently able to use it. If this *were* the case then the technology of QCD sum rules would be redundant. This means that, for moderate values of s_0, our QCD description of $\Pi(s)$ must fail, at the very least, in the region of the positive real axis (see Fig 4.1). However, it is believed [68] that it is *only* in the region of the positive, real axis that the QCD description fails and that in the rest of the s-plane QCD provides a good description of the correlator. Thus we introduce a second type of sum rule containing a weight function that has a zero at s_0. We will refer to this second type of sum rule, which have weight functions $w(s) = s^k \left(1 - s/s_0\right) e^{-s/M^2}$, as T-type and denote them by the symbol T_k. Elsewhere in the literature they are often referred to as 'pinched weight' sum rules. When we wish to refer to both types of sum rule, we will use the symbol S_k.

Introducing this zero into the weight function of the T-type sum rules has a number of advantages. Firstly, on the theoretical side we avoid the problem, just described, of the failure of QCD on the part of the circle near the positive real axis. Secondly, on the phenomenological side, we have introduced a second factor with a tendency to suppress the higher energy portion of the integral. Thirdly, we would expect the zero to reduce the dependency on the parameter s_0 [69, 70]. For these reasons we expect that the T-type sum rules will prove to be more

reliable.

To recap, our two types of sum rule are

$$\left[R_k(s_0, M^2)\right]_{had} = \frac{1}{\pi}\int_{4m_\pi^2}^{s_0} s^k\, e^{-s/M^2}\, \left[\mathrm{Im}\Pi(s)\right]_{had}\, \mathrm{d}s\ , \tag{4.6}$$

$$\left[R_k(s_0, M^2)\right]_{QCD} = \frac{-1}{2\pi i}\oint_{|s|=s_0} s^k\, e^{-s/M^2}\, \left[\Pi(s)\right]_{QCD}\, \mathrm{d}s\ , \tag{4.7}$$

$$\left[T_k(s_0, M^2)\right]_{had} = \frac{1}{\pi}\int_{4m_\pi^2}^{s_0} s^k\, e^{-s/M^2}\left(1-\frac{s}{s_0}\right)\left[\mathrm{Im}\Pi(s)\right]_{had}\, \mathrm{d}s\ , \tag{4.8}$$

$$\left[T_k(s_0, M^2)\right]_{QCD} = \frac{-1}{2\pi i}\oint_{|s|=s_0} s^k\, e^{-s/M^2}\left(1-\frac{s}{s_0}\right)\left[\Pi(s)\right]_{QCD}\, \mathrm{d}s\ . \tag{4.9}$$

The parameter s_0 is not entirely free: it must be large enough that the QCD expressions we are able to calculate are expected to be a good approximation to the full correlator yet small enough that we have experimental information. The art of sum-ruling is to find (sensible) values of s_0 for which $[S_k(s_0, M^2)]_{had} = [S_k(s_0, M^2)]_{QCD}$ over a wide range of the unphysical parameter M^2. When this occurs we say that the sum rules are *saturated*.

4.3 The Scalar-Isoscalar Light Quark Correlator

In this study we are concerned with the scalar-isoscalar light quark correlator, this is built by substituting into (4.3) the RG-invariant $I = J = 0$ non-strange quark current, *i.e.*

$$J(x) = \frac{m_q}{2}\left\{\overline{u}(x)u(x) + \overline{d}(x)d(x)\right\} = \frac{m_q}{\sqrt{2}}\,\overline{n}(x)n(x)\ , \tag{4.10}$$

where $m_q \equiv \frac{1}{2}(m_u + m_d)$ and we use the symbol n to denote an effective light-quark. The second equality follows because we ignore the two-gluon intermediate state, whose contribution to the OPE of the up/down combination is $\mathcal{O}(m_q^2)$ and so can be safely neglected.

Although the current (4.10) is RG-invariant, the correlator it gives rise to is not. As well as making the calculation of the correlator within QCD more difficult, this would also lead to an unwanted scale dependence in our final results. The second derivative of this correlator, $\Pi''(s)$, *is* RG-invariant. As $\Pi''(s)$ is also

analytic within the contour shown in Fig. 4.1 we could choose to write our sum rule completely in terms of this quantity, but $\mathrm{Im}\,\Pi''(s)$ is not directly related to any physical quantity and so we would lose our link to experiment. Instead we use partial integration to rewrite the theoretical side of the sum rules in terms of $\Pi''(s)$. To do this we write the integral on the theoretical side as

$$i_1 = \oint v''(s)\Pi(s)\,\mathrm{d}s\ . \tag{4.11}$$

We now partially integrate this expression twice to give,

$$i_1 = v'(s)\Pi(s) - v(s)\Pi'(s) + \oint v(s)\Pi''(s)\mathrm{d}s\ , \tag{4.12}$$

and arrange the constants of integration which appear in $v(s)$ and $v'(s)$ such that these functions disappear at $s = s_0$. Then our sum rule is

$$\frac{1}{\pi}\int_0^{s_0} w(s)\ [\mathrm{Im}\Pi(s)]_{had}\ \mathrm{d}s = -\frac{1}{2\pi i}\oint_{|s|=s_0} v(s)\ [\Pi''(s)]_{QCD}\ \mathrm{d}s\ . \tag{4.13}$$

Table 4.1 shows the phenomenological and corresponding theoretical weight functions required for the sum rules we consider.

Sum Rule	$w(s)$	$v(s)$
R_0	e^{-s/M^2}	$M^2[M^2e^{-s/M^2}.$ $+ e^{-s_0/M^2}(s - s_0 - M^2)]$
R_1	$s\,e^{-s/M^2}$	$M^2[M^2e^{-s/M^2}(s + 2M^2)$ $+ e^{-s_0/M^2}(ss_0 + sM^2 - 2M^2s_0$ $- 2M^4 - s_0^2)]$
T_0	$\left(1 - \frac{s}{s_0}\right) e^{-s/M^2}$	$M^4[e^{-s/M^2}(s_0 - s - 2M^2)$ $+ e^{-s_0/M^2}(s_0 - s + 2M^2)]$
T_1	$s\left(1 - \frac{s}{s_0}\right) e^{-s/M^2}$	$M^4[e^{-s/M^2}(ss_0 - s^2 + 2M^2s_0 - 4sM^2 - 6M^4)$ $+ e^{-s_0/M^2}(s_0^2 - ss_0 - 2sM^2$ $+ 4s_0M^2 + 6M^4)]$

Table 4.1: The weight functions for the phenomenological side, $w(s)$, and the corresponding weight functions, $v(s)$, which must accompany the second derivative on the theoretical side of the sum rule.

4.4 The Operator Product Expansion

As mentioned above the central object in this analysis is the vacuum polarisation $\Pi(s)$. In order to calculate this quantity within QCD we make use of the Operator Product Expansion (OPE) [71]. This replaces the matrix element of the product of currents in (4.3) by a linear combination of local operators,

$$\Pi(s = -Q^2) = \sum_n C_n(Q^2)\langle \mathcal{O}_n \rangle \ . \tag{4.14}$$

The Q^2-dependent functions, C_n, are known as Wilson coefficient functions and can be calculated using standard perturbation theory. The operators in (4.14) have the same quantum numbers as the product of currents appearing in (4.3) and are ordered by increasing dimensionality. As each term in the OPE must have the same dimensions, the dimension of the coefficient functions must decrease. Consequently, we expect higher dimension operators to be suppressed by factors of Q^{2d} where d is the dimension of the operator. The first operator to appear in the OPE is the identity operator which thus gives the purely perturbative contribution to the correlator. The vacuum expectation values of higher dimension operators are called condensates, which can be thought of as fluctuations of the non-trivial QCD vacuum with infinite correlation lengths.

The structure of the OPE is such that all the non-perturbative (*i.e.* long-distance or low-energy) physics is described by the vacuum expectation values of the operators $\mathcal{O}_n$, whilst the Wilson coefficients describe the short distance effects. As explained in [72] (and references therein), in order to fully separate the long and short distance physics it is necessary to calculate the vacuum expectation values of the operators in a minimally subtracted scheme. The down side of this is that the operators of a given dimension mix under renormalisation, *i.e.* individual condensates are no longer renormalisation group invariant. However, the total contribution from all operators of a given dimension remains invariant. In the following, all expressions have been calculated within the $\overline{\text{MS}}$ scheme.

4.5 The OPE in the Scalar Isoscalar Channel

Within the framework of (4.14) we expand the correlator as

$$\Pi(s) = \Pi_0(s) + \Pi_2(s) + \Pi_4(s) + \Pi_6(s) + \dots \,, \tag{4.15}$$

where Π_d is the total contribution to the correlator from all operators of dimension d. A similar expansion is made for $\Pi''(s)$. We will truncate these expansions at dimension 6.

4.5.1 The Perturbative Contribution

The Wilson coefficient of the unit operator gives us the purely perturbative contribution to the OPE for the second derivative. The general form of this coefficient is [73]

$$\overline{C_1}(Q^2) = \frac{Nm_q^2}{Q^2} \sum_{i=0}^{\infty} a_s^i \sum_{j=1}^{i+1} d_{ij}\, j \left[\log^{j-1}\!\left(\frac{Q^2}{\mu^2}\right) + (j-1)\log^{j-2}\!\left(\frac{Q^2}{\mu^2}\right) \right] \,, \tag{4.16}$$

where μ^2 is the renormalisation scale and $a_s = \alpha_s(\mu^2)/\pi$. Π'' is renormalisation group invariant, which implies that

$$\left[\mu^2 \frac{\partial}{\partial \mu^2} + \beta(a_s)\frac{\partial}{\partial a_s} + \gamma(a_s) m_q \frac{\partial}{\partial m_q} \right] \overline{C_1}(Q^2) = 0 \,, \tag{4.17}$$

where $\beta(a_s)$ is the QCD β-function, $\gamma(a_s)$ is the quark mass anomalous dimension and our conventions for these functions are explained later in (4.36) - (4.40).

In (4.17) each term $a_s^i \log^j(Q^2/\mu^2)$ must vanish separately. This means that the various d_{ij} are interrelated, and in fact there is only one independent constant for each order in a_s, usually taken to be d_{i1}. The first two of these independent constants have been known for a long time, the third was calculated in [74] and the fourth in [75]. Thus the perturbative contribution to the correlator is known

to four-loop order. The full expression can be found in [76] and is given by

$$\begin{aligned}\Pi_0''(Q^2) = \frac{6m_q^2}{2(4\pi)^2Q^2}\Bigg\{1 + a_s\left[\frac{11}{3} - 2\log\frac{Q^2}{\mu^2}\right] \\ + a_s^2\left[\left(\frac{5071}{144} - \frac{35}{2}\zeta(3)\right) - \frac{139}{6}\log\frac{Q^2}{\mu^2} + \frac{17}{4}\log^2\frac{Q^2}{\mu^2}\right] \\ + a_s^3\left[\left(-\frac{4781}{9} + \frac{b_1}{6} + \frac{475}{4}\zeta(3)\right) + \left(-\frac{2720}{9} + \frac{475}{4}\zeta(3)\right)\log\frac{Q^2}{\mu^2}\right. \\ \left. + \frac{695}{8}\log^2\frac{Q^2}{\mu^2} - \frac{221}{24}\log^3\frac{Q^2}{\mu^2}\right]\Bigg\}\,, \end{aligned} \tag{4.18}$$

where

$$b_1 = \frac{4\,748\,953}{864} - \frac{91\,519}{36}\zeta(3) - 15\zeta(4) + \frac{715}{2}\zeta(5)\,,$$

and $\zeta(n)$ is the Riemann Zeta function.

As $\Pi''(s)$ is renormalisation group invariant, we are free to make any convenient choice of the renormalisation scale. We use the 'contour improvement' prescription, whereby the logs in (4.18) are 're-summed' by making the choice $\mu^2 = Q^2$. This improves the convergence of the perturbative series by removing the dependence on large powers of possibly large logs which would appear in the (unknown) higher order terms. The contour improved perturbative contribution to our correlator is then,

$$\begin{aligned}\Pi_0''(Q^2) = \frac{6m_q^2(Q^2)}{2(4\pi)^2Q^2}\Bigg\{1 + \frac{11a_s(Q^2)}{3} + a_s^2(Q^2)\left(\frac{5071}{144} - \frac{35}{2}\zeta(3)\right) \\ + a_s^3(Q^2)\left(-\frac{4781}{9} + \frac{b_1}{6} + \frac{475}{4}\zeta(3)\right)\Bigg\}\,. \end{aligned} \tag{4.20}$$

The calculation of the running coupling and quark mass is explained in Section 4.7.

4.5.2 Dimension 2 Operators

Naïvely, the only gauge-invariant operator of dimension two that can be constructed within QCD is the so-called mass insertion term, m_q^2. For the light quarks that we are considering this term can safely be ignored.

Some recent works have suggested that there may be mechanisms outside of the normal OPE which could lead to dimension two contributions to correlation

functions. These mechanisms include renormalons (singularities of the correlator related to divergent perturbative series - see [77] for a recent review), and a tachyonic (*i.e.* imaginary) gluon mass [78]. It has been argued that, if they do exist, the effects of dimension two operators would not be significant in most sum rule analyses and that even in calculations where they would be expected to be most noticeable, these effects are consistent with zero [79]. Hence, in this work, we choose to ignore them.

4.5.3 Dimension 4 Operators

There are three types of dimension four operator that could contribute to the OPE for the scalar-isoscalar correlator. These are explicit mass corrections, m^4, which as in the dimension two case are ignored, the light quark condensate, $\langle m_q\bar{q}q\rangle$, and the gluon condensate, $\langle a_s G^a_{\mu\nu}G^{a\,\mu\nu}\rangle = \langle a_s G^2\rangle$ where $G^a_{\mu\nu}$ is the gluon field-strength tensor. To two loop order, the contribution to the correlator from the quark condensate can be found in [73] and from the gluon condensate contribution is taken from [80, 72]. The overall expression is

$$\Pi_4(Q^2) = \frac{m_q^2}{2Q^2}\left\{3\langle m_q\bar{q}q\rangle\left[1+a_s\left(\frac{13}{3}-2\log\frac{Q^2}{\mu^2}\right)\right] + \frac{\langle a_s G^2\rangle}{8}\left[1+a_s\left(\frac{67}{18}-2\log\frac{Q^2}{\mu^2}\right)\right]\right\}, \tag{4.21}$$

and taking two derivatives gives

$$\Pi_4''(Q^2) = \frac{m_q^2}{2Q^6}\left\{6\langle m_q\bar{q}q\rangle\left[1+a_s\left(\frac{22}{3}-2\log\frac{Q^2}{\mu^2}\right)\right] + \frac{\langle a_s G^2\rangle}{4}\left[1+a_s\left(\frac{121}{18}-2\log\frac{Q^2}{\mu^2}\right)\right]\right\}. \tag{4.22}$$

Applying the contour improvement prescription we obtain

$$\Pi_4''(Q^2) = \frac{m_q^2(Q^2)}{2Q^6}\left\{6\langle m_q\bar{q}q\rangle\left[1+\frac{22a_s(Q^2)}{3}\right] + \frac{\langle a_s G^2\rangle}{4}\left[1+\frac{121a_s(Q^2)}{18}\right]\right\}. \tag{4.23}$$

As mentioned above, correctly separating the short and long distance physics in the OPE leads to mixing under renormalisation of operators of a given dimensionality. Up to to negligible $\mathcal{O}(m_q^4)$ terms, the light quark condensate remains

RG-invariant [73]. However, the gluon condensate mixes with the strange quark condensate, $\langle m_s\bar{s}s\rangle$, and the explicit strange quark mass correction [72]. In terms of the two-loop RG-invariant combinations introduced in [76], (4.23) becomes

$$\Pi_4''(Q^2) = \frac{m_q^2(Q^2)}{2Q^6}\left\{6\langle m_q\bar{q}q\rangle\left[1+\frac{22a_s(Q^2)}{3}\right] - \frac{I_g}{9}\left[1+\frac{121a_s(Q^2)}{18}\right] + I_s\frac{4a_s(Q^2)}{9} - \frac{3m_s^4(Q^2)}{28\pi^2}\right\}, \tag{4.24}$$

where

$$I_G = -\frac{9\langle a_sG^2\rangle}{4}\left(1+\frac{16a_s}{9}\right)+4a_s\langle m_s\bar{s}s\rangle\left(1+\frac{91a_s}{24}\right)+\frac{3m_s^4}{4\pi^2}\left(1+\frac{4a_s}{3}\right), \tag{4.25}$$

and

$$I_s = \langle m_s\bar{s}s\rangle + \frac{3m_s^4}{7\pi^2}\left(\frac{1}{a_s}-\frac{53}{24}\right). \tag{4.26}$$

The value of the light quark condensate is fixed (at lowest order in χPT) by the Gell-Mann-Oakes-Renner [81] formula

$$\langle m_q\bar{q}q\rangle = -\frac{m_\pi^2 f_\pi^2}{4}, \tag{4.27}$$

where $f_\pi = 131$ MeV is the pion decay constant. The value of the gluon condensate at 1 GeV is taken to be $(381\text{ MeV})^4$ and the input values for the strange quark mass and condensate, which should not affect our final results, are $m_s(1\text{ GeV}^2) = 159$ MeV and $\langle m_s\bar{s}s\rangle = -(195\text{ MeV})^4$. Deviations from these standard values will be discussed in Chapter 5.

4.5.4 Dimension 6 Operators

At dimension six, the most important contributions to the scalar-isoscalar correlator can be taken from [73]. In this approximation we have three terms, coming from two four quark operators and the 'mixed' operator. The full renormalisation group properties of these operators have not yet been explored, so we follow [73] and take the dimension six contribution at a fixed scale of 1 GeV, thus all references to condensates, the strong coupling constant and the quark mass in this

section imply their values at this scale. The dimension six contribution to the correlator is

$$\Pi_6(Q^2) = \frac{m_q^2}{2Q^4}\left(m_q\langle g\bar{q}\sigma_{\mu\nu}G^{\mu\nu a}\lambda^a q\rangle + \pi^2 a_s\left[\langle\bar{q}\sigma_{\mu\nu}\lambda^a q\bar{q}\sigma^{\mu\nu}\lambda^a q\rangle + \frac{2}{3}\langle\bar{q}\gamma_\mu\lambda^a q\bar{q}\gamma^\mu\lambda^a q\rangle\right]\right) , \quad (4.28)$$

where γ_μ are the Dirac matrices, $\sigma_{\mu\nu} = \frac{1}{2}\{\gamma_\mu, \gamma_\nu\}$ and λ^a are the usual Gell-Mann matrices normalised such that $\mathrm{Tr}[\lambda^a\lambda^b] = 2\delta^{ab}$. We follow standard practice in sum rule work and relate the values of the dimension six condensates to the dimension three (RG-variant) two quark condensate $\langle\bar{q}q\rangle$.

For the mixed condensate this is done by parameterising it as

$$\langle g\bar{q}\sigma_{\mu\nu}G^{\mu\nu a}\lambda^a q\rangle = m_0^2\langle\bar{q}q\rangle . \quad (4.29)$$

The constant m_0^2 can then be found from a sum rule analysis of a channel where this operator is dominant. This analysis has been carried out in [82], where the value $m_0^2 = 0.8 \pm 0.2$ GeV^2 was found. However, earlier determinations of this constant [83] gave markedly different values, in the range $m_0^2 = 0.2 - 1.1$ GeV^2.

For the four quark operators there exists no reliable calculation of their VEVs. If we invoke the so-called vacuum saturation hypothesis [57] we obtain the approximations

$$\langle\bar{q}\sigma_{\mu\nu}\lambda^a q\bar{q}\sigma^{\mu\nu}\lambda^a q\rangle = -\frac{16}{3}\langle\bar{q}q\rangle^2 , \quad (4.30)$$

$$\langle\bar{q}\gamma_\mu\lambda^a q\bar{q}\gamma^\mu\lambda^a q\rangle = -\frac{16}{9}\langle\bar{q}q\rangle^2 . \quad (4.31)$$

However, it has been suggested that the vacuum saturation hypothesis is quite strongly violated in nature [84]. To take this into account we introduce the multiplicative factor V_{vs}.

Putting all this together gives

$$\Pi_6(Q^2) = \frac{m_q^2}{2Q^4}\left(m_q\, m_0^2\langle\bar{q}q\rangle - \frac{176\pi^2 a_s V_{vs}}{27}\langle\bar{q}q\rangle^2\right) , \quad (4.32)$$

Noting that, for the mixed condensate term, the RG-variant two quark condensate appears with the quark mass to give the RG-invariant combination $\langle m_q\bar{q}q\rangle$ and

taking two derivatives with respect to Q^2 gives

$$\Pi_6''(Q^2) = \frac{6m_q^2}{2Q^8}\left(m_0^2\langle m_q\bar{q}q\rangle - \frac{176\pi^2 a_s V_{vs}}{27}\langle\bar{q}q\rangle^2\right) . \tag{4.33}$$

As input, we take the standard value $\langle\bar{q}q\rangle = -(0.225\text{ GeV})^3$. The effect that varying m_0^2 and V_{vs} has on our final results will be discussed in Chapter 5.

4.6 Instantons

The OPEs for the scalar-isoscalar and scalar-isovector channels are identical. This was originally interpreted as an explanation for the almost exact mass degeneracy of the $f_0(980)$ and the $a_0(980)$ [60]. However, we know that the OPE is not enough to completely describe the QCD vacuum and that other effects are important, particularly in the scalar and pseudoscalar channels [85].

Instantons [86] are solutions of the classical solutions of the Euclidean version of a quantum field theory. They are localised in both space and time and can give a non-zero contribution to the correlation functions of that theory. Within the framework of QCD Laplace sum rules, instantons have been shown to give an important contribution to scalar and pseudoscalar correlators [87, 88, 63].

The complex nature of the QCD vacuum means that it is not currently possible to directly solve the equations of motion of the full theory. We must make use of approximations. In this work we choose to work in an approximation known as the Instanton Liquid Model [89, 90, 87]. Here the QCD vacuum is modelled as a four-dimensional 'liquid' of instantons, which is assumed to be dilute enough to make the idea of individual instantons meaningful. The liquid is characterised by the average instanton size ρ_c and four-volume density n_c (or alternatively the average instanton separation, $r_c = n_c^{-1/4}$). The Instanton Liquid model is then thought to be a good approximation if the ratio ρ_c/r_c is small.

In [90], the average instanton size was estimated to be about $(600\text{ MeV})^{-1}$, or approximately 1/3 fm, and the average separation $(200\text{ MeV}^{-1}) \approx 1$ fm (or $n_c \approx 1\text{ fm}^{-4}$). These are now often taken as standard values. Lattice studies

would seem to be consistent with this value of ρ_c, but may favour a slightly larger value, and tend to find higher instanton densities (see Table 1 of [91]). There have also been recent suggestions [92] that the lattice determination of the instanton size may not be reliable as conventional lattice 'instanton finder' algorithms may miss larger instantons.

Within the Instanton Liquid Model the instanton contribution to the scalar-isoscalar light-quark correlator was found in [87, 93] to be

$$\Pi_i(s) = \frac{3\,Q^2\,m_q^2}{2\pi^2}\left[K_1(\rho_c\sqrt{Q^2})\right]^2 , \tag{4.34}$$

where $K_1(x)$ is a modified Bessel function of the second kind (or MacDonald function). Taking two derivatives we obtain

$$\Pi_i''(s) = \frac{3\,\rho_c^2\,m_q^2}{4\pi^2}\left[K_0^2(\rho_c\sqrt{Q^2}) + K_1^2(\rho_c\sqrt{Q^2})\right] . \tag{4.35}$$

As stated above $\Pi''(s)$ is an RG-invariant quantity. The only quantity in (4.35) that could have a renormalisation scale dependence is the quark mass. This renormalisation scale dependence can not be cancelled out anywhere else, so we conclude that the quark mass appearing in (4.35) must be the quark mass at some fixed scale, X. *A priori* we do not know what this scale is. It is reasonable to expect that this scale is related to the instanton scale given by $1/\rho_c$ or the hadronic scale of $\sim$ 1 GeV, but we have no physical reason for choosing $1/\rho_c$ rather than *e.g.* $2/\rho_c$. Thus we take this scale as an input parameter in the calculation. If this scale is found to be considerably different from the hadronic and instanton scales then it would call into doubt our treatment of the instanton contribution.

4.7 The Running Coupling and Quark Mass

The running of the coupling constant, α_s and quark mass, m_q, are defined by the Renormalisation Group Equations

$$\mu^2\frac{\mathrm{d}a_s}{\mathrm{d}\mu^2} = -\beta(a_s) , \qquad \beta(a_s) = a_s^2\sum_{i\geq 0}\beta_i a_s^i , \tag{4.36}$$

and

$$\mu^2 \frac{\mathrm{d}m_q}{\mathrm{d}\mu^2} = -m_q \gamma(a_s) \ , \qquad \gamma(a_s) = a_s \sum_{i \geq 0} \gamma_i a_s^i \ , \tag{4.37}$$

where $a_s = \alpha_s/\pi$.

Currently, the QCD β and γ functions are known to four-loop order. For three active flavours, the coefficients of the β function within the $\overline{\mathrm{MS}}$ scheme are [94]

$$\beta_0 = \frac{9}{4} \ , \quad \beta_1 = 4 \ , \quad \beta_2 = \frac{3863}{384} \ , \quad \beta_3 = \frac{140\,599}{4608} + \frac{445}{32}\zeta(3) \ . \tag{4.38}$$

The coefficients of the γ function, also within the $\overline{\mathrm{MS}}$ scheme, are [95, 96]

$$\gamma_0 = 1 \ , \quad \gamma_1 = \frac{91}{24} \quad , \gamma_2 = \frac{8885}{576} - \frac{5}{2}\zeta(3) \ ,$$

$$\gamma_3 = \frac{2\,977\,517}{41\,472} - \frac{9295}{432}\zeta(3) + \frac{135}{16}\zeta(4) - \frac{125}{12}\zeta(5) \ . \tag{4.40}$$

The values of the coupling and the quark mass are then found by solving (4.36) and (4.37) with the four-loop β and γ functions defined by (4.38) and (4.40). *I.e.* we use the exact solution of the truncated RGE and not a truncated expansion in $\log(\mu^2/\Lambda_{QCD}^2)$ of this solution.

For the coupling, we choose to solve the implicit equation

$$\int_{a_s(m_\tau^2)}^{a_s(\mu^2)} \frac{\mathrm{d}a'}{\beta(a')} - \log\left(\frac{\mu^2}{m_\tau^2}\right) = 0 \ , \tag{4.41}$$

iteratively using Newton's method. As input, we take the experimental value $\alpha_s(m_\tau^2) = 0.334 \pm 0.022$, as measured by the ALEPH collaboration [97]. For reference, had we used the standard expansion for α_s, then at four-loops and with three active flavours this central input value would correspond to $\Lambda_{QCD} \approx 365$ MeV. For high values of $\alpha_s(m_\tau^2)$, or correspondingly Λ_{QCD}, the radiative corrections to (4.20) become more important and start to swamp the higher dimension terms, *i.e* it becomes more important to include higher loop corrections to the perturbative contribution than to include the condensates. It has been argued [98] that the sum rule methodology could become invalid for $\Lambda_{QCD} \gtrsim 330$ MeV. This is especially problematic for attempts to determine condensate values via the sum rule technique. As this is not our aim and considering the success of previous

sum rule works with similar and higher values of $\alpha_s(m_\tau^2)$ (Λ_{QCD}), we feel justified in applying sum rules to this problem.

For the quark mass, (4.37) is solved by

$$m_q(\mu^2) = m_q(1\,\mathrm{GeV}^2)\exp\left[\int_{a_s(1\,\mathrm{GeV}^2)}^{a_s(\mu^2)} \frac{\gamma(a')}{\beta(a')}\,\mathrm{d}a'\right] \tag{4.42}$$

Although the instanton and OPE contributions have factors of m_q^2 at different scales, writing the quark mass in this way gives an overall multiplicative factor of $m_q^2(1\,\mathrm{GeV}^2)$ on the QCD side. We define $[S_k(\mu^2, s_0)]_{calc}$ via

$$\left[S_k(M^2, s_0)\right]_{QCD} = m_q^2(1\,\mathrm{GeV}^2)\left[S_k(M^2, s_0)\right]_{calc}\ , \tag{4.43}$$

and it is this quantity that is actually calculated.

4.8 The Phenomenology Side

4.8.1 The Coupling Schemes

At low energies the only hadronic process possible in the scalar-isoscalar channel is $\pi\pi$ scattering. As pions are made of non-strange quarks it is reasonable to expect that, in the elastic region, the spectral density for the correlator is related to the absorptive part of the $\pi\pi \to \pi\pi$ scattering amplitude, $\mathcal{T}(s)$. This link can be made via the scalar form-factor of the pion, $d(s)$, which is defined by

$$d(s) = \langle 0|m_q\bar{q}q|\pi\pi\rangle\ . \tag{4.44}$$

Inserting a complete set of hadronic states into the correlator (4.3) and keeping only the lowest state, *i.e.* the two pion state, gives the spectral density in the elastic region,

$$\frac{\mathrm{Im}\Pi(s)}{\pi} = \frac{3\beta(s)}{32\pi^2}|d(s)|^2\ , \tag{4.45}$$

where $\beta(s) = \sqrt{1 - 4m_\pi^2/s}$.

Watson's Final State Interaction Theorem [99] implies that the form factor and the scattering amplitude have the same phase. Thus, in the region where

elastic unitarity holds, we can write

$$\mathcal{T}(s) = \alpha(s)d(s) \ , \tag{4.46}$$

where the coupling function, $\alpha(s)$, is real for real $s > 4m_\pi^2$. Substituting (4.46) into (4.45) and making use of the elastic unitarity relationship $\mathrm{Im}\mathcal{T} = \beta\,|\mathcal{T}|^2$ we obtain

$$\frac{\mathrm{Im}\Pi(s)}{\pi} = \frac{3}{32\pi^2}\frac{\mathrm{Im}\mathcal{T}}{\alpha^2(s)} \tag{4.47}$$

It is well known that $\pi\pi$ scattering contains an Adler zero [100], and that this Adler zero does not appear in the pion form factor. We now make the simplifying assumption that this is the only s-dependence appearing in $\alpha(s)$, *i.e.*

$$\alpha(s) = \alpha(s - s_A) \tag{4.48}$$

where s_A is the position of the Adler zero. Substituting (4.48) into (4.47) gives our first ansatz

$$\frac{\mathrm{Im}\Pi(s)}{\pi} = \frac{f\,\mathrm{Im}\mathcal{T}(s)}{(s - s_A)^2} \ , \tag{4.49}$$

where f is an unknown constant of proportionality.

Although the 4π threshold is at 560 MeV, it is well known that multi-pion channels are not significant below around 1400 MeV when quasi two-body channels, *e.g.* $\sigma\sigma$, $\rho\rho$, become important [101, 102]. The first significant inelastic channel is $\pi\pi \to K\overline{K}$. Even after this has opened the $\pi\pi$ final state will continue to pick out the non-strange contribution to the sum over states. Thus we might expect (4.49) to give a reasonable approximation to the true spectral density even above 1 GeV. We call this Coupling Scheme I.

The multi-pion final states mentioned above will increase the $n\overline{n}$ spectral density, causing (4.49) to be an underestimate at higher energies. Phenomenologically, we might expect the true spectral density to be enhanced by the ratio of the total to elastic $\pi\pi$ cross-sections, thus giving

$$\frac{\mathrm{Im}\Pi(s)}{\pi} = \frac{f\,(\mathrm{Im}\mathcal{T}(s))^2}{\beta(s)(s - s_A)^2|\mathcal{T}(s)|^2} \ , \tag{4.50}$$

which we call Coupling Scheme II. In the elastic region, the two coupling schemes are, of course, identical. Above the $K\overline{K}$ threshold, whereas Coupling Scheme I ignores all inelastic channels and so will underestimate the spectral density, Coupling Scheme II takes into account all inelastic channels, including those with hidden strangeness, and so may be an overestimate.

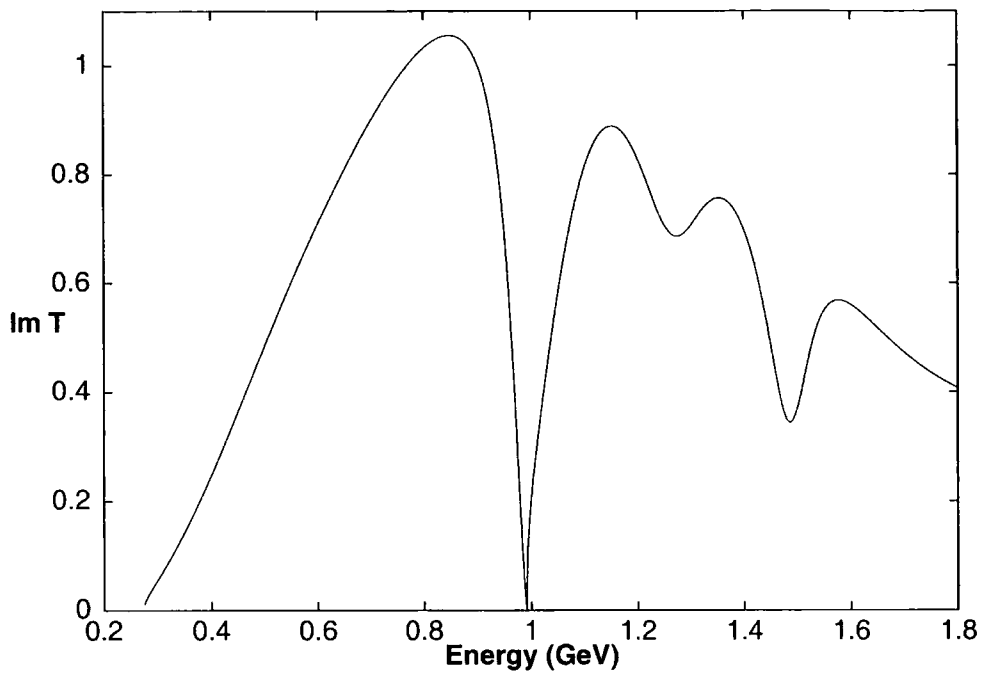

Figure 4.2: A sketch showing the absorptive part of the $I = J = 0$ $\pi\pi$ scattering amplitude, based on the Bugg analysis [103]

Figure 4.2 shows a sketch of the absorptive part of the isospin zero, S-wave amplitude for $\pi\pi$ scattering. From this we can clearly see that the $f_0(400-1200)$ and the $f_0(1370)$ appear as peaks, while the $f_0(980)$ and the $f_0(1500)$ show up as sharp dips. Thus these latter two states, and in particular the $f_0(980)$, will be largely decoupled from the spectral density and if saturation of the sum rules is achieved with either of our two Coupling Schemes, it will not be due in any great part to the $f_0(980)$ or $f_0(1500)$. By varying M^2 and s_0 it may be possible to determine which of the $f_0(400-1200)$ and the $f_0(1370)$ plays the dominant role in saturation, but for the evaluation of the Wilson coefficients in the OPE to be trustworthy, we would expect s_0 to be too high to exclude the $f_0(1370)$.

Nevertheless, as the decaying exponential in the weight functions of our sum rules suppresses the integrand for $s > M^2$, it may still be possible to determine which resonance is most important for saturation.

4.8.2 Experimental Inputs

The $\pi\pi$ scattering amplitude is calculated from the experimentally measured inelasticities, η, and phase-shifts, δ, in text-book fashion

$$\mathcal{T}(s) = \frac{\eta e^{2i\delta} - 1}{2i\beta(s)} \,. \tag{4.51}$$

We will consider two different data-sets. The first is a smooth curve based on the parameterisation due to Bugg [103]. This data-set is available up to a maximum energy of 2.25 GeV, but contains no experimental errors. This data-set is illustrated in Figure 4.3, from which we see that this parameterisation is in good agreement with earlier, low-energy data. The second data-set is based upon the *down-flat* solution of Kamiński *et al.* from their recent reanalysis [104] of the combined data from the polarised and unpolarised target CERN(-Cracow)-Munich experiments [105, 106]. This data-set includes experimental errors, which are quite large due to the uncertainty in extracting the one-pion exchange signal, and is available in the energy range 600-1600 MeV. This down-flat solution is quite close to the earlier Ochs-Wagner analysis [107] and below 600 MeV we include the Roy equation extrapolation down to threshold of the Ochs-Wagner data carried out by Pennington and used in his discussion of $\gamma\gamma \to \pi\pi$ [108]. As we expect that $s_0 > (1.6 \text{ GeV})^2$ we also include some higher energy data from the Bugg parameterisation. This, somewhat composite, data-set is illustrated in Figure 4.4. In both data-sets we impose elastic unitarity up to the $K\bar{K}$ threshold. As we can see from Figure 4.3, the two data-sets are not too dissimilar and so we will only give results based on the Kamiński data-set where they differ from those for the Bugg parameterisation.

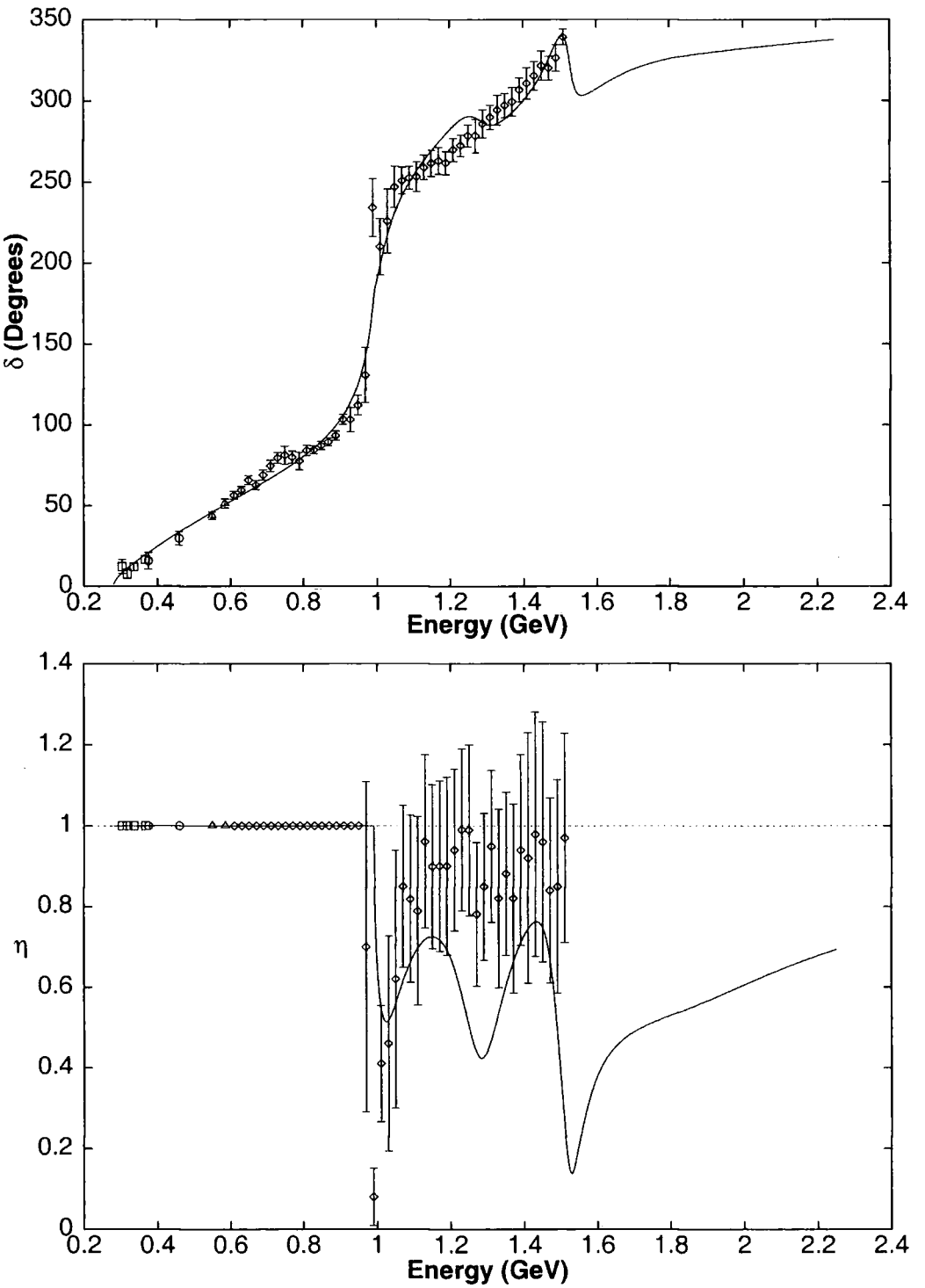

Figure 4.3: The Bugg parameterisation[103] of the scalar-isoscalar phase shifts, δ, and inelasticities, η. Note that we have imposed elastic unitarity exactly up to the $K\overline{K}$ threshold. Superimposed are data points from K_{e4} data of Rosselet *et al.* [109] (squares), Alekseeva *et al.* [110] (circles), Estabrookes and Martin [111] and the Ochs-Wagner analysis [107] of the CERN-Munich unpolarised experiment [105] (diamonds).

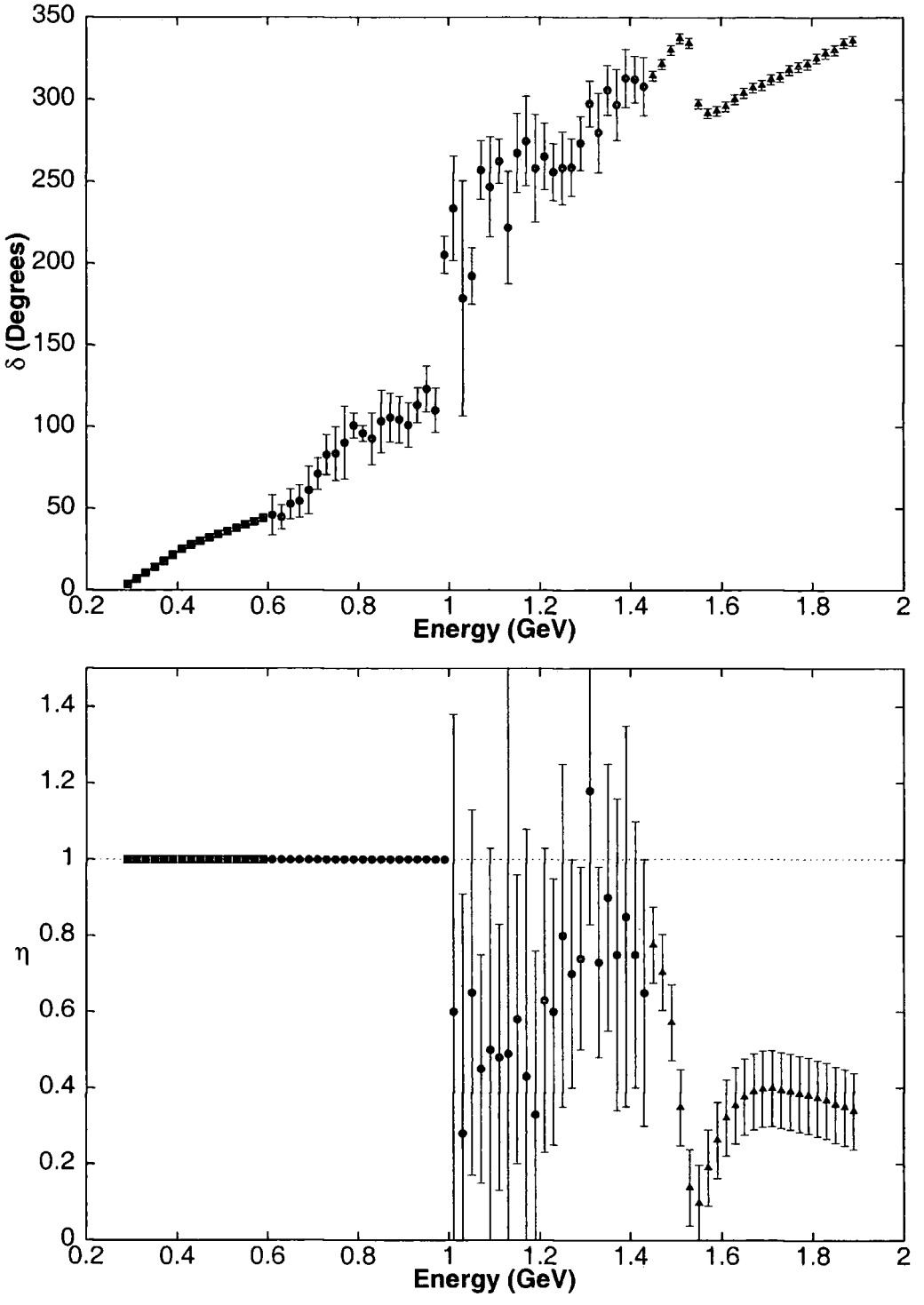

Figure 4.4: The phase shifts, δ, and inelasticities, η, of the Kamiński data-set based on their *down-flat* solution [104] (circles). These data are supplemented by the Pennington extrapolation to threshold [108] (squares) and the Bugg parameterisation [103]. Note that we have imposed elastic unitarity exactly up to the $K\overline{K}$ threshold.

4.8.3 Normalisation

Some justification for the above Coupling Schemes (4.49) and (4.50), and a value for the normalisation factor f, can be obtained by making a comparison with the spectral density obtained using an Omnès representation [112] of the form factor. This representation is given by

$$d(s) = d(0) \exp\left[\frac{s}{\pi}\int_{4m_\pi^2}^{\infty} \frac{\phi(s')\,\mathrm{d}s'}{s'(s'-s)}\right] , \tag{4.52}$$

where $\phi(s)$ is the phase of $I = J = 0$ $\pi\pi$ scattering. The form factor at zero momentum transfer, which normalises the Omnès function, can be determined from the Feynman-Hellman Theorem [113] and is given by

$$d(0) = m_q \frac{\partial m_\pi^2}{\partial m_q} . \tag{4.53}$$

To leading order in χPT, the physical pion mass is given by the GMOR formula (4.27) and thus we see that

$$d(0) = m_\pi^2 . \tag{4.54}$$

Going to next-to-leading order in χPT would introduce a correction to (4.54) of the order of 1% (see for example [114]), which is safe to neglect.

To evaluate the integral in (4.52) exactly requires knowledge of the scattering phase in the high energy region where it is unknown. However, the integrand is dominated by the region around s. So if we restrict our comparison to the low energy region then the behaviour of the phase above some point s_1, where $s_1 \gg s$, will not greatly effect the value of the integral. We take s_1 to correspond to the last data point and approximate the phase above this point as a constant, ϕ_1. Thus, the spectral density, as calculated from the Omnès representation, is written

$$\frac{\mathrm{Im}\Pi(s)}{\pi} = \frac{3m_\pi^4}{32\pi^2}\beta(s)\left(\frac{s_1}{s_1 - s}\right)^{2\phi_1/\pi} \exp\left[\frac{2s}{\pi}\int_{4m_\pi^2}^{s_1} \frac{\phi(s')\mathrm{d}s'}{s'(s'-s)}\right] . \tag{4.55}$$

where the bar on the integral sign denotes the Cauchy Principal Value.

The value of the constant, f, can then be determined by fitting (4.49) to (4.55), this fit is carried out up to a maximum energy of 400 MeV (over this energy range

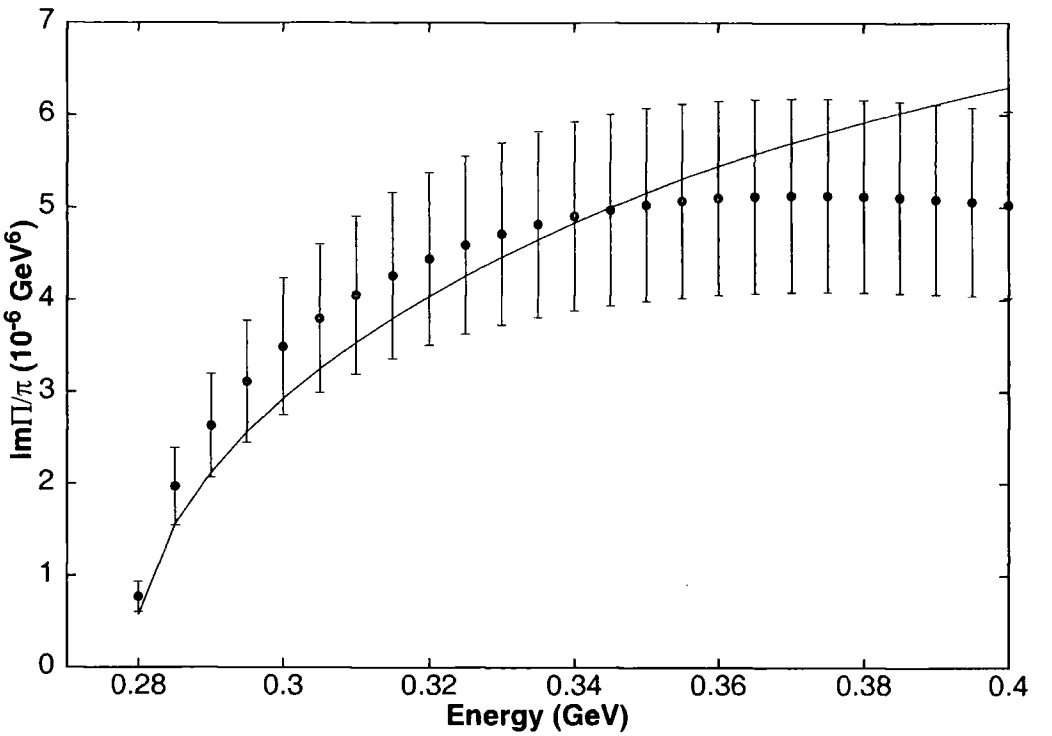

Figure 4.5: The spectral density below 400 MeV, as calculated from our Coupling Scheme (points) and from the single channel Omnès representation (solid line) for the Bugg data-set. The errors come from assuming a 5% error on the phase-shift with the inelasticity exactly equal to 1.

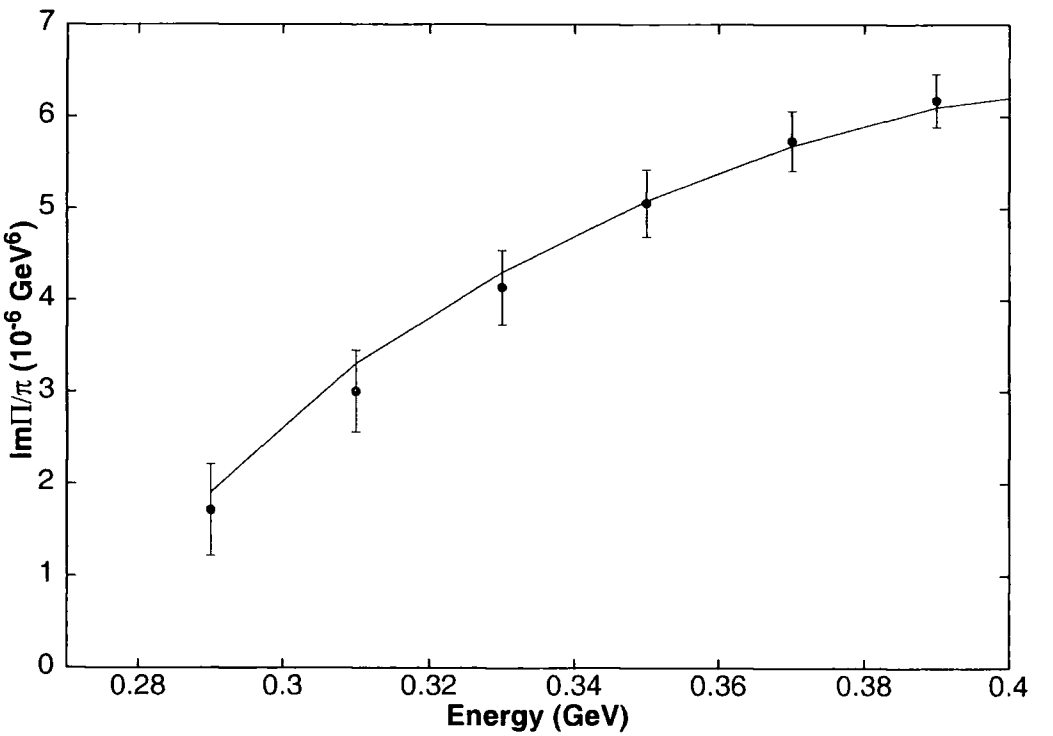

Figure 4.6: The spectral density below 400 MeV, as calculated from our Coupling Scheme (points) and from the single channel Omnès representation (solid line) for the Kamiński data-set.

it does not matter which Coupling Scheme we use). The position of the Adler zero for isospin-0, S-wave $\pi\pi$ scattering is fixed by lowest order χPT to be $\frac{1}{2}m_\pi^2$, and so we only have one parameter to fit for. The results of this fit are shown in Figures 4.5 and 4.6. The constant of proportionality was found to be $\sim 4.7 \times 10^{-7}$ for the Bugg parameterisation and $\sim 6.5 \times 10^{-7}$ for the Kamiński data-set, which can be seen to give a reasonable fit. However, these values are quite sensitive to the maximum energy of the fit and should not be trusted to an accuracy better than 20-30%.

With this normalisation our two Coupling Schemes are shown in Figure 4.7 for the Bugg data-set. We see that the differences between the two Coupling Schemes are actually quite small, thus, except where the difference is important, we will only show results from Scheme II. In Figure 4.8, we show how the spectral density obtained from the Bugg parameterisation compares with that implied by the data points shown in Figure 4.3, using Coupling Scheme II.

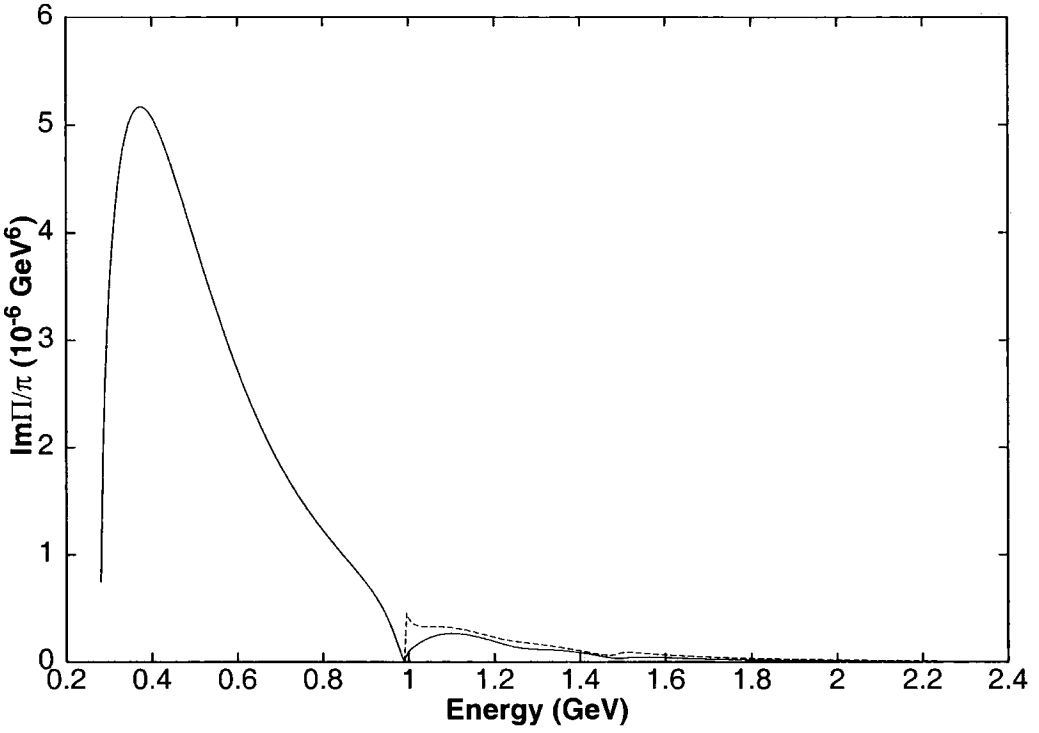

Figure 4.7: The two Coupling Schemes as calculated from the Bugg data-set. The solid line shows Coupling Scheme I and the dashed line shows Coupling Scheme II.

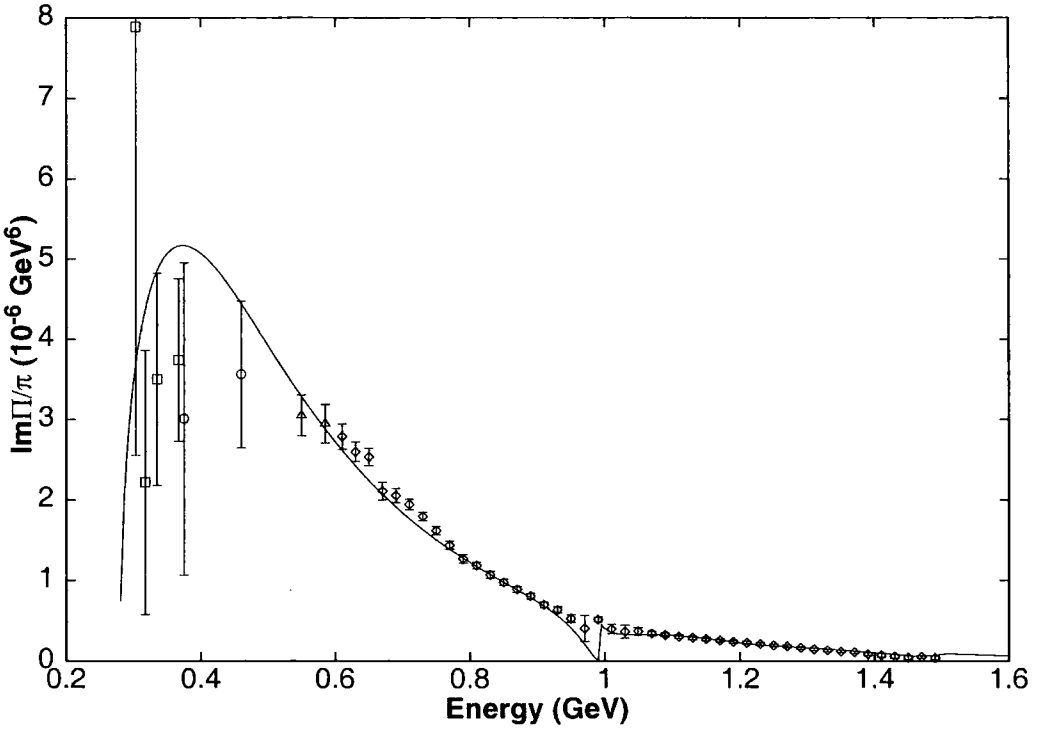

Figure 4.8: A comparison of the spectral densities obtained, using Coupling Scheme II, from the Bugg parameterisation and the experimental data. The labelling for the data points is the same as for Figure 4.3.

Chapter 5

Sum Rule Investigation of the Scalar Isoscalar Channel

5.1 The sizes of the different contributions.

In the preceding Chapter, expressions for the different contributions to the theoretical side of our sum rules have been give. These expressions contained many parameters which, for ease of reference we now list in Table 5.1 along with their 'standard' values. Unless otherwise stated, the results shown will use these parameter values. Using these standard values, in Figures 5.1 and 5.2 we show the size of the three theoretical contributions to the lowest R and T-type sum rules for two values of s_0.

The first thing that we notice from these graphs is that, for typical values of s_0, the dominant contribution to the theoretical side comes from the purely perturbative part. Next most important are the instantons, the contribution of which have a magnitude approximately 20-50% that of perturbation theory, with the condensate contribution being two orders of magnitude smaller. This shows that instanton effects are indeed important in understanding the scalar mesons. That they have quite such a large effect on the sum rules could cause some concern as the instanton contribution is the least well controlled of the three, being as it

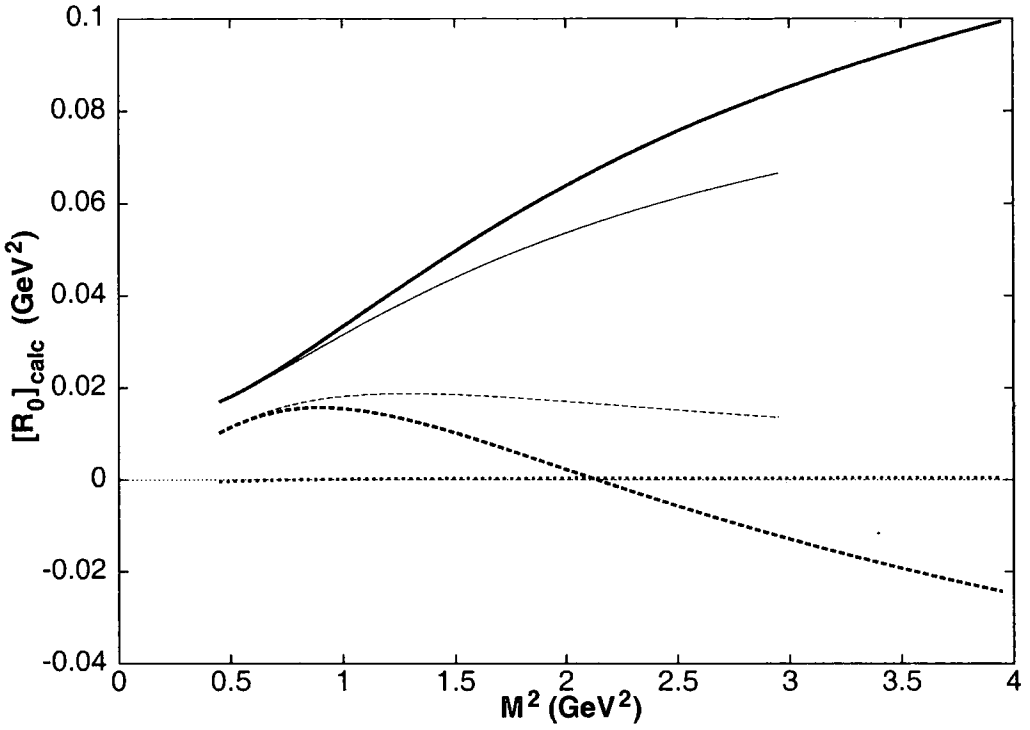

Figure 5.1: The purely perturbative (solid line), instanton (dashed line) and condensate (dotted line) contributions to the R-type sum rules. For the thinner lines $s_0 = 3.0$ GeV^2, and for the thicker lines $s_0 = 4.0$ GeV^2. The standard parameter values of Table 5.1 were used with $X = 1$ GeV^2.

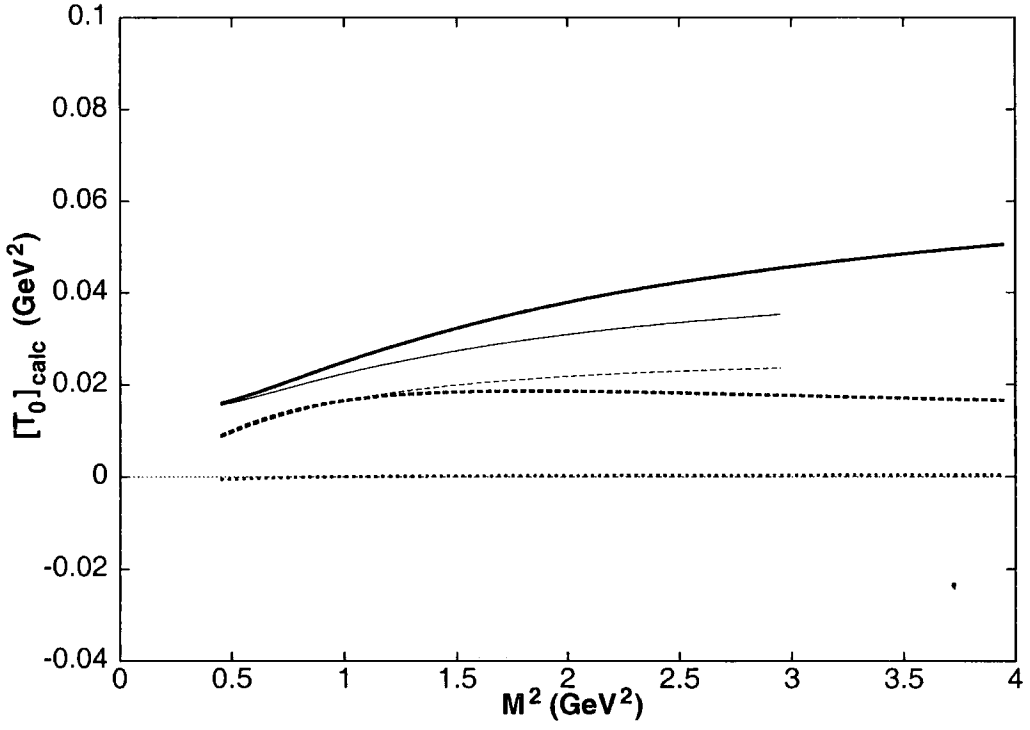

Figure 5.2: As Figure 5.1, but for the T-type sum rules.

Parameter		Value
$\alpha_s(m_\tau^2)$	Strong coupling constant	0.334
$\langle m_q\bar{q}q\rangle$	Invariant light-quark condensate	$-\frac{1}{4}m_\pi^2 f_\pi^2 \approx -(95\text{ MeV})^4$
$\langle a_s G^2\rangle$	Gluon condensate	$(381\text{ MeV})^4$
$\langle m_s\bar{s}s\rangle$	Strange-quark condensate at 1 GeV^2	$-(195\text{ MeV})^4$
m_s	Strange quark mass at 1 GeV^2	159 MeV
$\langle\bar{q}q\rangle$	Light-quark condensate at 1 GeV^2	$-(225\text{ MeV})^3$
m_0^2	Mixed condensate parameter	0.8 GeV^2
V_{vs}	Vacuum saturation violation	1
ρ_c	Average Instanton size	$(600\text{ MeV})^{-1}$
X	Instanton Quark Mass Scale	Unknown

Table 5.1: Standard values of all parameters used to evaluate the sum rules.

is based on a rough model.

Figures 5.1 and 5.2 also suggest that the T-type sum rules are more stable to changes in s_0, though in both cases the increase in the perturbative contribution as s_0 is increased is somewhat compensated by a decrease in the instanton contribution. We can also see that for larger s_0, the instanton contribution can change sign and become negative for some values of M^2. If the instanton contribution becomes too negative, it will make the whole sum rule negative. On the phenomenological side the sum rules must be positive (due to the positivity of ImΠ), this suggests that for certain values of s_0, $\alpha_s(m_\tau^2)$, X and ρ_c our sum rules may break down.

5.2 Measuring the Saturation

In any sum rule calculation, we hope to find regions of the parameter space where the theoretical and phenomenological sides are equal. We measure this *saturation* of the sum rules by introducing the double ratios

$$D_k^S(s_0, M^2) = \frac{[S_{k+1}/S_k]_{had}}{[S_{k+1}/S_k]_{QCD}} \,. \tag{5.1}$$

This ratio is independent of the overall normalising constants on either side, *i.e* f and $m_q^2(1\text{ GeV}^2)$, and obviously is equal to one when the sum rules are

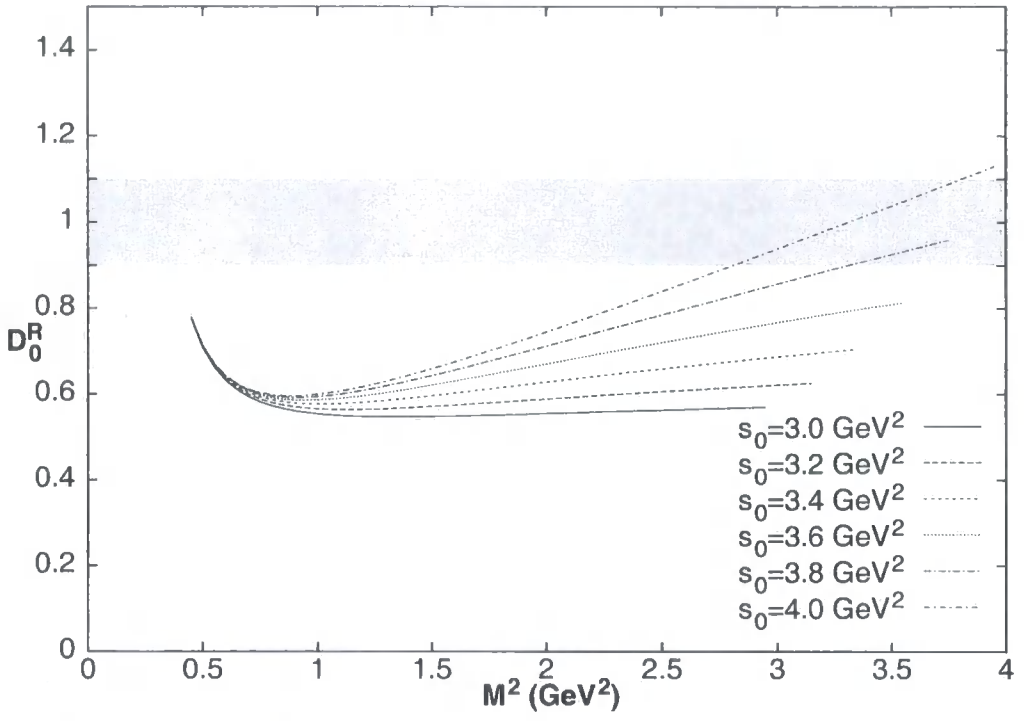

Figure 5.3: The stability curve for the R-type sum rules for various values of s_0 and the standard parameter values of Table 5.1. The shaded area shows the 10% agreement region.

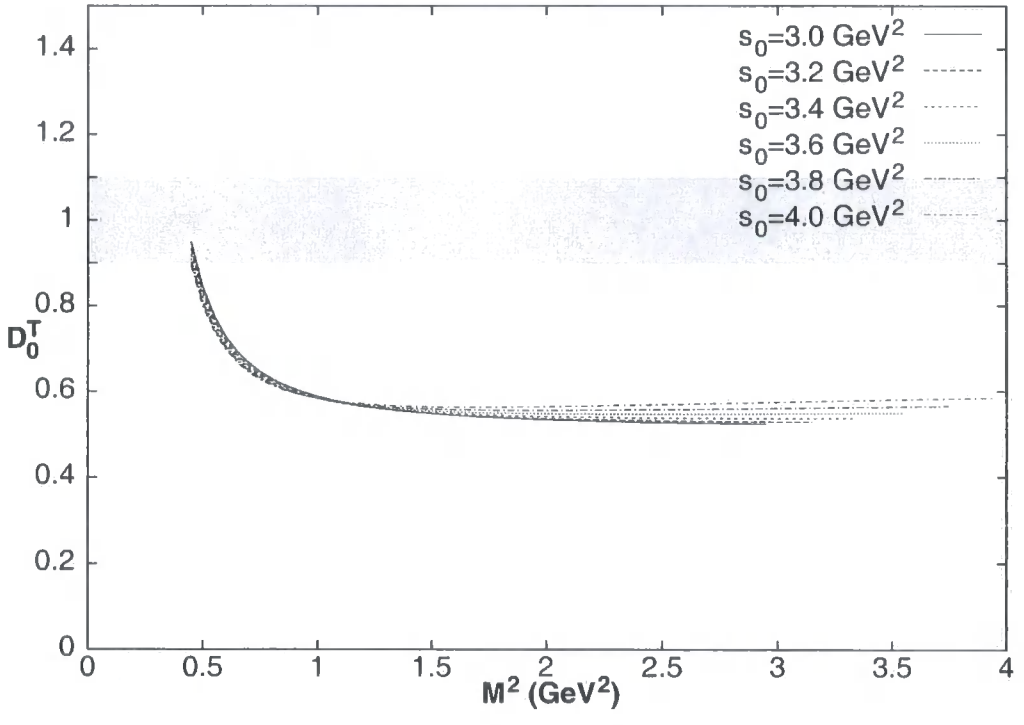

Figure 5.4: As Figure 5.3 but for the T-type sum rules.

saturated. As sum rule analyses are generally accurate to around 10-20% we set an agreement region of 1 ± 0.1. In practice we shall use only the lowest such double ratio for each type of sum rule, *i.e* D_0^S, as the integer powers of s in the higher sum rules increase the importance of the upper end of the integrand on the phenomenological side. Figures 5.3 and 5.4 show this double ratio for the R and T-type sum rules for the standard parameter values and various values of s_0 in the range expected to give the best saturation.

Another way to measure whether the sum rules are saturated is by making a prediction for a physical quantity. As M^2 is an unphysical parameter, for 'sensible' values of s_0 this prediction should be effectively independent of M^2 over a wide range. From (4.43), we see that the theoretical side of our sum rules contains an overall factor of $m_q^2(1\ \mathrm{GeV}^2)$, we can thus make an estimate for the average light quark mass from

$$m_q(1\ \mathrm{GeV}^2) = \sqrt{\frac{[S_k]_{had}}{[S_k]_{calc}}}\ . \tag{5.2}$$

If the graph of this quantity against M^2 is found to be flat then we can say that the sum rules are saturated. Although the actual value of the quark mass extracted will depend on the constant f, its M^2 dependence will not, thus as a test of saturation (5.2) is independent of any uncertainties in the normalisation of the hadronic side. Once again we will use only the lowest sum rules, *i.e.* S_0, to estimate the quark mass. For the standard parameter values, the quark mass curves obtained with various s_0 are shown in Figure 5.5, for the R-type, and Figure 5.6, for the T-type.

The first point to notice from Figures 5.3 - 5.6 is that with the standard parameters and X taken arbitrarily to be 1 GeV^2 the sum rules are *not* saturated. All four of these Figures make use of Coupling Scheme II, however using Coupling Scheme I would not change this conclusion. In fact, for Coupling Scheme I the saturation is slightly worse. That saturation is not achieved is not such a great surprise. The scale X is a completely unknown quantity. Whilst we may intuitively expect that it must be near the typical hadronic scale of around 1 GeV^2,

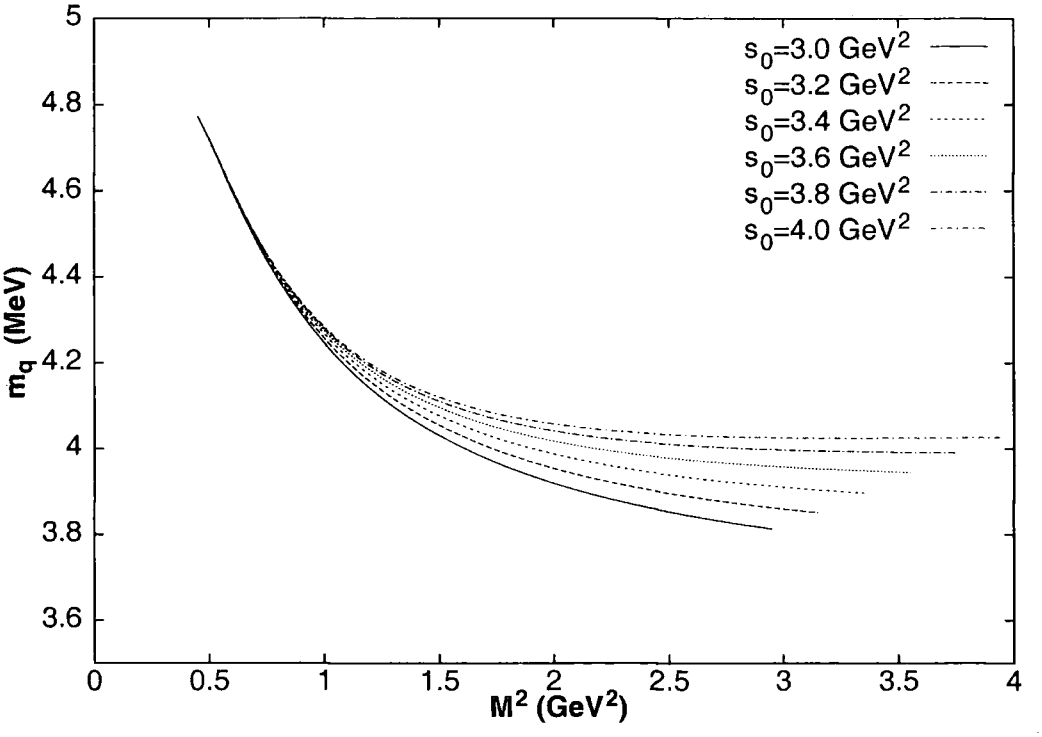

Figure 5.5: $m_q(1\ \mathrm{GeV}^2)$ calculated from the R-type sum rules for various values of s_0 and the standard parameter values of Table 5.1, with X taken as 1 GeV^2.

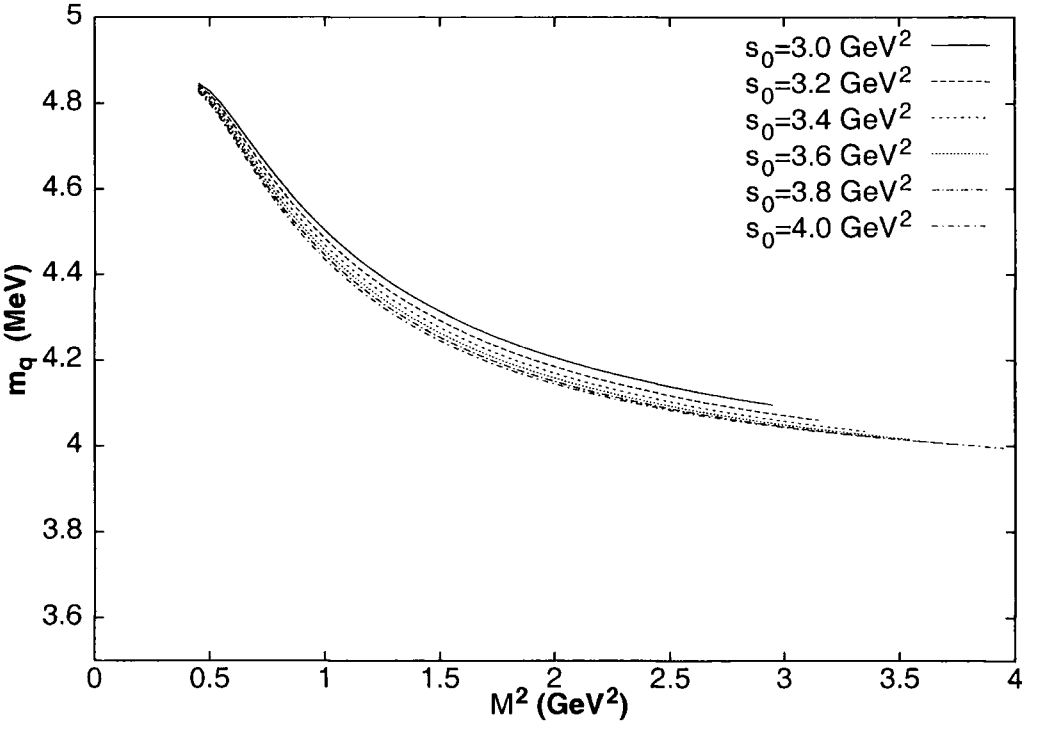

Figure 5.6: As Figure 5.5 but for the T-type sum rules.

we do not know *a priori* its exact value nor how sensitive the sum rules will be to it. 1 GeV^2 was just a guess, and we would have been very lucky indeed if our first guess had turned out to be correct. Thus in Section 5.3.1 we will attempt to determine this scale and we shall see that it has quite a strong effect on the quality of the saturation. The second conclusion to be drawn from Figures 5.3 - 5.6 is the the T-type sum rules are indeed less sensitive to the choice of s_0. From now on we will in general show results based on these sum rules.

5.3 The Instanton Parameters

5.3.1 The Scale of the Quark Mass

As mentioned before, the instanton contribution includes the average quark mass at a fixed, but unknown, scale, X. To evaluate (4.35), we introduce a new parameter, λ, which is equal to the ratio of $m_q^2(X)$ to $m_q^2(1\ \mathrm{GeV}^2)$, *i.e.*,

$$\lambda = \left[\frac{m_q(X)}{m_q(1\ \mathrm{GeV}^2)}\right]^2 = \exp\left[2\int_{a_s(1\ \mathrm{GeV}^2)}^{a_s(X)} \frac{\gamma(a')}{\beta(a')}\,\mathrm{d}a'\right] , \tag{5.3}$$

where the second equality follows from (4.42). The instanton contribution is then

$$\dot{\Pi_i''}(s) = m_q^2(1\ \mathrm{GeV}^2)\,\lambda\,F(\rho_c, Q^2) , \tag{5.4}$$

where $F(\rho_c, Q^2)$ stands for the combination of Bessel functions in (4.35). Obviously then, λ just serves to rescale the the instanton contribution. Note that a value of $\lambda > 1$ implies that the scale $X < 1$ GeV^2.

In Figure 5.7 we show how the saturation of the sum rules, using the Bugg parameterisation and Coupling Scheme II, varies with λ. As shown above, (see Figure 5.4) the saturation curve for the T-type sum rules does not have a strong dependence on s_0 in the region 3.0 GeV$^2 \leq s_0 \leq$ 4.0 GeV^2 and henceforth, unless otherwise stated, we use the value $s_0 = 3.7$ GeV^2. No significance should be attached to this value. On the other hand, we have found that it is, in fact, not possible to saturate the sum rules without tuning both instanton parameters and

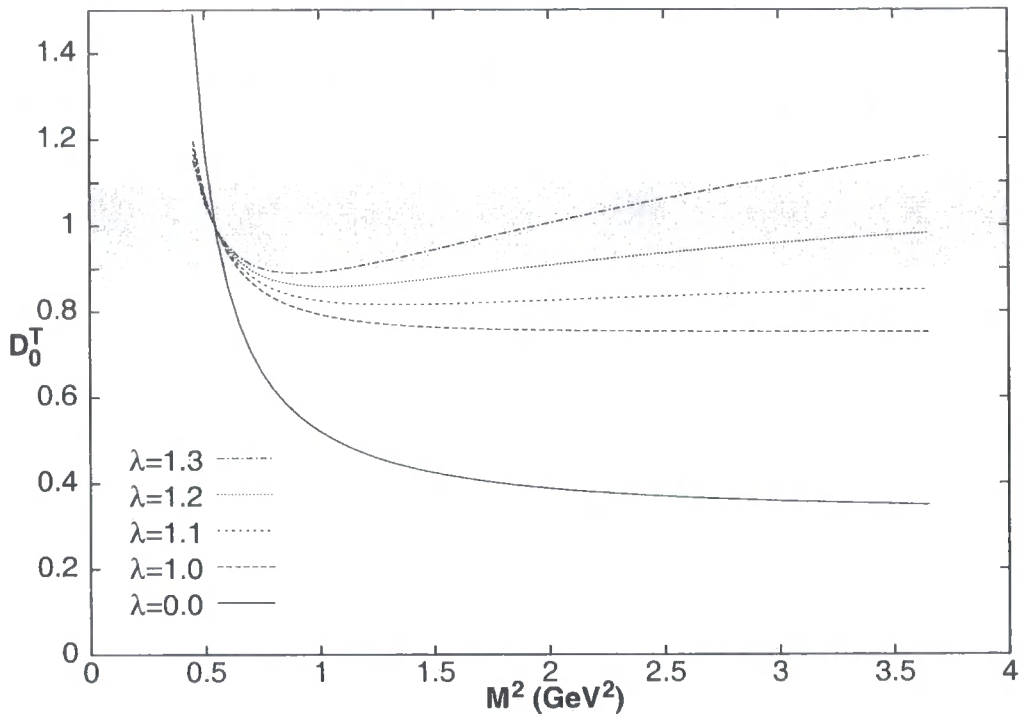

Figure 5.7: The effect of the instanton parameter λ on the the saturation curve for the lowest T-type sum rules. The values $s_0 = 3.7$ GeV^2 and $\rho_c = (500 \text{ MeV})^{-1}$ were used.

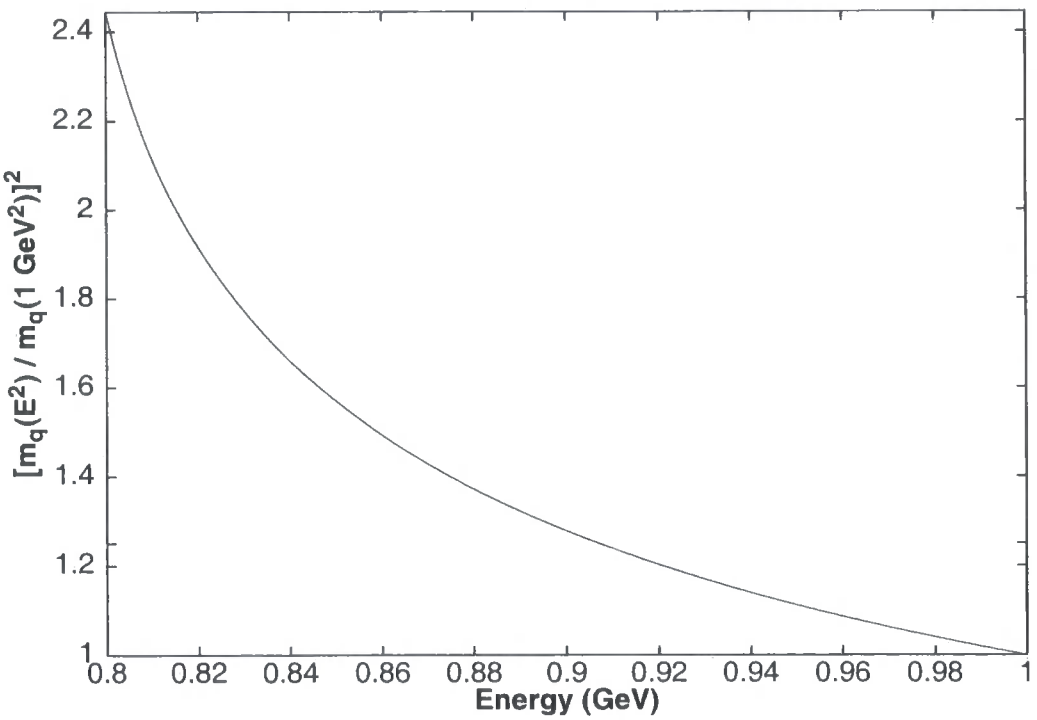

Figure 5.8: The ratio $\left[m_q(E^2)/m_q(1 \text{ GeV}^2)\right]^2$, as calculated from (4.42) using (4.41) and $\alpha_s(m_\tau^2) = 0.334$. Used to determine the scale X.

in Figure 5.7 the average instanton size has been set to the non-standard value $\rho_c = (500\ \text{MeV})^{-1}$. This choice somewhat preempts the results of Section 5.3.2 where we will determine the best value of this parameter more precisely.

From Figure 5.7 we can see that the sum rules are far from satisfied when $\lambda = 0$, *i.e.* when the instanton contribution is removed. However, the sum rules are well saturated for $\lambda = 1.2 - 1.3$. From now on, for the Bugg data-set, we will take $\lambda = 1.25$. From Figure 5.8, we see that this value corresponds to a scale $X \approx 0.91\ \text{GeV}^2$. Using the Kamiński data-set gives a similar result, but the best value of λ is found to be 1.2 corresponding to $X \approx 0.92\ \text{GeV}^2$.

5.3.2 The Average Instanton Size

In Section 5.3.1 it was mentioned that the sum rules were sensitive to the average instanton size, and that the standard value did not give good saturation. We now attempt to fix the best value of the average instanton size. This parameter is not entirely free. Working within the Instanton Liquid Model, with the instanton density fixed at $n_c = 1\ \text{GeV}^{-4}$, the value of ρ_c cannot become too large, else the assumption of diluteness, and hence the framework within which the instanton contribution is calculated, will breakdown. In Figure 5.9 we show the effect that the instanton size has on the saturation curves for the T-type sum rules, using Coupling Scheme II.

We see that saturation is achieved when $\rho_c = (500\ \text{MeV})^{-1}$ and that there is a considerable change of shape of the saturation curve between $\rho_c = (450\ \text{MeV})^{-1}$ and $(500\ \text{MeV})^{-1}$. In Figure 5.10 we explore this region in more detail and can see that good saturation is achieved for $\rho_c = (470 - 490\ \text{MeV})^{-1}$, with the 'best' value being $\rho_c = (480\ \text{MeV})^{-1} \approx 0.42$ fm. This value is slightly larger (25%) than the estimate [90] based on the size of the gluon condensate which has become the standard value employed in the Instanton Liquid Model. However, it is entirely consistent with current lattice determinations which tend to find sizes in the range 0.32 - 0.43 fm. A very similar picture is found using the Kamiński data-set

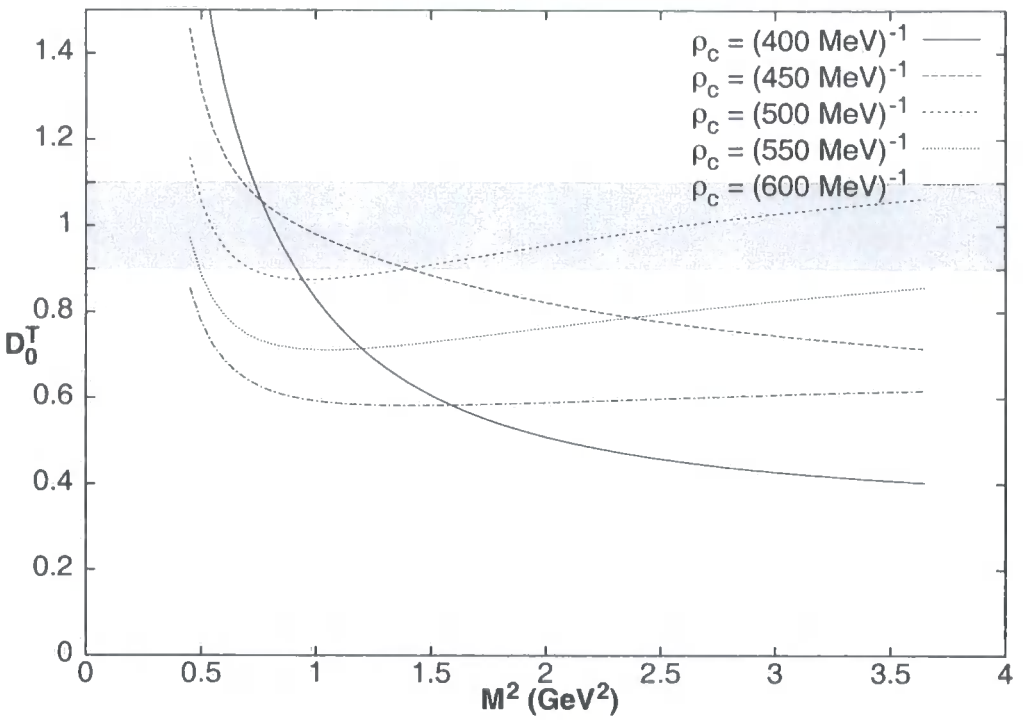

Figure 5.9: The saturation curve, D_0^T, for various values of the average instanton size, ρ_c. $s_0 = 3.7$ GeV^2, $\lambda = 1.25$ and all other parameters set to values listed in Table 5.1.

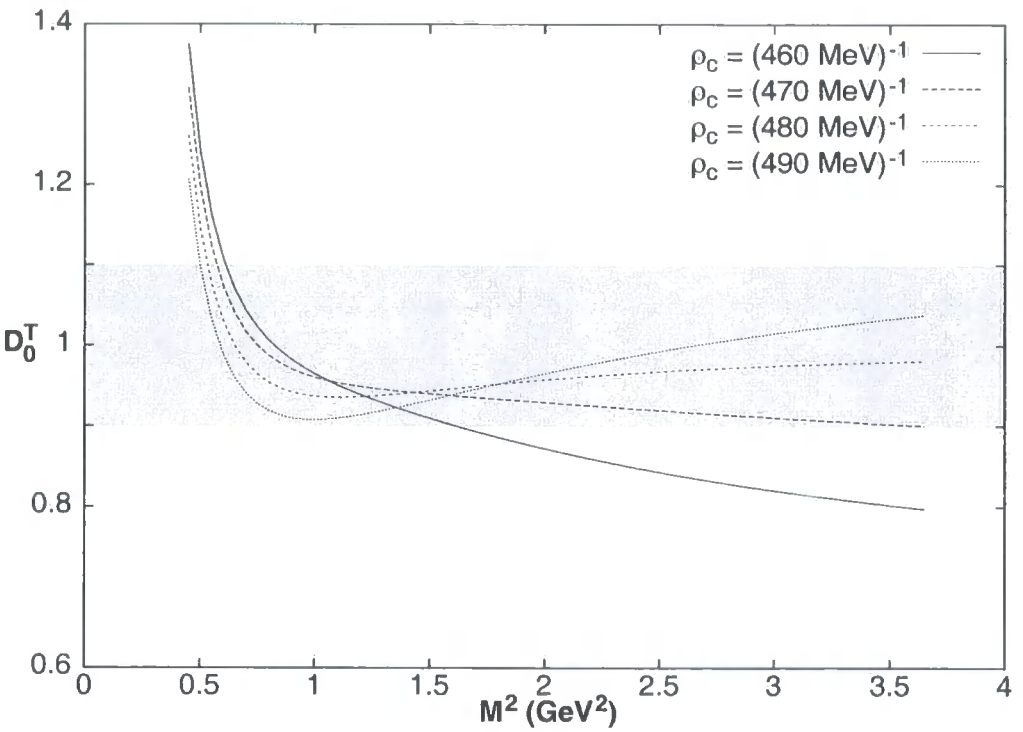

Figure 5.10: As Figure 5.9 but for finer steps in ρ_c.

From now on, unless stated otherwise, all results shown will make use of the instanton sector parameters $\rho_c = (480\ \text{MeV})^{-1}$ and $\lambda = 1.25$ (or $\lambda = 1.2$ for the Kamiński data-set).

5.4 The OPE Parameters

We now turn to the parameters entering into the perturbative and condensate contributions and investigate how they affect the saturation.

5.4.1 The Strong Coupling Constant

The perturbative contribution to our sum rules has only one parameter, which we choose to be the strong coupling constant at a fixed point. This parameter has been experimentally measured many times and as explained in Section 4.7 we take the ALEPH measurement at the mass of the τ as our input. This value, after running, is consistent with measurements at the mass of the Z-boson. As this is not a free parameter we will not try to 'tune' it as we did above with the instanton parameters. Instead, in Figure 5.11, we just show how varying $\alpha_s(m_\tau^2)$ within the experimental error changes the saturation. In Figure 5.11, the instanton quark mass scale, X, has been kept constant. The parameter λ is determined by the running of the quark mass, and so its value at the fixed scale X will depend on $\alpha_s(m_\tau^2)$ as well as the scale. Thus when changing $\alpha_s(m_\tau^2)$ we must also change λ, increasing $\alpha_s(m_\tau^2)$ requires that λ is increased also.

Varying $\alpha_s(m_\tau^2)$ even within the experimental errors destroys the saturation of the sum rules. However, the quality of the saturation can be restored by re-tuning the instanton parameter λ, as illustrated in Figure 5.12. Here the value of λ, and therefore X, has been re-tuned to the best value for each $\alpha_s(m_\tau^2)$. These values are shown in Table 5.2.

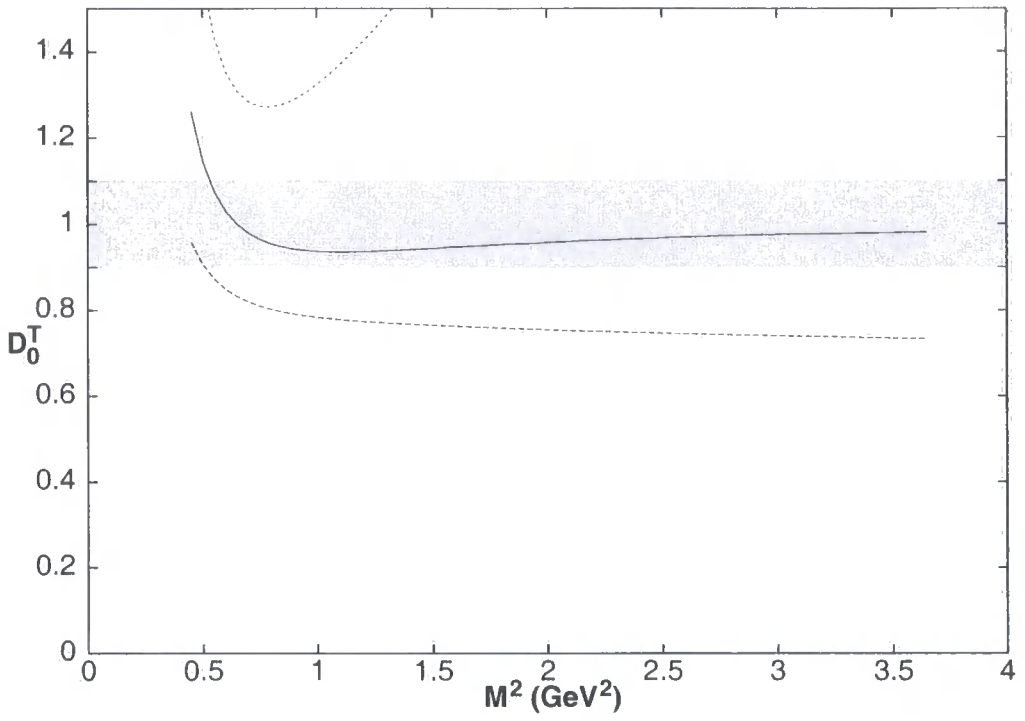

Figure 5.11: The change in saturation as $\alpha_s(m_\tau^2)$ is varied within its experimental error. The dashed line corresponds to $\alpha_s(m_\tau^2) = 0.312$ ($\lambda = 1.17$), the solid line to $\alpha_s(m_\tau^2) = 0.334$ ($\lambda = 1.25$) and the dotted line to $\alpha_s(m_\tau^2) = 0.356$ ($\lambda = 1.49$).

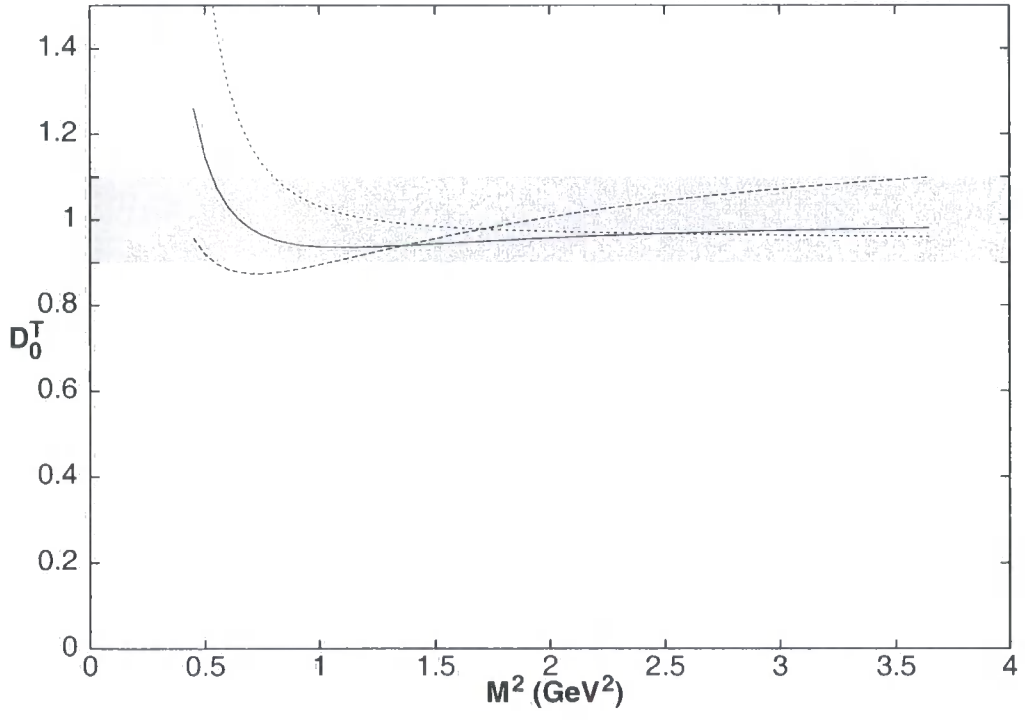

Figure 5.12: As Figure 5.11 but with the parameter λ re-tuned to its best value for each value of $\alpha_s(m_\tau^2)$, as listed in Table 5.2.

	Bugg		Kamiński	
$\alpha_s(m_\tau^2)$	λ	$\sqrt{X}$ (GeV)	λ	$\sqrt{X}$ (GeV)
0.312	1.46	0.82	1.34	0.85
0.334	1.25	0.91	1.20	0.92
0.356	1.05	0.98	0.94	1.02

Table 5.2: The best values of the instanton parameters as $\alpha_s(m_\tau^2)$ is varied across its experimental range, for both data-sets.

5.4.2 The Condensate Parameters

To measure how sensitive our results are to the size of the gluon condensate, we write

$$\langle a_s G^2 \rangle = c \langle a_s G^2 \rangle_0 \tag{5.5}$$

where $\langle a_s G^2 \rangle_0$ is the standard value listed in Table 5.1. The effect of varying the constant c in the range $0 \leq c \leq 2.5$ are shown in Figure 5.13. We see that the double ratio is closest to one for $c = 1.5$ *i.e.* a gluon condensate 50% larger than our standard value. However, the size of the gluon condensate does not heavily effect the saturation of the sum rules.

In Section 4.5.4 the size of the four-quark condensate was estimated via the vacuum saturation hypothesis of [57]. To account for the violation of this hypothesis we introduced the parameter, V_{vs}, with $V_{vs} = 1$ implying that vacuum saturation is exact.. In Figure 5.14 we show how this parameter affects the saturation curve for the Bugg parameterisation. We see that reasonable agreement is obtained in the range $-1 \leq V_{vs} \leq 1.5$. This (more than) encompasses the range of violation of vacuum saturation suggested in [84] and so we conclude that our sum rules are relatively insensitive to the violation of vacuum saturation.

We have also looked at the consequences of varying the remaining condensate parameters *i.e.* $\langle m_q \bar{q} q \rangle$, m_0^2, $\langle m_s \bar{s} s \rangle$ and $m_s(1\ \text{GeV}^2)$. We do not included graphs of these effects as in each case varying the parameter from zero to twice the value listed in Table 5.1 produced no noticeable change in the saturation or quark mass curves.

That the condensate parameters do not greatly affect the saturation of our sum

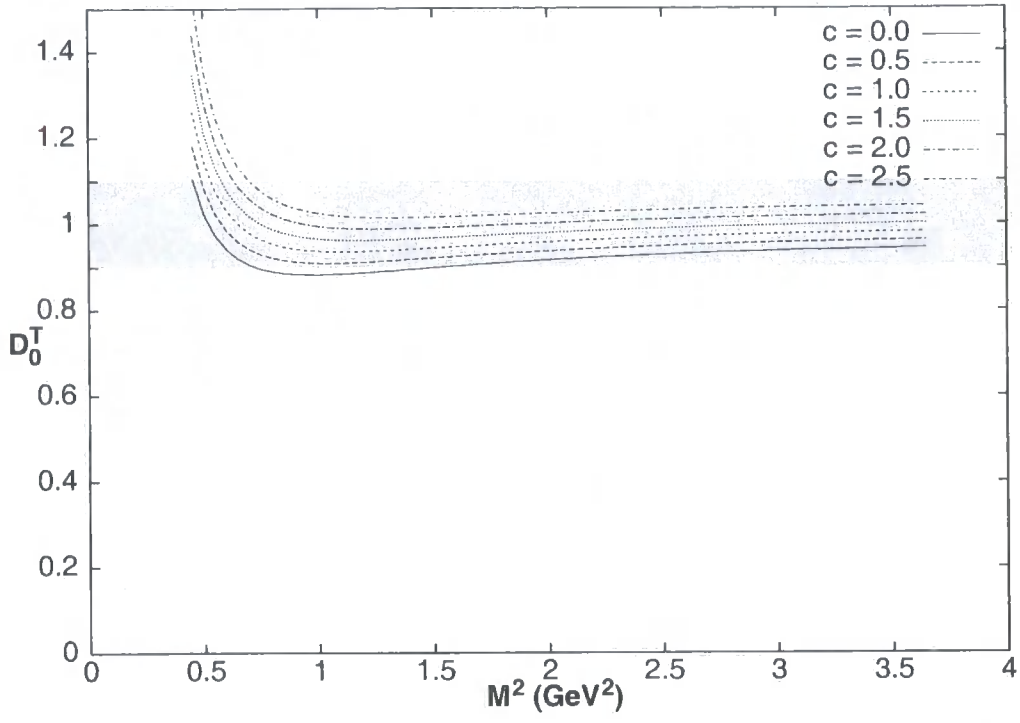

Figure 5.13: The saturation curves, D_0^T, for various values of the gluon condensate.

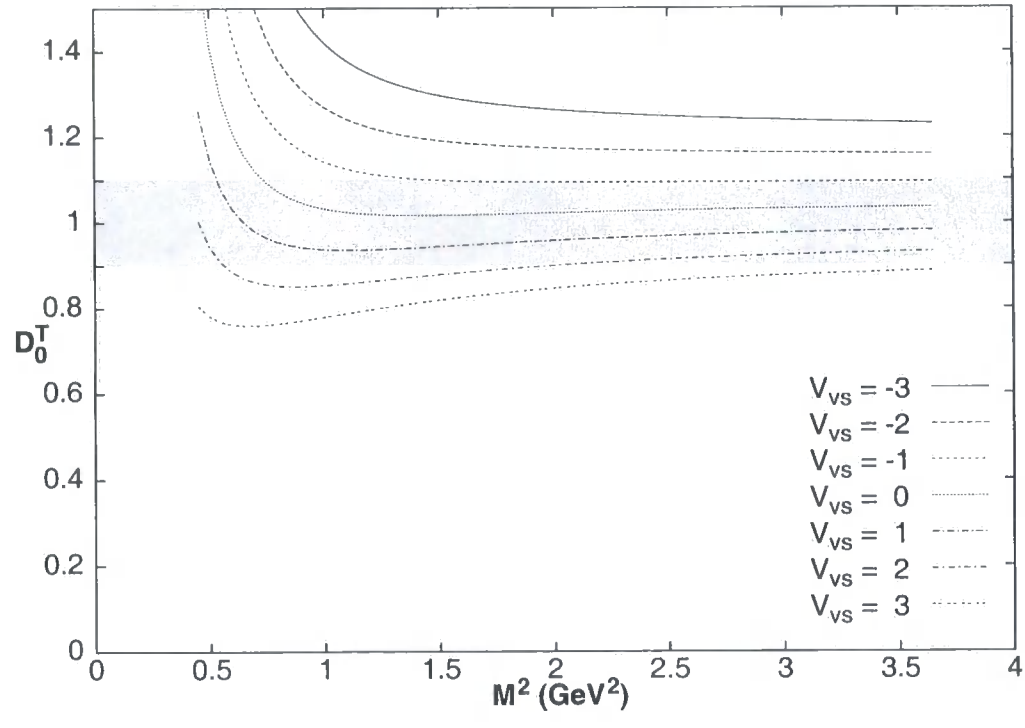

Figure 5.14: The saturation curves, D_0^T, for various values of the vacuum saturation violation parameter, V_{vs}.

rules is no great surprise. As was shown in Figure 5.2 our sum rules are dominated by the perturbative and instanton contributions. Sum rule investigations of the scalar-isoscalar channels are not a good way to determine condensate values, but on the other hand the results in this channel will not depend heavily on the uncertainties in these values.

5.5 The Average Light Quark Mass

As explained in Section 5.3.1 the scalar-isoscalar sum rules can be used to estimate the average *up/down*-quark mass. In Figure 5.15 we show this quark mass curve as calculated using the Bugg data-set and Coupling Scheme II.

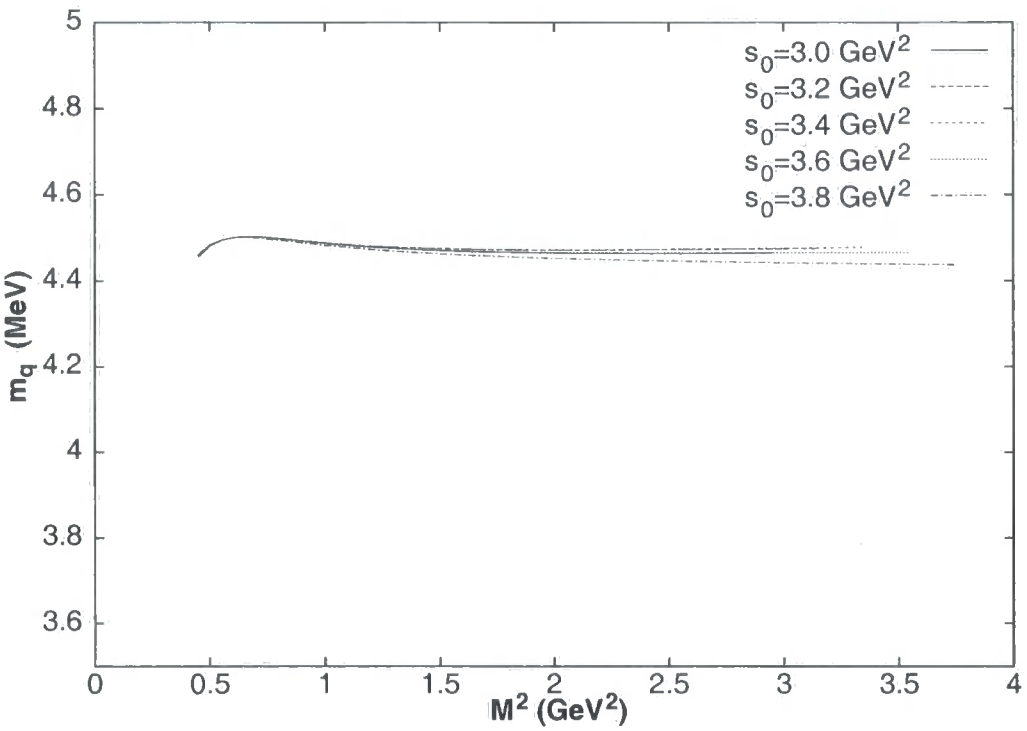

Figure 5.15: The quark mass curves for various values of s_0 in the range where saturation was found to be good.

As we can see, the curves are quite flat, the maximum variation over the entire range being of the order of 1%. This supports the evidence of Sections 5.3 and 5.4 that the sum rules are saturated by our Coupling Schemes. If we confine our investigation to the range indicated, we find that the actual value of the

quark mass is almost independent of s_0. This value is seen to be approximately 4.5 MeV.

To see how stable this value is to the various inputs, we start by considering the effects of the different phenomenological options. Figure 5.16 shows the quark mass curves for the two different data-sets and both Coupling Schemes. We see that, whilst the choice of Coupling Scheme has very little effect, the choice of data-set changes the result by almost 10%. This difference between the two data-sets was found to be almost entirely due to the different constants of proportionality required on the phenomenological side. As stated in Section 4.8.3, the constant of proportionality was not well determined and this was found to be the largest single source of uncertainty in our estimate of the quark mass.

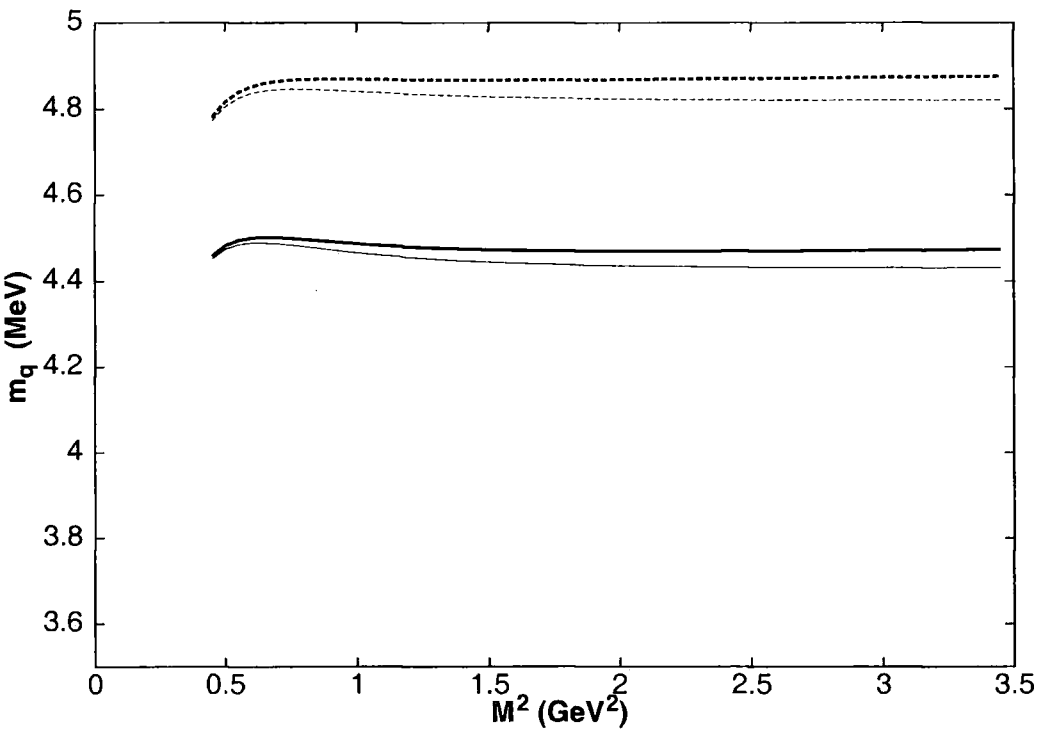

Figure 5.16: The quark mass curves for the Bugg (solid) and Kamiński (dashed) data-sets. The thinner lines come from using Coupling Scheme I and the thicker lines from Coupling Scheme II.

Next we consider the effect the instanton parameters have on the value of the quark mass obtained, confining our investigation to those parameter ranges that were seen to give good saturation in Section 5.3. In Figure 5.17 we show the effect

of the instanton size on the quark mass. We see that this effect is not negligible, varying the instanton size by about 6% changes our result by around 5%.

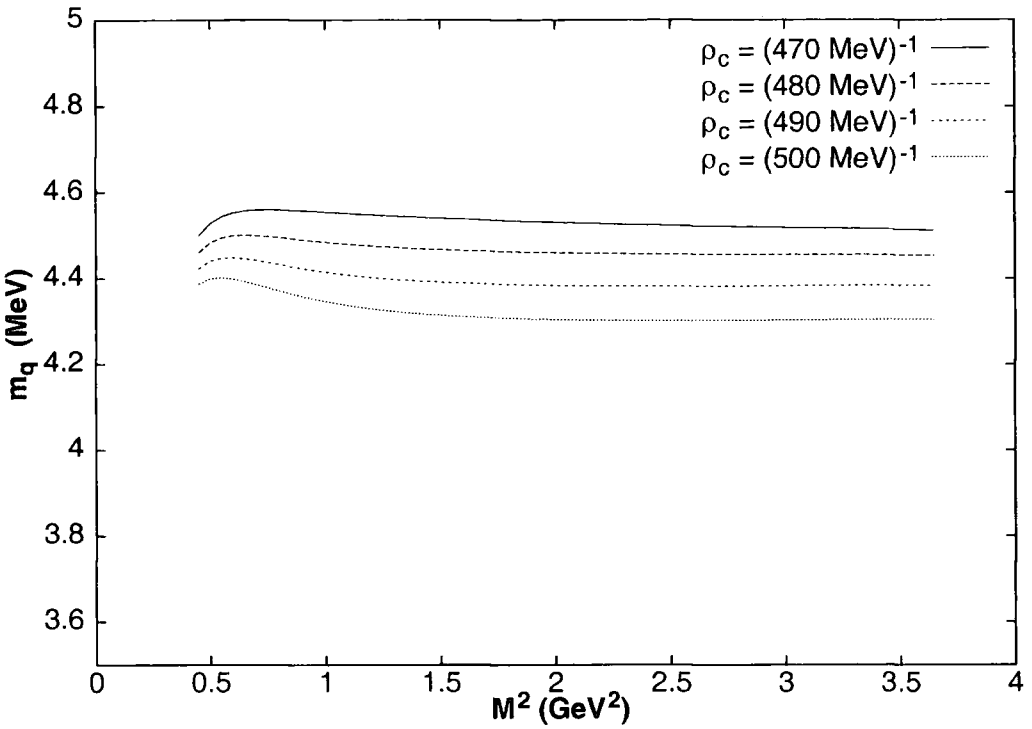

Figure 5.17: The quark mass curves for various values of ρ_c within the region where good saturation was found.

We do not show how the quark mass varies with the parameter λ as this was found to be negligible. This parameter was seen to markedly effect the quality of the saturation of the sum rules without significantly altering the final value obtained for the quark mass.

The input value for the strong coupling constant does, however, have a noticeable effect on the quark mass, as is seen from Figure 5.18. The experimental uncertainty in this quantity translates into an uncertainty in the final answer of around 4%.

Figure 5.19 shows how the input value of the gluon condensate affects the quark mass curves. As for the double ratio, the effect is not large. The quality of the saturation, *i.e.* the flatness of the curve, does not change greatly as the condensate value is changed and the extracted quark mass only differs by 4% over the range studied.

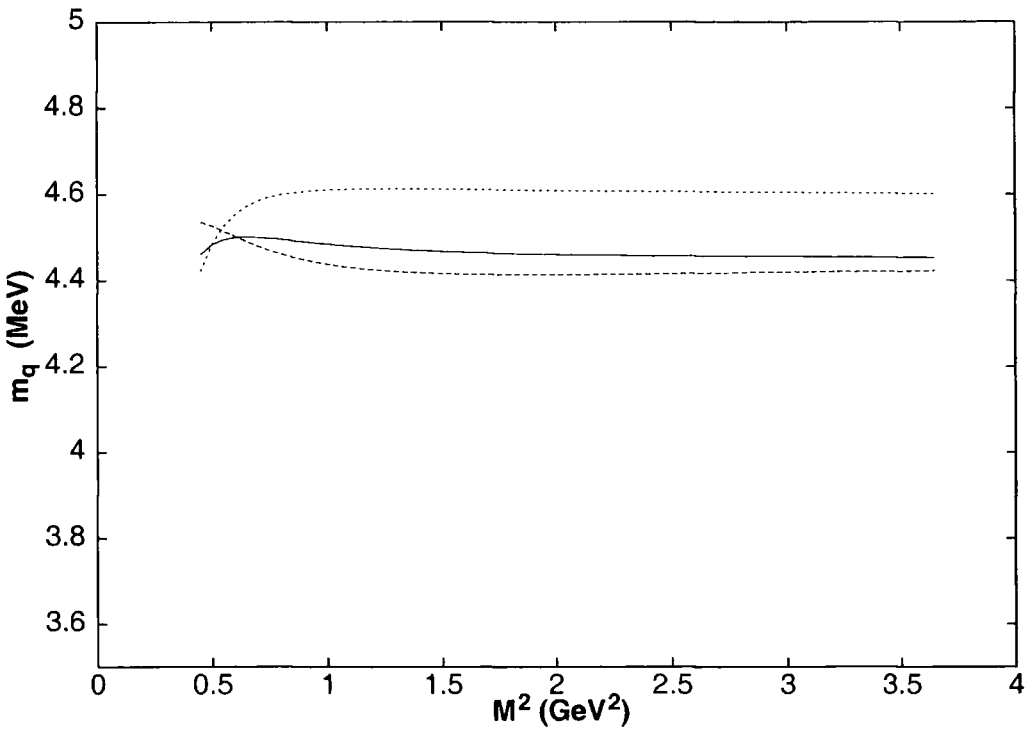

Figure 5.18: The quark mass curves as $\alpha_s(m_\tau^2)$ is varied across its experimental range, with the instanton scale varied according to Table 5.2. The dashed line corresponds to $\alpha_s(m_\tau^2) = 0.312$, the solid line to $\alpha_s(m_\tau^2) = 0.334$ and the dotted line to $\alpha_s(m_\tau^2) = 0.356$.

The effect that violating vacuum saturation has on our estimate of the quark mass is shown in Figure 5.20. From the flatness of the curves we again see that the best saturation is obtained in the range $-1 \leq V_{vs} \leq 1$, agreeing with what we found in Section 5.4.2. Restricting ourselves to this range, the variation in our estimate is about 3%.

From the graphs in this section we estimate that the average light quark mass at 1 GeV^2 is around 4.7 MeV. The combined error arising from the uncertainties arising above is of the order of 20%.

In Table 5.3 we list some other recent estimates of this quantity. Comparing our result with this Table, we see that it is consistent, though markedly lower than, other sum rule determinations. Our value is not consistent with the results of quenched lattice QCD, being approximately 20% lower. However, studies of the strange quark mass suggest that unquenching leads to lower predictions for

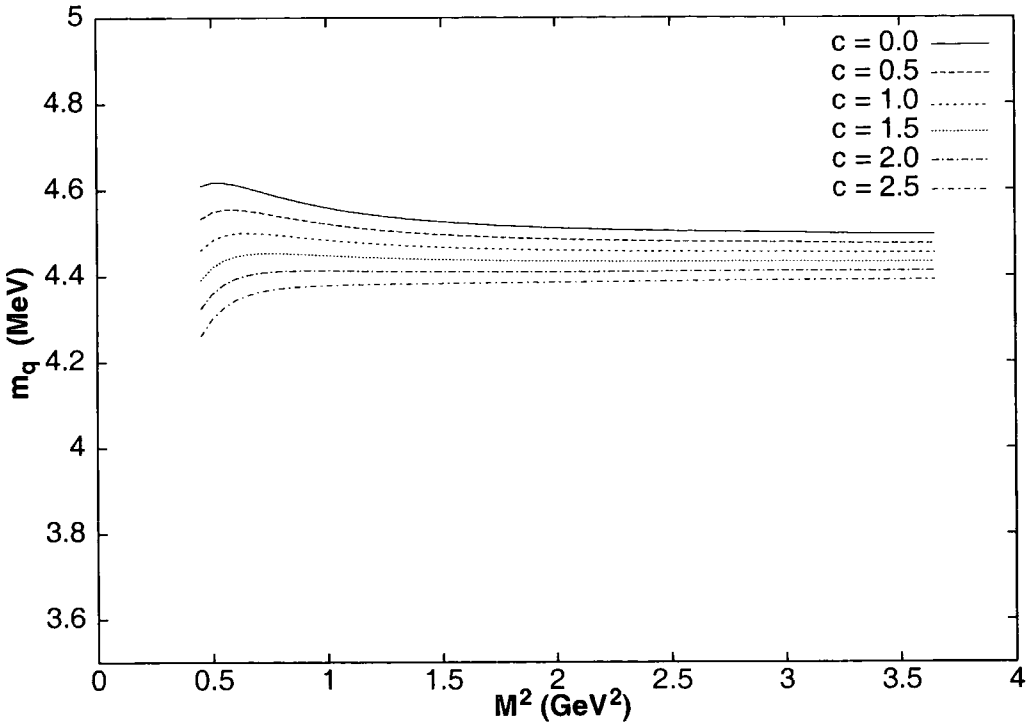

Figure 5.19: The variation of $m_q(1\ \text{GeV}^2)$ with the value of the gluon condensate.

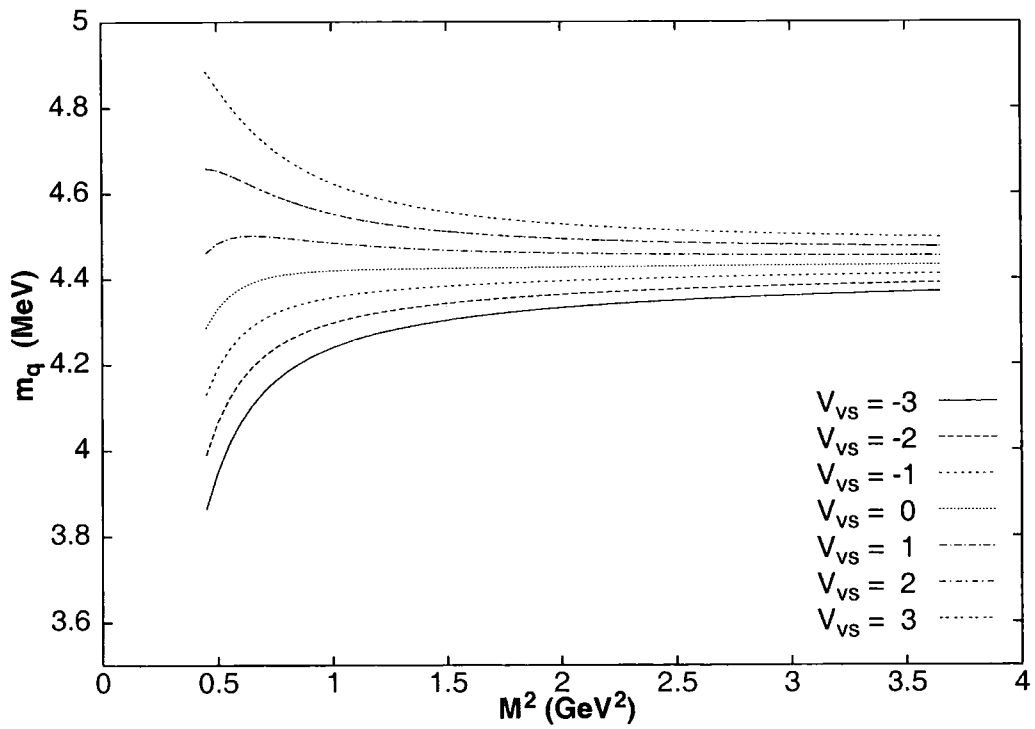

Figure 5.20: The effect of the violation of Vacuum Saturation on our estimate of $m_q(1\ \text{GeV}^2)$.

	Technique	$m_q(1\ \text{GeV}^2)$ (MeV)
Bijnens *et al.* [115]	Pseudoscalar Sum Rule	6.0 ± 2.3
Chetyrkin *et al.* [78]	"	5.7 ± 1.2
Prades [116]	"	6.4 ± 2.3
Maltman & Kambor [117]	"	5.6 ± 0.8
Dosch [118]	SR for $\langle\bar{q}q\rangle$ + GMOR	$4.7 - 7.9$
APE 98 [119]	Quenched Lattice QCD	6.8 ± 0.6
JLQCD 99 [120]	"	6.0 ± 0.4
CP-PACS 99 [121]	"	6.5 ± 0.3
QCDSF 99 [122]	"	6.3 ± 0.3
APE 99 [123]	"	6.8 ± 0.7
CP-PACS 00 [125]	"	6.2 ± 0.2
SESAM 98 [124]	Unquenched Lattice QCD	3.9 ± 0.2
CP-PACS 00 [125]	"	4.9 ± 0.3
QCDSF - UKQCD 01 [126]	"	5.0 ± 0.3

Table 5.3: Recent determinations of $m_q(1\ \text{GeV}^2)$. Note that Lattice QCD results are generally quoted as $m_q(4\ \text{GeV}^2)$ and have here been scaled up by a factor of 1.42 as required by (4.42) with $\alpha_s(m_\tau^2) = 0.334$.

quark masses (see Table 4 of [12]) and this seems to be borne out in the non-strange mass also [124, 125]. Our estimate is consistent with the early results of unquenched lattice QCD.

5.6 Discussion

From the results presented in this Chapter it seems clear that the Coupling Schemes of Section 4.8.1 are capable of saturating our sum rules. These coupling schemes, being based on $\pi\pi$ scattering, contain the $f_0(980)$ as a sharp dip. As such this state does not contribute greatly to the integral on the phenomenological side. That good saturation is possible strongly suggests then that the $f_0(980)$ is not important in saturating the scalar-isoscalar sum rules which in turn implies that it does not contain a large $\bar{n}n$ component in its wave function. This result is at odds with the conclusion reached in [63, 64]. However, as explained above, when the authors of [64] considered a more realistic approximation for the resonance shape the parameters found were more consistent with a Breit-Wigner fit to the $f_0(400-1200)$ than the $f_0(980)$. From this analysis however, beyond

saying that it is not strongly $\overline{n}n$, we can make no comment on the structure of the $f_0(980)$.

Looking more closely at the saturation curves of Sections 5.3 and 5.4 we see that if saturation is achieved at all it starts to set in for relatively low values of M^2, *i.e.* around 1 GeV^2. As the exponential in (4.8) tends to suppress the integrand in the region $s > M^2$, saturation at these values of M^2 would suggest that it is the lower energy portion of the experimental data that is most important in saturating the sum rules. Furthermore, the $f_0(1370)$ will not contribute to the sum rule until $M^2 \gtrsim (m - \Gamma/2)^2 \approx 1.4$ GeV^2. That the sum rules are saturated from $M^2 \approx 1$ GeV^2 thus suggests that it is the $f_0(400-1200)$ that plays the most important role in saturating the $\overline{n}n$ scalar-isoscalar sum rules. This conclusion is independent of the data-set and Coupling Scheme used.

Our results again show that the Operator Product Expansion is not enough to fully describe the physics of the scalar mesons. We find saturation only when instantons are included. One slightly worrying point of this analysis is the need to tune the average instanton size away from its accepted value of $\rho_c \approx (600 \text{ MeV})^{-1} \approx 0.33$ fm. We found that saturation was only possible when $\rho_c \approx (470 - 500 \text{ MeV})^{-1}$ or $\approx 0.40 - 0.42$ fm, which is about 25% larger. The validity of the Instanton Liquid Model relies on the average separation of instantons being significantly larger than their average size. If this is not true then neighbouring instantons will overlap significantly and it becomes meaningless to talk about individual instantons. The assumed average instanton separation of 1 fm is only about 2.5 times the value of ρ_c required by our sum rule, and so we are probably approaching this limit. Reassuringly though, lattice simulations of the topological features of the QCD vacuum seem to find average instanton sizes similar to the one we are forced to use (for a summary of lattice determinations of instanton parameters see [91]).

The quark mass curves of Section 5.5 were found, with the appropriate choice of parameters, to be flat and this flatness sets in at around $M^2 = 1$ GeV^2. This

is again evidence that our Coupling Schemes are capable of satisfying the sum rules and that the state most important for this saturation is the $f_0(400-1200)$. The actual value found for the quark mass was

$$m_q(1\ \mathrm{GeV}^2) = 4.7 \pm 0.9\ \mathrm{MeV}\ . \tag{5.6}$$

The most conservative way to interpret this result is as a consistency check. A number of assumptions are made in this analysis, *e.g.* the validity of the Coupling Schemes, the truncation of the OPE at dimension-6 and the perturbative contribution at $\mathcal{O}(a_s^3)$, the form of the instanton contribution *etc.* That our final result is of the correct order of magnitude at least reassures us that none of our assumptions are too far off the mark. Going further, our estimate is quite compatible with both previous sum rule determinations and the early unquenched lattice estimates that are just starting to appear in the literature.

Chapter 6

Conclusions

In Chapter 2 we have outlined a method, first proposed by Nogová *et al*, for determining the number of resonances in a given channel, and their parameters. This method involves an analytic continuation of the experimental data and does not make use of any model for the underlying dynamics of these states nor of the the non-resonant background scattering. The result of this method as applied to S-wave πK scattering are presented in Chapter 3. These results led us to the conclusion that this channel contains only one resonance in the mass range 825-180 MeV: the established $K_0^*(1430)$. We found no evidence for a light κ in the data from the two highest statistics experiments to explore this channel. That there is only one strange scalar resonance below 1800 MeV obviously has serious implications for models that predict two complete scalar nonets [26, 28, 127].

In Chapters 4 and 5 we have carried out a QCD Finite Energy Sum Rule study of the correlator built from the light-quark scalar isoscalar current. On the experimental side we have argued that the spectral density can be related to $\pi\pi$ scattering data. We found that the $f_0(980)$ was not required to saturate these sum rules and that the $f_0(400-1200)$ plays the most important role in saturation. This suggests that the $f_0(400-1200)$ has a large $u\overline{u}+d\overline{d}$ component in its wave-function whilst $f_0(980)$ does not and is presumably predominantly $s\overline{s}$ or $K\overline{K}$. Although the $f_0(400-1200)$ is capable of saturating our sum rules, its large width would suggest that it spends much of its time in a two meson configuration

in keeping with the picture of [29, 18]. Furthermore, our results would suggest that the $f_0(400-1200)$ does not contain a large gluonic component. This is contrary to the claims of [128] that the $f_0(400-1200)$ and the $f_0(1370)$ are in fact a single, glueball state.

The scalar meson nonet is still very far from being understood. The $K_0^*(1430)$ is generally assumed to be the strange member of the nonet and its mass can be taken as setting the natural mass scale. Our results would suggest that the $f_0(400-1200)$ is a manifestation of the $u\bar{u}+d\bar{d}$ seed state of this nonet. Although its mass is not determined to any great precision, as evidenced by its name, the $f_0(400-1200)$ would appear to be much lighter than we would expect. However, there are mechanisms at work in the scalar sector that can significantly shift the masses of physical hadrons, *e.g* the lifting of the degeneracy of the the isoscalar and isovector due to instantons [63, 64] and the coupling of $q\bar{q}$-states to physical decay channels [28, 29, 18]. Thus the large spread of masses may not be as implausible as it first appears.

The two techniques used in this study could, of course, be applied to the other channels in the scalar sector. In particular, the pole search technique of Chapter 2 could be usefully applied to the isoscalar channel to determine the parameters of the $f_0(400-1200)$ more accurately. With no light κ being found, there seems to be no argument against interpreting the $K_0^*(1430)$ as a $q\bar{q}$-state, thus, in the isospin-1/2 channel, there is little to gain from a sum rule analysis of the type carried out in Chapter 5. The correlators of the the isovector and hidden-strangeness currents, *i.e* $m_q(u\bar{u}-d\bar{d})$ and $m_s s\bar{s}$, do warrant investigating in this way. The theoretical expressions required are already available and are only slightly different from those given in Chapter 4. This could, in principle, allow us to entirely determine the $q\bar{q}$ nonet and indicate what room, if any, is left for the scalar glueball.

Bibliography

[1] H. Yukawa, Proc. Phys. Math. Soc. Jap. **17** (1935) 48.

[2] C. M. Lattes, G. P. Occhialini and C. F. Powell, Nature **160** (1947) 453;
C. M. Lattes, G. P. Occhialini and C. F. Powell, Nature **160** (1947) 486.

[3] Y. Ne'eman, Nucl. Phys. **26** (1961) 222;
M. Gell-Mann, Cal. Tech. Synchrotron Laboratory Report CTSL-20 (1961);
Both reprinted in M. Gell-Mann and Y. Ne'eman, *The Eightfold Way*, Benjamin (1964)

[4] M. Gell-Mann, Phys. Lett. **8** (1964) 214;
G. Zweig, CERN-TH-401 (1964).

[5] O. W. Greenberg, Phys. Rev. Lett. **13** (1964) 598;
M. Y. Han and Y. Nambu, Phys. Rev. **139** (1965) B1006.

[6] D. J. Gross and F. Wilczek, Phys. Rev. Lett. **30** (1973) 1343;
S. Weinberg, Phys. Rev. Lett. **31** (1973) 494;
H. Fritzsch, M. Gell-Mann and H. Leutwyler, Phys. Lett. B **47** (1973) 365.

[7] H. Fritzsch and M. Gell-Mann, Proc. of *XVI International Conference on High Energy Physics*, Chicago, 1972, (ed. J. Jackson, A. Roberts and R. Donaldson) vol. 2 p. 135;
H. Fritzsch and P. Minkowski, Nuovo Cim. A **30** (1975) 393.

[8] D. Horn and J. Mandula, Phys. Rev. D **17** (1978) 898.

[9] K. G. Wilson, Phys. Rev. D **10** (1974) 2445.

[10] C. Bernard *et al.*, hep-lat/0104002.

[11] C. Michael, Nucl. Phys. A **655** (1999) 12 [hep-ph/9810415].

[12] V. Lubicz, Nucl. Phys. Proc. Suppl. **94** (2001) 116 [hep-lat/0012003].

[13] A. Ali Khan *et al.* [CP-PACS Collaboration], Nucl. Phys. Proc. Suppl. **83** (2000) 176 [hep-lat/9909050].

[14] A. Chodos, R. L. Jaffe, K. Johnson, C. B. Thorn and V. F. Weisskopf, Phys. Rev. D **9** (1974) 3471.

[15] T. DeGrand, R. L. Jaffe, K. Johnson and J. Kiskis, Phys. Rev. D **12** (1975) 2060.

[16] S. Godfrey and J. Napolitano, Rev. Mod. Phys. **71** (1999) 1411 [hep-ph/9811410].

[17] M. R. Pennington, hep-ph/9510229.

[18] M. Boglione and M. R. Pennington, Phys. Rev. Lett. **79** (1997) 1998 [hep-ph/9703257].

[19] E. Van Beveren, G. Rupp, T. A. Rijken and C. Dullemond, Phys. Rev. D **27** (1983) 1527.

[20] N. A. Tornqvist, Acta Phys. Polon. B **16** (1985) 503 [Erratum-ibid. B **16** (1985) 683].

[21] D. E. Groom *et al.*, Eur. Phys. J. **C15** (2000) 1.

[22] L. Li, B. Zou and G. Li, Phys. Rev. D **63** (2001) 074003 [hep-ph/0010196].

[23] E. Klempt, hep-ex/0101031.

[24] See for instance L. Montanet *et al.*, Phys. Rev. **D50** (1994) 1173;
V. Chaloupka *et al.*, Phys. Lett. **B50** (1974) 1.

[25] See for example T. Barnes, F. E. Close and S. Monaghan, Nucl. Phys. B **198** (1982) 380;
S. Narison, Nucl. Phys. B **509** (1998) 312 [hep-ph/9612457].

[26] R. L. Jaffe, Phys. Rev. **D15** (1977) 267;
R. L. Jaffe, Phys. Rev. **D15** (1977) 281.

[27] J. Weinstein and N. Isgur, Phys. Rev. Lett. **48** (1982) 659.

[28] E. Van Beveren, T. A. Rijken, K. Metzger, C. Dullemond, G. Rupp and J. E. Ribeiro, Z. Phys. **C30** (1986) 615;
E. van Beveren and G. Rupp, Eur. Phys. J. C **10** (1999) 469 [hep-ph/9806246].

[29] N. A. Tornqvist, Z. Phys. C **68** (1995) 647 [hep-ph/9504372];
N. A. Tornqvist and M. Roos, Phys. Rev. Lett. **76** (1996) 1575 [hep-ph/9511210].

[30] G. Alexander *et al.*, Phys. Rev. Lett. **8** (1962) 447.

[31] V. S. Mather and I. K. Pandit. Phys. Rev. **143** (1966) 1216.

[32] A. Rosenfield *et al.*, Rev. Mod. Phys. **39** (1967) 1.

[33] S. Matsuda, S. Oneda and J. Sucher, Phys. Rev. **159** (1967) 1247.

[34] P. Roy, Phys. Rev. **168** (1968) 1708.

[35] T. G. Trippe *et al.*, Phys. Lett. **28B** (1968) 203.

[36] C. G. Wohl *et al.*, Rev. Mod. Phys. **56** (1984) S1.

[37] P. Estabrooks, R. K. Carnegie, A. D. Martin, W. M. Dunwoodie, T. A. Lasinski and D. W. Leith, Nucl. Phys. **B133** (1978) 490.

[38] D. Aston *et al.* (LASS Collaboration), Nucl. Phys. **B296** (1988) 493.

[39] A. Abele *et al.*, Phys. Rev. **D57** (1998) 3860.

[40] P. L. Frabetti *et al.* [E687 Collaboration], Phys. Lett. **B331** (1994) 217.

[41] C. Gobel [The E791 Collaboration], hep-ex/0012009.

[42] M. D. Scadron, Phys. Rev. **D26** (1982) 239.

[43] S. Ishida, M. Ishida, T. Ishida, K. Takamatsu and T. Tsuru, Prog. Theor. Phys. **98** (1997) 621 [hep-ph/9705437].

[44] D. Black, A. H. Fariborz, F. Sannino and J. Schechter, Phys. Rev. **D58** (1998) 054012 [hep-ph/9804273].

[45] R. Delbourgo and M. D. Scadron, Int. J. Mod. Phys. A **13** (1998) 657 [hep-ph/9807504].

[46] J. A. Oller and E. Oset, Phys. Rev. **D60** (1999) 074023 [hep-ph/9809337].

[47] A. V. Anisovich and A. V. Sarantsev, Phys. Lett. **B413** (1997) 137 [hep-ph/9705401].

[48] J. A. Oller, E. Oset and J. R. Peláez, Phys. Rev. **D59** (1999) 074001; *Erratum-ibid.* **D60** (1999) 099906 [hep-ph/9804209].

[49] M. Jamin, J. A. Oller and A. Pich, Nucl. Phys. B **587** (2000) 331 [hep-ph/0006045].

[50] See e.g. J. T. Taylor *Scattering Theory* John Wiley & Sons (1972); R. J. Eden, P. V. Landshoff, D. I. Olive and J. C. Polkinghorne *The Analytic S-Matrix* CUP (1966).

[51] A. Nogová, J. Pišút and P. Prešnajder, Nucl. Phys. **B61**, (1973) 438; A. Nogová, J. Pišút, Nucl. Phys. **B61**, (1973) 445.

[52] J. Hamilton and T. D. Spearman, Annals of Physics **12**, (1961) 172; See also, J. Hamilton, *High Energy Physics*, (Ed. E. Burhop) **Vol. 1** Academic Press (1967) 193.

[53] E. Barrelet, Nuovo Cim. **A8** (1972) 331.

[54] P. Estabrooks, Phys. Rev. **D19** (1979) 2678.

[55] V. Bernard, N. Kaiser and U. G. Meissner, Nucl. Phys. **B357** (1991) 129; V. Bernard, N. Kaiser and U. G. Meissner, Nucl. Phys. **B364** (1991) 283.

[56] A. Dobado and J. R. Peláez, Phys. Rev. **D47** (1993) 4883 [hep-ph/9301276].

[57] M. A. Shifman, A. I. Vainshtein and V. I. Zakharov, Nucl. Phys. B **147** (1979) 385.

[58] L. J. Reinders, H. Rubinstein and S. Yazaki, Phys. Rept. **127** (1985) 1.

[59] P. Colangelo and A. Khodjamirian, hep-ph/0010175.

[60] L. J. Reinders, S. Yazaki and H. R. Rubinstein, Nucl. Phys. B **196** (1982) 125.

[61] A. Bramon and S. Narison, Mod. Phys. Lett. A **4** (1989) 1113.

[62] E. V. Shuryak, Nucl. Phys. B **319** (1989) 541.

[63] V. Elias, A. H. Fariborz, F. Shi and T. G. Steele, Nucl. Phys. A **633** (1998) 279 [hep-ph/9801415].

[64] F. Shi, T. G. Steele, V. Elias, K. B. Sprague, Y. Xue and A. H. Fariborz, Nucl. Phys. A **671** (2000) 416 [hep-ph/9909475].

[65] K. Maltman, Phys. Lett. B **462** (1999) 14 [hep-ph/9906267].

[66] A. A. Logunov, L. D. Soloviev and A. N. Tavkhelidze, Phys. Lett. B **24** (1967) 181.

[67] R. Shankar, Phys. Rev. D **15** (1977) 755.

[68] E. C. Poggio, H. R. Quinn and S. Weinberg, Phys. Rev. D **13** (1976) 1958.

[69] F. Le Diberder and A. Pich, Phys. Lett. B **289** (1992) 165.

[70] C. A. Dominguez and K. Schilcher, Phys. Lett. B **448** (1999) 93 [hep-ph/9811261].

[71] K. G. Wilson, Phys. Rev. **179** (1969) 1499.

[72] K. G. Chetyrkin, C. A. Dominguez, D. Pirjol and K. Schilcher, Phys. Rev. D **51** (1995) 5090 [hep-ph/9409371].

[73] M. Jamin and M. Münz, Z. Phys. C **66** (1995) 633 [hep-ph/9409335].

[74] S. G. Gorishnii, A. L. Kataev, S. A. Larin and L. R. Surguladze, Mod. Phys. Lett. A **5** (1990) 2703.

[75] K. G. Chetyrkin, Phys. Lett. B **390** (1997) 309 [hep-ph/9608318].

[76] K. G. Chetyrkin, D. Pirjol and K. Schilcher, Phys. Lett. B **404** (1997) 337 [hep-ph/9612394].

[77] M. Beneke, Phys. Rept. **317** (1999) 1 [hep-ph/9807443].

[78] K. G. Chetyrkin, S. Narison and V. I. Zakharov, Nucl. Phys. B **550** (1999) 353 [hep-ph/9811275].

[79] C. A. Dominguez and K. Schilcher, Phys. Rev. D **61** (2000) 114020 [hep-ph/9903483].

[80] L. R. Surguladze and F. V. Tkachov, Nucl. Phys. B **331** (1990) 35.

[81] M. Gell-Mann, R. J. Oakes and B. Renner, Phys. Rev. **175** (1968) 2195.

[82] A. A. Ovchinnikov and A. A. Pivovarov, Sov. J. Nucl. Phys. **48** (1988) 721.

[83] V. M. Belyaev and B. L. Ioffe, Sov. Phys. JETP **56** (1982) 493 [Zh. Eksp. Teor. Fiz. **83** (1982) 876];
Y. Chung, H. G. Dosch, M. Kremer and D. Schall, Z. Phys. C **25** (1984) 151;
M. Kremer and G. Schierholz, Phys. Lett. B **194** (1987) 283.

[84] K. G. Chetyrkin and A. A. Pivovarov, Nuovo Cim. A **100** (1998) 899 [hep-ph/0105093] and references therein.

[85] V. A. Novikov, M. A. Shifman, A. I. Vainshtein and V. I. Zakharov, Nucl. Phys. B **191** (1981) 301.

[86] A. A. Belavin, A. M. Polyakov, A. S. Shvarts and Y. S. Tyupkin, Phys. Lett. B **59** (1975) 85;
G. 't Hooft, Phys. Rev. D **14** (1976) 3432 [Erratum-ibid. D **18** (1976) 2199].

[87] E. V. Shuryak, Nucl. Phys. B **203** (1982) 116.

[88] E. V. Shuryak, Nucl. Phys. B **214** (1983) 237.

[89] E. M. Ilgenfritz and M. Muller-Preussker, Nucl. Phys. B **184** (1981) 443.

[90] E. V. Shuryak, Nucl. Phys. B **203** (1982) 93.

[91] J. W. Negele, Nucl. Phys. Proc. Suppl. **73** (1999) 92 [hep-lat/9810053].

[92] M. Garcia Perez, T. G. Kovacs and P. van Baal, Phys. Lett. B **472** (2000) 295 [hep-ph/9911485].

[93] V. Elias, F. Shi and T. G. Steele, J. Phys. G **G24** (1998) 267.

[94] J. A. Vermaseren, S. A. Larin and T. van Ritbergen, Phys. Lett. B **405** (1997) 327 [hep-ph/9703284].

[95] T. van Ritbergen, J. A. Vermaseren and S. A. Larin, Phys. Lett. B **400** (1997) 379 [hep-ph/9701390].

[96] K. G. Chetyrkin, Phys. Lett. B **404** (1997) 161 [hep-ph/9703278].

[97] R. Barate *et al.* [ALEPH Collaboration], Eur. Phys. J. C **4** (1998) 409.

[98] C. A. Dominguez, A. Ramlakan and K. Schilcher, hep-ph/0104262.

[99] K. M. Watson, Phys. Rev. **88** (1952) 1163.

[100] S. L. Adler, Phys. Rev. **137** (1965) B1022.

[101] D. V. Bugg, I. Scott, B. S. Zou, V. V. Anisovich, A. V. Sarantsev, T. H. Burnett and S. Sutlief, Phys. Lett. B **353** (1995) 378.

[102] A. Abele *et al.* [Crystal Barrel Collaboration], Phys. Lett. B **380** (1996) 453.

[103] D. V. Bugg, B. S. Zou and A. V. Sarantsev, Nucl. Phys. B **471** (1996) 59.

[104] R. Kamiński, L. Leśniak and K. Rybicki, Z. Phys. C **74** (1997) 79 [hep-ph/9606362].

[105] G. Grayer *et al.*, Nucl. Phys. B **75** (1974) 189.

[106] H. Becker *et al.* [CERN-Munich Collaboration], Nucl. Phys. B **150** (1979) 301;
H. Becker *et al.* [CERN-Cracow-Munich Collaboration], Nucl. Phys. B **151** (1979) 46.

[107] B. Hyams *et al.*, Nucl. Phys. B **64** (1973) 134 [AIP Conf. Proc. **13** (1973) 206];
W. Ochs, Ph.D. Thesis, Ludwig-Maximilians-Universität, München (1974).

[108] M. R. Pennington, *The DAΦNE Physics Handbook,* ed. L. Maiani, G. Pancheri and N. Paver (INFN, Frascati, 1992) vol. 2 pp. 379-418;
M. R. Pennington, *The Second DAΦNE Physics Handbook,* ed. L. Maiani, G. Pancheri and N. Paver (INFN, Frascati, 1995) vol. 2 pp. 531-558.

[109] L. Rosselet *et al.*, Phys. Rev. D **15** (1977) 574.

[110] E. A. Alekseeva *et al.*, Sov. Phys. JETP **55** (1982) 591 [Zh. Eksp. Teor. Fiz. **82** (1982) 1007].

[111] P. Estabrooks and A. D. Martin, Phys. Lett. B **41** (1972) 350;
P. Estabrooks and A. D. Martin, Nucl. Phys. B **79** (1974) 301.

[112] R. Omnès, Nuovo Cim. **8** (1958) 316.

[113] H. Hellmann, *Einfürung in die Quantenchemie*, Deuticke (1937)
R. P. Feynman, Phys. Rev. **56**, 340 (1939).

[114] G. Colangelo, J. Gasser and H. Leutwyler, hep-ph/0103088.

[115] J. Bijnens, J. Prades and E. de Rafael, Phys. Lett. B **348** (1995) 226 [hep-ph/9411285].

[116] J. Prades, Nucl. Phys. Proc. Suppl. **64** (1998) 253 [hep-ph/9708395].

[117] K. Maltman and J. Kambor, [hep-ph/0107060].

[118] H. G. Dosch and S. Narison, Phys. Lett. B **417** (1998) 173 [hep-ph/9709215].

[119] D. Becirevic, P. Boucaud, J. P. Leroy, V. Lubicz, G. Martinelli and F. Mescia, Phys. Lett. B **444** (1998) 401 [hep-lat/9807046].

[120] S. Aoki *et al.* [JLQCD Collaboration], Phys. Rev. Lett. **82** (1999) 4392 [hep-lat/9901019].

[121] S. Aoki *et al.* [CP-PACS Collaboration], Phys. Rev. Lett. **84** (2000) 238 [hep-lat/9904012].

[122] M. Gockeler *et al.*, Phys. Rev. D **62** (2000) 054504 [hep-lat/9908005].

[123] D. Becirevic, V. Gimenez, V. Lubicz and G. Martinelli, Phys. Rev. D **61** (2000) 114507 [hep-lat/9909082].

[124] N. Eicker *et al.* [SESAM collaboration], Phys. Rev. D **59** (1999) 014509 [hep-lat/9806027].

[125] A. Ali Khan *et al.* [CP-PACS Collaboration], Phys. Rev. Lett. **85** (2000) 4674 [hep-lat/0004010].

[126] D. Pleiter [QCDSF and UKQCD Collaborations], Nucl. Phys. Proc. Suppl. **94** (2001) 265 [hep-lat/0010063].

[127] D. Black, A. H. Fariborz, F. Sannino and J. Schechter, Phys. Rev. **D59** (1999) 074026 [hep-ph/9808415];
D. Black, A. H. Fariborz and J. Schechter, Phys. Rev. **D61** (2000) 074001 [hep-ph/9907516].

[128] P. Minkowski and W. Ochs, Eur. Phys. J. C **9** (1999) 283 [hep-ph/9811518].

[129] S. N. Cherry and M. R. Pennington, Nucl. Phys. A **688** (2001) 823 [hep-ph/0005208];
S. Cherry and M. R. Pennington, hep-ph/0007275.